Fossils of the Distant Galaxy: NGC 5466 and its Stellar Stream

by

Jaclyn Jensen
B.Sc., University of Denver, 2017

A Dissertation Submitted in Partial Fulfillment of the
Requirements for the Degree of

MASTER OF SCIENCE

in the Department of Physics & Astronomy

Fossils of the Distant Galaxy: NGC 5466 and its Stellar Stream

by

Jaclyn Jensen
B.Sc., University of Denver, 2017

Supervisory Committee

Dr. Alan McConnachie, Co-Supervisor
(Department of Physics and Astronomy)

Dr. Sara Ellison, Co-Supervisor
(Department of Physics and Astronomy)

ABSTRACT

The stellar halo of the Milky Way is populated by mostly old and metal-poor stars. As dynamical timescales are of order ∼Gyrs at these large distances, accreted stellar substructures, such as dwarf galaxies or globular clusters, survive here as coherent entities longer than anywhere else in the Galaxy. These substructures represent our "fossil record" which can be used to reconstruct the Galaxy's complex past. In this work, we seek to identify the structures found in the far reaches of the stellar halo as a step towards a correct interpretation of this fossil record. The advent of all-sky surveys in the *Gaia* era has ignited a prosperous period for this field of Galactic archaeology, but exploring the distant Milky Way (>10 kpc) with *Gaia* is difficult. Parallax measurements are much less accurate beyond the Solar neighborhood, though *Gaia*'s proper motions remain useful out to large radii.

To push *Gaia* into the distant Galaxy, we combined these astrometric data with *u*-band photometry from the Canada-France Imaging Survey (CFIS). We exploited CFIS' excellent photometric quality and depth (which extends 3 magnitudes deeper than that of the Sloan Digital Sky Survey) to use blue horizontal branch stars (BHBs) as a tracer population with well-measured distances. We first examined the distribution of BHBs using the OPTICS (*Ordering Points To Identify the Clustering Structure*) clustering algorithm to visualize the hierarchical nature of outer halo substructure. We then identified several well-known satellites, including a group of stars in the vicinity of a distant globular cluster (NGC 5466). Analysis of their kinematics suggested a few of these BHBs outside the cluster's tidal radius were co-moving with NGC 5466, implying they may be tidal debris from this system. Interestingly, a stream had previously been detected extending from this globular cluster. However, its properties had not been studied in the decade since its discovery, and previous dynamical models were unable to reproduce many of the reported features. As one of the (allegedly) longest globular cluster streams on the sky - and given its distance and utility to constrain the Milky Way's mass at large Galactic radius - we sought to explore this structure further.

We subsequently used red giant branch stars (RGBs) identified in CFIS to try to better quantify the characteristics of the putative stream. We were able to filter these data and obtain a sample of stars that are fully consistent with stream membership and which span approximately 31° of sky. Combined with the BHBs, we used these populations to trace the path of the stream, its distance and distance gradient across

the stream's longitude, and additionally estimated a lower limit to the stream's luminosity. Our measurements suggest that the stream is at least 11% of the luminosity of the cluster.

We then compared our observational data to dynamical models, which showed generally good agreement with the observed stream. This success reflects the updated properties of data measured in this work, and the inclusion of new data (especially proper motions). Our model suggests that the pericenter and apocenter of NGC 5466's orbit are 6.4 and 43 kpc, respectively, resulting in a very eccentric orbit ($\varepsilon = 0.74$). We also find evidence that the cluster experienced a recent interaction (within the past $\sim$100 Myrs) with the Galactic disk, suggesting that the primary source of mass loss in this system may be caused by disk-shocking. The NGC 5466 stellar stream also exhibits an interesting heliocentric gradient in the leading arm, which our simplistic spherical halo model does not fully reproduce. Dynamical experiments with various halo shapes fit to this stream will prove interesting for future work. For local cosmology in particular, long, thin, dynamically cold stellar streams are ideal systems for constraining properties of the Milky Way's dark matter halo, and streams at large radius are especially useful for measuring the Galaxy's mass interior to the stream. In this respect, we anticipate that NGC 5466 will be exceptionally useful as a probe of the shape, mass, and dark substructure of the Milky Way's distant dark matter halo.

Contents

List of Tables

List of Figures

Acknowledgements

I would like to thank my friends, family and professors through the years that encouraged me to continue on this academic journey. Your support moves mountains, and I would not be here without you. Thank you to all the giants on whose shoulders I stand. Above all, much thanks to:

Alan McConnachie, for everyday support, patience, and encouragement. Thank you for your understanding and willingness to teach me.

My step-father and my mom, for always supporting me to foster a deep curiosity, love for science, and teaching me that intelligence is a cultivated trait.

My immediate academic family (Katie Crotts, William Thompson, and Guillaume Thomas),
for our adventures,
your cheer,
game nights,
and beer.

My first-born cat (Sushi), for the mental health support, constant laughs, and riveting conversations.

My sun and stars (James), for your calming exterior in the face of adversity. Your support and light triumphs all.

Beyond a wholesome discipline,
be gentle with yourself.
You are a child of the Universe,
no less than the trees and the stars;
you have a right to be here.
And whether or not it is clear to you,
no doubt the Universe is unfolding as it should.
Excerpt from *Desiderata* by Max Ehrmann

Chapter 1

Introduction

1.1 Our Milky Way

Our Galaxy is one of trillions in the observable Universe (Conselice et al. 2016), yet as our home, it is extraordinarily unique. Galaxies evolve over their lifetime in part due to interactions with larger galaxies and the accretion of smaller satellites – a history which is distinct from one galaxy to another. Observational evidence for this *hierarchical merging* is present in our own Milky Way through the study of its satellites as they are perturbed or fully destroyed by the Galaxy's gravitational potential. Mergers not only cause galaxies to grow by subsuming the stars of other systems, but they can also induce new star formation and change the host's structure (Renaud et al. 2020). Thus, each galaxy's accretion history is directly tied to its observable structure and stellar populations.

The Milky Way presents a unique case study for understanding galactic formation. Though our position within the disk is not ideal to view its global properties, our advantage is access to highly detailed data for billions of individual stars. Revolutionary large-sky surveys have provided unprecedented perspectives of the Milky Way in recent years, for example, the Sloan Digital Sky Survey (SDSS, York et al. 2000), Pan-STARRS 3π survey (PS1; Chambers et al. 2016), the Dark Energy Survey (DES; The Dark Energy Survey Collaboration 2005), and most notably, the advent of the first and second *Gaia* data releases (Gaia Collaboration et al. 2016b, 2018). The precise astrometry *Gaia* provides is the missing link to track the orbits of millions of stars back to the early Galaxy, and predict their trajectory in the future. Stellar orbits are key to understanding the features and characteristics of the Galaxy's various

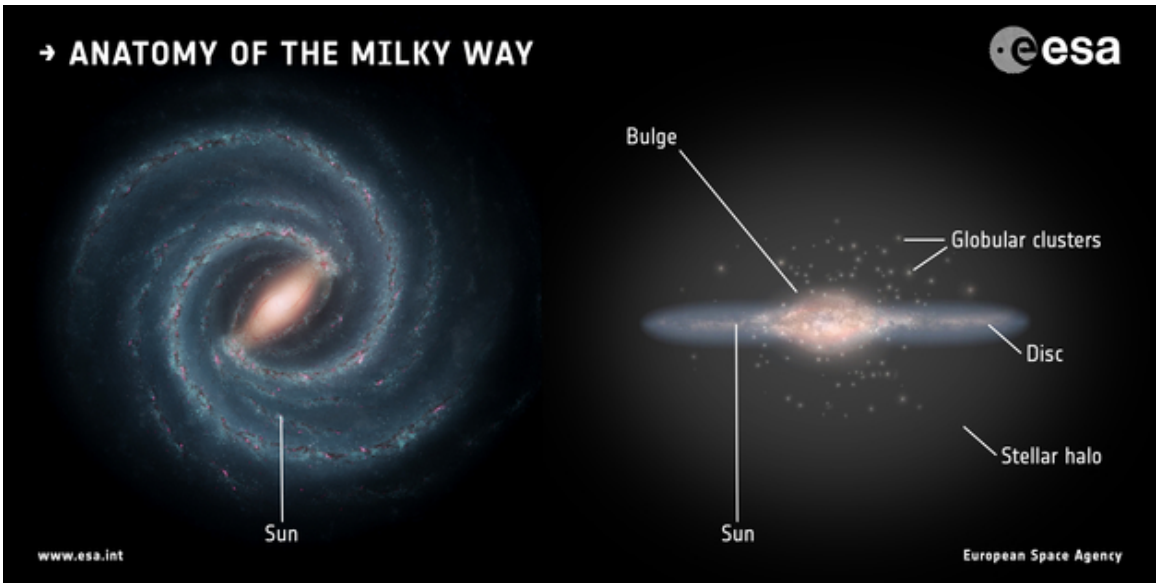

Figure 1.1: Artist's representation of the Milky Way face-on (left) and edge-on (right). Source: European Space Agency (https://sci.esa.int/web/gaia/-/58206-anatomy-of-the-milky-way).

structures.

We know that the Milky Way is formed of gas, dust, and stars (Bland-Hawthorn & Gerhard 2016) and its overall structure is akin to many other disk galaxies. It is typically described by three observable components, as shown in the artist's rendering above (Figure 1.1). The central regions are dominated by the Galactic bulge, protruded by a rotating bar. Encircling this system is a flattened, rotationally-supported gaseous disk consisting of two features. The first being the thin disk, which is a site of ongoing star formation in the Galaxy and has been actively doing so for approximately 9 Gyrs (Tononi et al. 2019). Surrounding this structure is a hotter, more diffuse thick disk composed of older stellar populations than that of the thin disk (Kilic et al. 2017). The final observable element to the Galaxy is the stellar halo which contains many metal-poor and old substructures. The major baryonic components of the Milky Way are enveloped by the dark matter halo, for which many properties remain unknown.

The overall formation process of the Galaxy and its components occurs within the larger context of structure formation dominated by dark energy and dark matter. As such, we provide a brief overview of the standard theoretical perspective known as Λ Cold Dark Matter (ΛCDM) below.

1.2 The Standard Cosmological Perspective

ΛCDM is the standard cosmological model by which the Universe is thought to have formed and evolved (Somerville & Davé 2015 and references therein). In this paradigm, the dominant energy component of the Universe is Λ, representing the Einstein cosmological constant and its relationship to dark energy. The nature of dark energy is not presently understood, but it is hypothesized to contribute a "negative pressure" in the early Universe, counteracting the gravitational force which would otherwise slow down the expansion of the Universe following the Big Bang.

The principal source of gravitational forces in this paradigm is Cold Dark Matter which dominates over baryonic matter by ∼sixfold (Planck Collaboration et al. 2016). The "cold" aspect of these non-baryonic particles relates to their low velocities (significantly slower than the speed of light). Unlike baryonic matter, CDM is collisionless, such that no thermal energy is transferred between particles. Thus, the only way CDM can interact is via gravity.

Following the Big Bang, the Universe was an extremely hot plasma of baryonic and non-baryonic matter. This primordial plasma exhibited density fluctuations on a quantum scale that grew during Inflation, creating a global density matter field. Overdense regions grew and merged with one another, and accumulated mass exponentially over time. As each high-density region approaches a critical threshold above the background, they became gravitationally self-bound.

It was by these density "seeds" that galaxies formed (Mo et al. 2010), accreting gas in their deep potential wells in the process and forming *proto-galaxies*. As the gas in these systems cooled, the net angular momentum of the gas forms a rotationally supported disk, in which star formation occurs.

But then where do the stars observed in the halo originate? Building a stellar halo is thought to occur hierarchically (e.g. smaller galaxies are cannibalized by bigger ones; Searle & Zinn 1978) through cosmic time as a natural consequence of the large-scale structure surrounding any individual galaxy. An example of a "standard" halo built up from these accretions is shown in Figure 1.2. This particular halo is an analogue of a Milky Way-like galaxy from the Johnston et al. (2008) simulation suites. The upper left panel of Figure 1.2 shows an external view of this model, where a handful of subhalos are present. The numerous fainter intersecting features are also represented in the upper right panel as an all-sky view. These structures are potentially observable out to relatively large heliocentric distances, though given

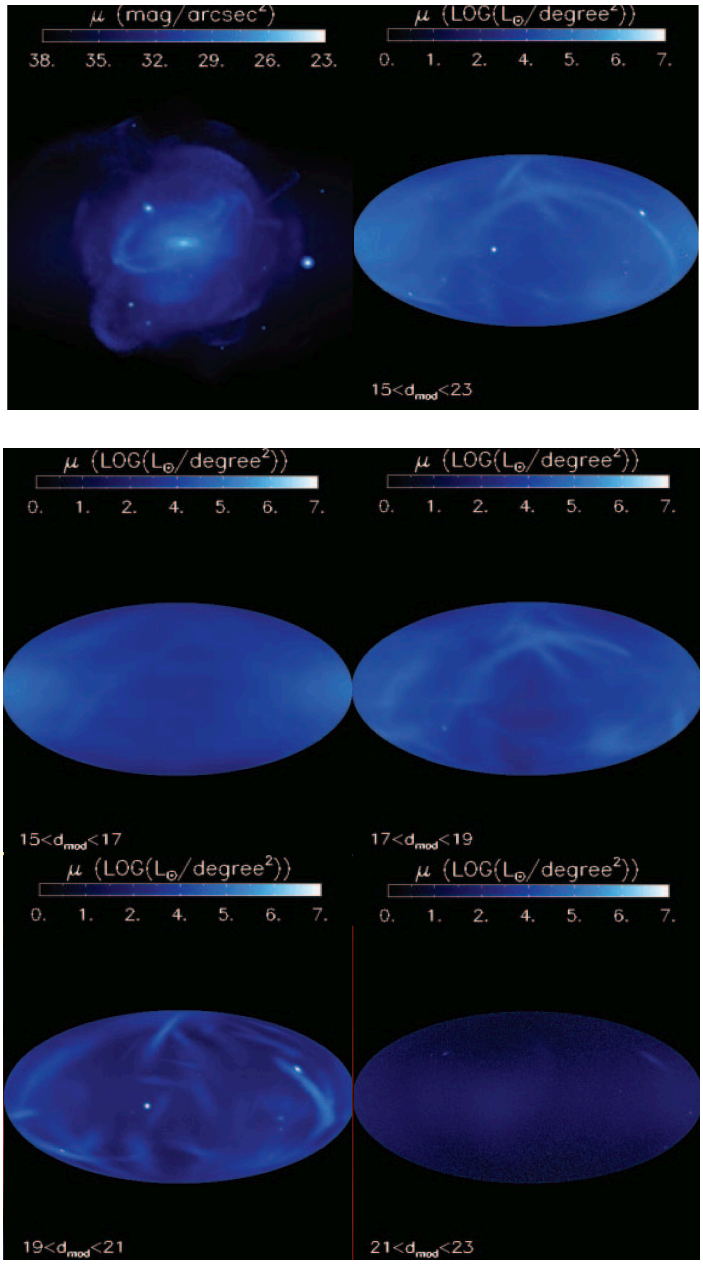

Figure 1.2: A "standard" halo from the suite of Milky Way halo analogues directly from Johnston et al. (2008), built up over time via a series of mergers. The color scale indicates surface brightness. The upper-most plots show an external view of the Galaxy (left; 300 kpc on each side), and the all-sky projection (right; as viewed at 8 kpc, or near the Sun) for substructure distances of $15 - 23$ kpc. Each panel below highlights four distance bins for comparison (R_{helio} = [15, 17] in middle left, [17, 19] in middle right, [19, 21] in bottom left, and [21, 23] in bottom right).

their low surface brightness, are best observed in very nearby systems like the Milky Way. It is worth noting that some halo stars may also be formed *in-situ* – that is, they may be ejected from a heated disk after a merger. For example, simulations by Monachesi et al. 2019 show that up to 20% of Milky Way halo stars beyond 50 kpc could originate in this fashion, as opposed to originating from remnants of destroyed satellites (*ex-situ*).

ΛCDM is the most widely accepted theoretical perspective for the overall formation of the Universe, and it has demonstrated excellent consistency with large-scale observations such as the Cosmic Microwave Background, the Universe's expansion observed with Type Ia supernovae, and distributions of galaxy groups (Planck Collaboration et al. 2016). However, this paradigm was not developed to explain the properties of small-scale structure and galaxies, though there is some qualitative agreement with observations. More detailed observations on these scales are necessary to stress the theory and advance our understanding of galaxy formation. With respect to better understanding the merger histories of galaxies and the structure of stellar halos, our own Milky Way serves as the perfect laboratory.

1.3 Galactic Archaeology

With the rise of large-sky surveys in the past few years, charting the Milky Way has never been more achievable. This field is known as Galactic archaeology (see Belokurov 2013 for an excellent review). In this domain, we seek to answer questions about the Galaxy's assembly and formation. For example, what role did hierarchical merging play in the development of the main components of the Galaxy? How did these structures evolve over cosmic time and what effect does this have on the Galaxy's star formation history? Can we establish a timeline of major events?

The chemical composition, kinematics, and ages of stars are the data most relevant to these questions. As described in Helmi (2020), stars retain a memory of their origin. New generations of stars are formed with the chemical abundances available in the interstellar cloud of their birth, and elements in each star's atmosphere are linked to the chemical enrichment of its previous environment. Old stars in particular are recognized as probes of the chemistry and kinematics of the early years of the Galaxy. Galactic archaeologists target these old stellar populations in the bulge and halo to understand the conditions under which these ancient stars were created. Below, we discuss recent discoveries relevant to the field that are most influential to shaping our

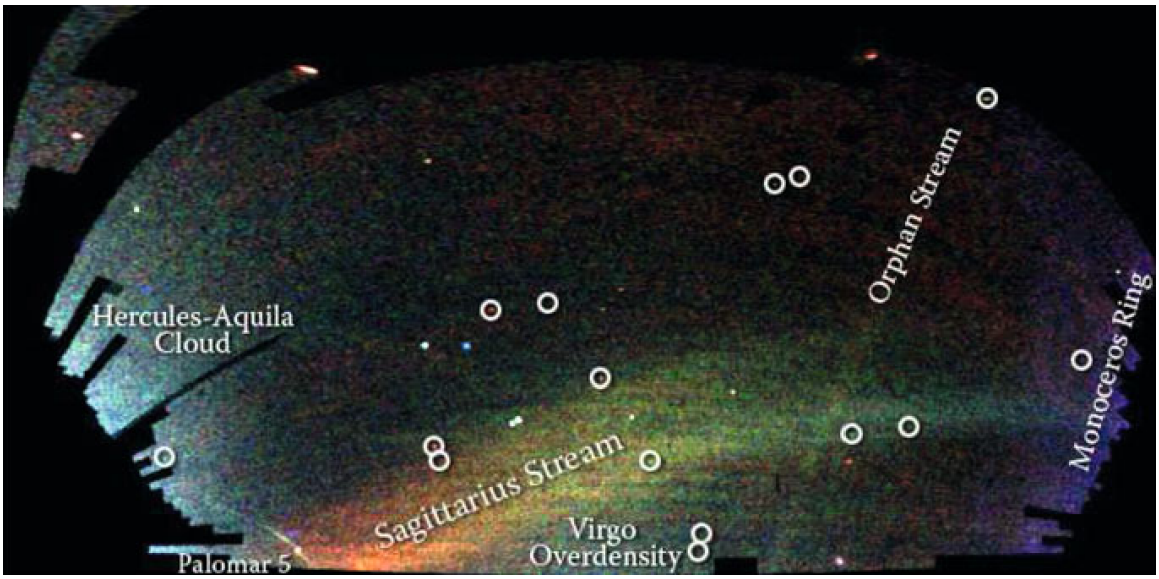

Figure 1.3: Representation of the SDSS "Field of Streams", originally created in Belokurov et al. (2006b). This reproduction is taken directly from Newberg (2016) using upper main sequence and turnoff stars color-coded by distance (blue are distances less than 15 kpc, red are distances greater than 25).

Galactic perspective.

1.3.1 Significant Accretions

As a satellite orbits a host halo, the host imparts a differential gravitational force across the smaller body which can eventually result in *tidal stripping*. Depending on the positions on the satellite where the mass was stripped, the stars can lie on slightly higher and slightly lower orbital energies than their progenitor. The mass located at higher potential energies (i.e. released at farther Galactocentric radii) trail behind the satellite, while mass at lower potentials leads forward. Thus, these stars form the leading and trailing arms of a *stellar stream*.

Given the number of predicted satellites in ΛCDM for a typical Milky Way-mass galaxy, the stellar halo should be littered with traces of these structures across the sky (as shown in the simulation captured in Figure 1.2). It was no surprise then, that the number of stellar streams observed in SDSS were numerous. The northern map first observed by Belokurov et al. (2006b) is appropriately titled the "Field of Streams"; we show a reproduction of this landscape in Figure 1.3 from Newberg (2016).

In this figure, upper main sequence and turn off stars are colored in blue at

distances less than 15 kpc, and red represents approximately more than 25 kpc. The most obvious overdensities/structures are labeled, while circles highlight the Milky Way satellites newly discovered within this particular SDSS dataset. It is extraordinary the influence that large-sky surveys like SDSS have on new Galactic discoveries, evidenced by the sheer number of structures observed in this map.

The most unmistakable feature in this figure is the notorious Sagittarius stellar stream. After the progenitor's identification by Ibata et al. (1994, 1995) for which there was already evidence to suggest tidal disruption, tidal tails were subsequently detected firstly by Ibata et al. (2001a) in SDSS, followed by detections in the 2MASS survey (Ibata et al. 2002; Majewski et al. 2003). The Sagittarius stream extends incredible distances – up to ∼100° on the sky, and ranging from R_{helio} = [7, 100] kpc. Ongoing studies have been extensively probing the stream to understand its kinematics and morphology (e.g., Ruhland et al. 2011; Vasiliev & Belokurov 2020; Antoja et al. 2020 and references therein) and efforts to locate the galaxy's stripped globular cluster populations have found them dispersed around the Milky Way (Ibata et al. 1995; Bellazzini et al. 2020).

As this stream (a) consists of many stellar members, (b) is presently experiencing the mid-stages of disruption, and (c) covers large distances around the Galaxy, it has been the focus of many recent studies (Law & Majewski 2016 and references therein). Namely, the disruption of Sagittarius is an interesting target to model the shape and mass of the Galaxy's dark matter halo. However, agreement for the shape of the halo constrained by Sagittarius has yet to reach a consensus (e.g., Helmi 2004 argue for prolate shape, Fellhauer et al. 2006 for spherical, Johnston et al. 2005 for oblate, and triaxial in Law & Majewski 2010). Additionally, the complexities of replicating all observable properties at once are extremely difficult, such as the bifurcated tail (shown in Figure 1.3). As a (relatively large) minor merger, no other coherent stream in the Galaxy compares in size. Its approximate initial virial mass has been cited as $\sim 10^{10}\ M_{\odot}$ by Łokas et al. (2010), or a present-day total mass within 5 kpc of $\sim 10^{8}\ M_{\odot}$. It is thought to have been merging for $\gtrsim$6 Gyrs (Laporte et al. 2018), in agreement with the chemical abundance yields of Sagittarius dwarf stars (Mucciarelli et al. 2017).

Whereas the Sagittarius dwarf is best described as a minor merger (given the much bigger mass of the Milky Way), the last known major merger was recently identified to be around ∼10 Gyrs ago, when the Milky Way was considerably less massive. Gaia-Enceladus, or the Gaia Sausage (GES for short), is estimated to have

provided $\sim 6 \times 10^8$ $M_\odot$ in stellar mass and may have been the merger that formed the Galaxy's heated thick disk (Helmi et al. 2018; Helmi 2020), including contributing a large fraction of retrograde-orbit stars in the Solar neighborhood. Given the epoch at which this merger occurred, the mass ratio between the Milky Way and GES at that time was likely of order 4:1 (Gallart et al. 2019).

Unlike Sagittarius, the timescale of GES' disruption has been substantially longer, such that GES stars no longer form a coherent structure on the sky. However, its presence is still detectable as a signature in phase-space (i.e., positions and kinematics) of its member stars near the Sun. Belokurov et al. (2018) first observed the GES structure in velocity-space using a catalogue of stars in *Gaia* DR1 cross-matched to SDSS radial velocities. We show this detection in the first two rows of Figure 1.4. The panels in the top and middle rows of Figure 1.4 are the radial and azimuthal velocities for stars in *Gaia* DR1 at heliocentric distances within the Solar neighborhood (R_{helio} $<$ 10 kpc) where each panel represents a bin of increasing metallicity. As a separate entity to disk stars, which can be seen in every panel as a "blob" at positive v_ϕ, a kinematic structure (the "sausage", named for its unusual shape in velocity-space) emerges in the metallicity bins approaching -1.66 to -1.33 dex. In Belokurov et al. (2018), the authors concluded that such a structure was most likely the result of a single, massive, relatively radial accretion event.

Shortly thereafter, Helmi et al. (2018) used the second *Gaia* data release (*Gaia* DR2) cross-matched to APOGEE spectra (Apache Point Observatory Galactic Evolution Experiment; Majewski et al. 2017) to identify this same feature. The final bottom-most panel of Figure 1.4 showcase their detection of this feature in a modified velocity-space orientation. The authors highlight GES as the retrograde-motion thick disk stars which exhibit "halo-like" kinematics (stars within the teal ellipse) and chemical abundance traits. The chemical analysis is the most telling of these features − thick disk stars show a distinct track in [α/Fe] to [Fe/H] ratios separate to that of the thin disk. If these stars had been formed *in situ* within the disk, the trends in [α/Fe] vs [Fe/H] should similarly reflect this pattern. Thus, the chemistry appears to confirm the accreted nature of this structure.

Although this large merger event has clearly had an impact of the structure of the Galaxy, especially its disks and nearby halo, the coherent structures traced by smaller satellites can in many ways provide more handles on many aspects of our Galaxy, especially its stellar and dark halos.

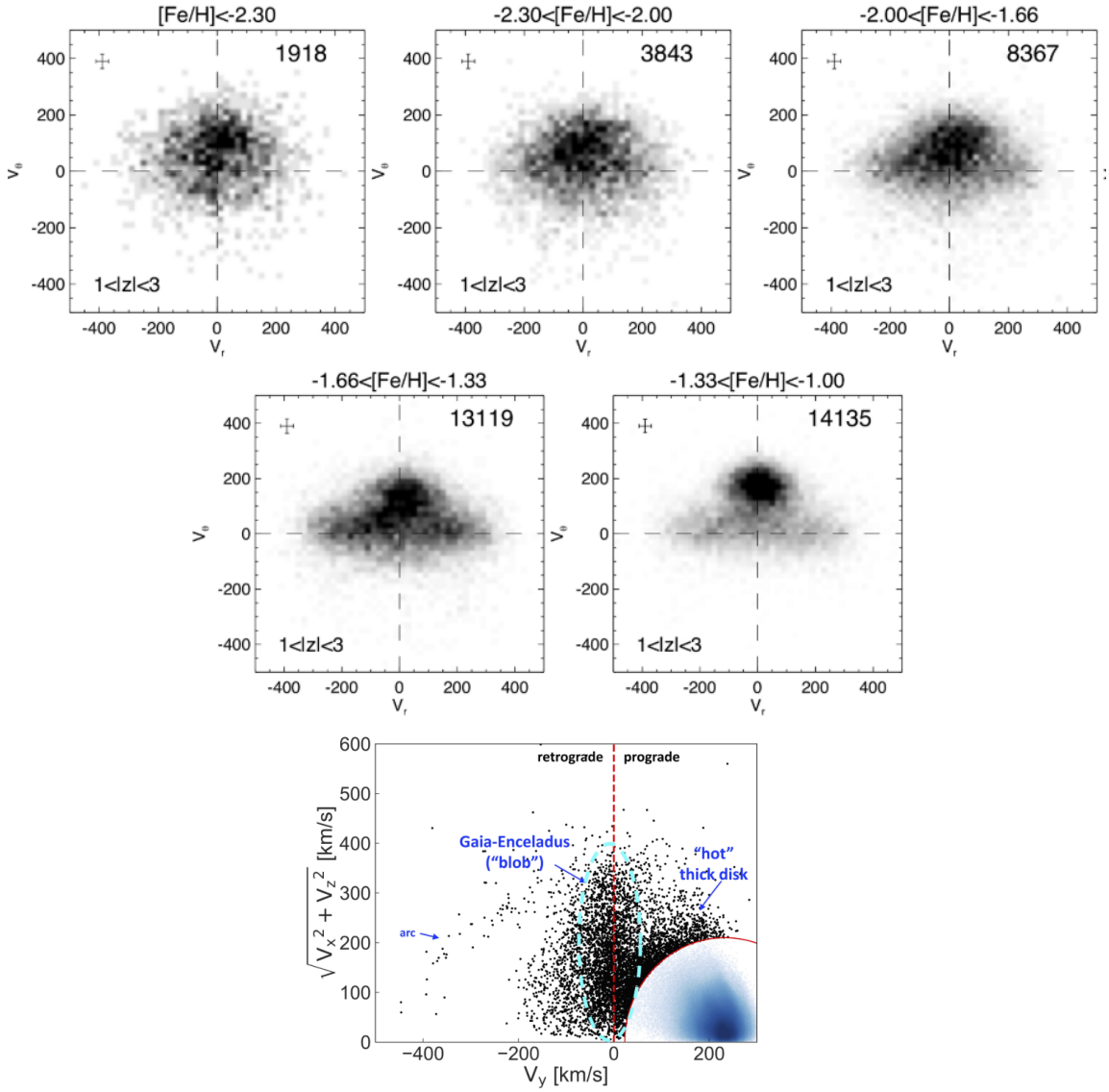

Figure 1.4: The discovery of Gaia-Enceladus (or Gaia-Sausage) in two detections. The first two rows are from Belokurov et al. (2018) where each panel show bins of increasing metallicities of stars at distances of $R_{helio} < 10$ kpc. The most metal-rich panels are in the middle row where the "sausage" shape clearly emerges at [Fe/H] = [-1.66, -1.33] dex. The ranges in z reference the height in the vertical (Galactic) plane. The final bottom-most panel is the detection of the Gaia-Enceladus from Helmi et al. (2018) where the disk stars are shown in blue contours.

1.3.2 Stellar Streams as Probes of the Halo

Stellar streams whose progenitors are globular clusters are much more common in the Galaxy (∼40 at R_{helio} < 45 kpc; Thomas et al. 2020) compared to those from massive dwarfs, though detecting them is generally more difficult. Due to their lower initial masses and velocity dispersions, the resulting stellar stream is usually thin and has a very low surface brightness (e.g. the Palomar 5 stream in Figure 1.3 compared to Sagittarius). However, these smaller satellites and their dynamically cold tidal tails are extremely sensitive to perturbations from their host's potential. Using these more numerous structures and tracing their morphologies yields promising results for constraining properties of dark matter at various distances in the Galaxy, as summarized in Bonaca & Hogg (2018).

Recent studies have implemented data-mining techniques to locate these thin stellar streams in the Milky Way. Equipped with the extensive source list in *Gaia* DR2, Malhan et al. (2018) developed the STREAMFINDER algorithm to attempt to identify stars on similar orbits but vastly separated on the sky. This method led them to detect many new stellar streams scattered across the Galaxy. Other works have implemented similar searches for structure within this survey (Mateu et al. 2018; Ibata et al. 2019; Necib et al. 2020; Borsato et al. 2020) and thus far, have largely appended the number of globular cluster stellar streams.

Perhaps the best test-case for the utility of globular cluster stellar streams is Palomar 5 (Pal 5; Odenkirchen et al. 2001) − one of the first streams detected from a globular cluster progenitor. The Pal 5 stream has been the subject of many interesting recent dynamical experiments; for example, Küpper et al. (2015) first used this stream to probe the dark matter halo shape at relatively large distances (R_{helio} = 21 kpc) using radial velocities of a handful of members, and SDSS data to construct a matched filter map of the stream. Their models accurately reproduce the kinematics of the present-day progenitor, and they conclude that the halo probed by Pal 5 is essentially spherical with mild flattening ($q_z \sim 0.95$, where $q_z < 1$ represents an oblate geometry). The authors also use the stream to calculate the mass of the Galaxy within the apogalactic radius (19 kpc) is $\sim 2.1 \times 10^{11}$ $M_\odot$. As a secondary result, the authors also obtained the distance to Galactic Center and rotational velocity at the Sun ($R_\odot = 8.3^{+0.24}_{-0.25}$ kpc, $v_{circ}(R_\odot) = 233^{+12.7}_{-10.0}$ km s^{-1}), citing values that agree with the latest observations (e.g., Gravity Collaboration et al. 2019; Eilers et al. 2019). In their work, Küpper et al. (2015) successfully demonstrated that Pal 5 and other dynamically thin

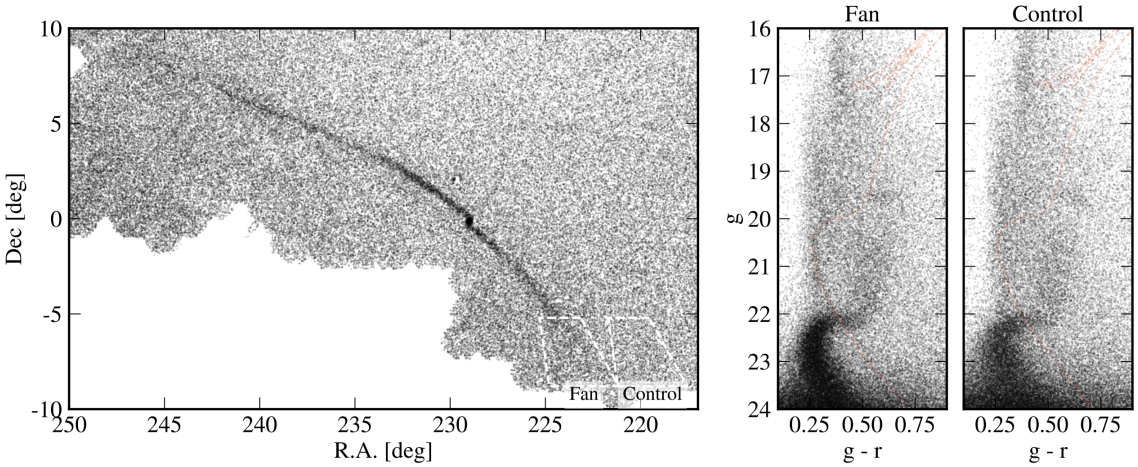

Figure 1.5: Palomar 5 morphology and fan structure from Bonaca et al. (2020). The color-magnitude diagrams show that the fan in the lower tidal arm occupies the same region as the isochrone fit to the globular cluster (represented as the faint orange line) shifted by distance. The control does not exhibit these features, suggesting the fan is indeed a real detection.

stellar streams are exceptionally useful to probe global properties of the Galaxy's halo.

Pearson et al. (2015) have also demonstrated that Pal 5 exhibits a fanning structure in the leading arm, or a shortening of one tail, as shown in Figure 1.5 (taken directly from Bonaca et al. 2020). In their simulations, no configuration of a triaxial halo could possibly fit the observed Pal 5 stream track based on its thin and curved morphology, allowing the authors to place an initial constraint on the halo's shape. In later works, Pearson et al. (2017) found that the best-fit halo configuration for this stream is one that is flattened ($q_z \sim 0.6$). They additionally find that the fanning structure can be reproduced when dynamical models include a rotating Galactic bar. While no work has yet been able to constrain all observed substructures in the stream track (wriggles, gaps, etc.; see Bonaca et al. 2020), study of its morphology is already yielding interesting insights into the Galaxy at large.

Pal 5 is just one example of the diverse science that can be derived with the morphology of distant, well-defined tidal tails. As the sample of globular cluster streams increases, so does our understanding of Galactic dynamics. Each stream represents a unique interaction with the Galaxy; therefore, charting nearby streams and exploiting their characteristics is necessary to develop a complete picture of the properties and evolution of our Galaxy.

The majority of stellar streams identified in recent years – especially those using

Gaia DR2 astrometry – are relatively local (<10 kpc; e.g., Malhan et al. 2019). In the Solar neighborhood, *Gaia* parallax errors are small and can be used to derive accurate distances. However, as the earlier simulations from Figure 1.2 show, we anticipate extensive substructure out to very large radii in the stellar halo. Indeed, it is here also that the properties of the dark matter halo (e.g, total mass) are less well-constrained due to a dearth of luminous tracers, and therefore newly discovered streams and substructures could provide the most significant constraints to these estimates. At these distances, *Gaia* parallaxes are essentially useless, though the proper motions are valuable if the angular velocities could be converted to physical velocities. The goal of this thesis is to push the discovery space of *Gaia* into the outer halo by combining *Gaia* DR2 with new wide-field photometry that is capable of identifying bright tracer populations at large distances, and independently providing the critical missing distances.

1.4 Thesis Outline

Our objective is to probe the vast charters of the Milky Way's stellar halo for interesting and distant structures that can help us better know and understand the properties of the distant Galaxy. In Chapter 2, we discuss the various large-sky surveys used in this work. These surveys allow us to identify tracer populations and obtain better distance estimates than *Gaia* can provide for distant objects. We investigate the overall clustering properties of the first of these bright stellar populations, blue horizontal branch (BHB) stars, in Chapter 3 via the OPTICS clustering algorithm, allowing us to visualize the hierarchical nature of halo substructures.

This initial analysis identifies one globular cluster in particular (NGC 5466) that allegedly hosts a stellar stream. The subsequent analysis of this feature forms the crux of the rest of the following chapters. Chapter 4 analyses the distribution of red giant branch (RGB) stars in the vicinity of the cluster to better trace the substructure suggested by the BHBs. We show that NGC 5466 is in fact a highly extended, very diffuse stellar stream. Chapter 5 presents a detailed analysis of the observed properties of the stream as traced by both the BHB and RGB populations. We show that the stream exhibits a very significant distance gradient, potentially making it an excellent tracer of the mass and shape of the distant halo. Chapter 6 presents new, simple, dynamical modelling of this stellar stream, which agrees with our observed data. A summary of our results, including a comparison of our findings for this cluster

compared to earlier results in the literature, is presented in Chapter 7.

Chapter 2

Data

Each old, metal-poor substructure found in the stellar halo forms part of the fossil record of our Galaxy. The arrival of the first two data releases from the *Gaia* space satellite (DR1 and DR2) provided detailed astrometry for stars beyond the Solar neighborhood, including excellent proper motions for stars at very large (>10 kpc) distances. It is in this region of the Galaxy that the stellar halo dominates; however, *Gaia*'s parallax uncertainties here are generally extremely poor. Our approach is to use ancillary ground-based data − particularly the unparalleled u-band imaging from the Canada-France Imaging Survey (CFIS) − to obtain photometric parallaxes that surpass *Gaia*'s angular parallaxes for very distant stars. This chapter describes the surveys, catalogues, and stellar populations used in this thesis.

2.1 Principal Surveys

2.1.1 *Gaia*: the "Astrometric Solution"

The advent of digital large-sky surveys in the optical (e.g., SDSS by York et al. 2000; PS1 by Chambers et al. 2016), provided a wealth of data on stars in the Galaxy that is prime for exploration. Most recently, Galactic archaeology has been impacted significantly by *Gaia* and subsequent discoveries from the first and second data releases. The primary objective of this mission is to obtain five-parameter astrometry (positions, proper motions, and parallaxes) for approximately 1% of all stars in the Milky Way (Gaia Collaboration et al. 2016a), thus creating a precise and detailed map of the Galaxy. Even by the first data release in 2016, *Gaia* had determined parallaxes and proper motions for 2 million stars, extending the Hipparcos astrometric source

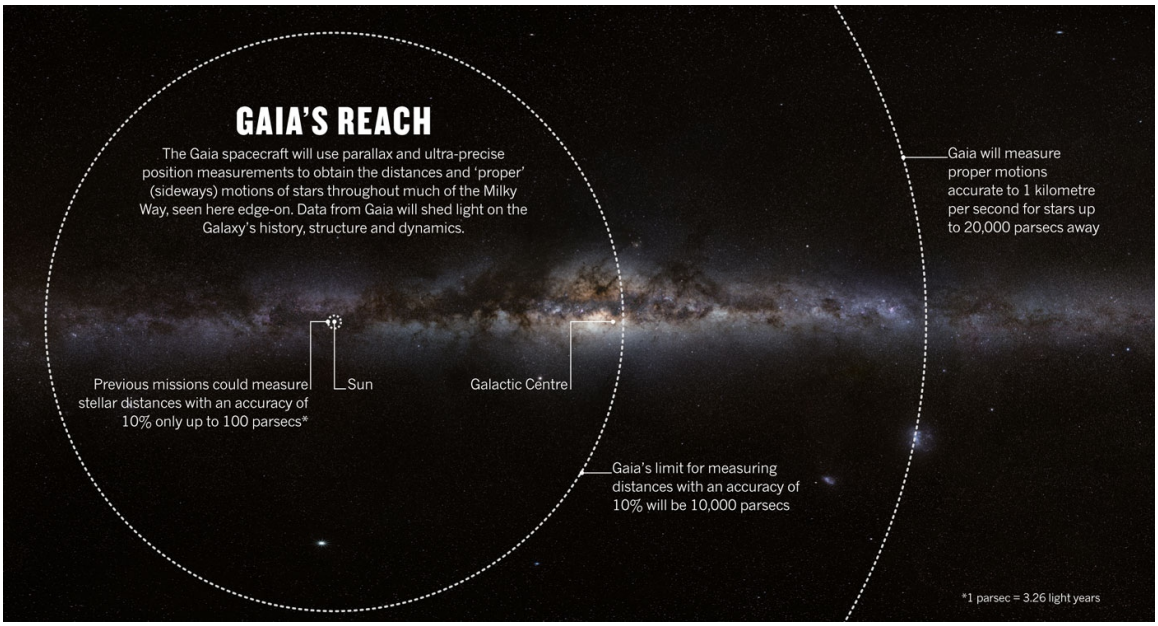

Figure 2.1: *Gaia* uncertainties relative to heliocentric distances, directly from Powell (2013). The innermost circle shows the radius at which HIPPARCOS achieved parallax uncertainties of 10%. In comparison, the middle radius shows the limit where *Gaia* obtains the same order of parallax uncertainties, or distances up to 10 kpc. The outermost circle shows where *Gaia* reaches proper motion errors of ∼10% at ∼20 kpc.

list by a factor of >16 with an accuracy 200 times better than that of its predecessor (Gaia Collaboration et al. 2016b).

Figure 2.1 highlights this remarkable advancement, not only with respect to *Gaia*'s radial extent compared to HIPPARCOS, but also the measurement uncertainties that are achieved at large distances. *Gaia* obtains parallax uncertainties of 10% up to ∼10 kpc, and similar proper motion uncertainties up to ∼20 kpc. The accuracy of *Gaia*'s astrometry is crucial to understanding kinematics of stars and their orbits, which can reveal the Galaxy's dynamics and formation over time. The unique and unprecedented data from this satellite indicates that the present is a golden era for Galactic exploration.

Subsequently in 2018, the second *Gaia* data release (*Gaia* DR2; Gaia Collaboration et al. 2018) became publicly available. This updated dataset boasts substantial advancement in both the number of observed stars and the accuracies of individual measurements. DR2 contains five-parameter astrometry for *1.3 billion* sources, of which on-board radial velocities were observed for 7 million (for $G \leq 12$ mag).

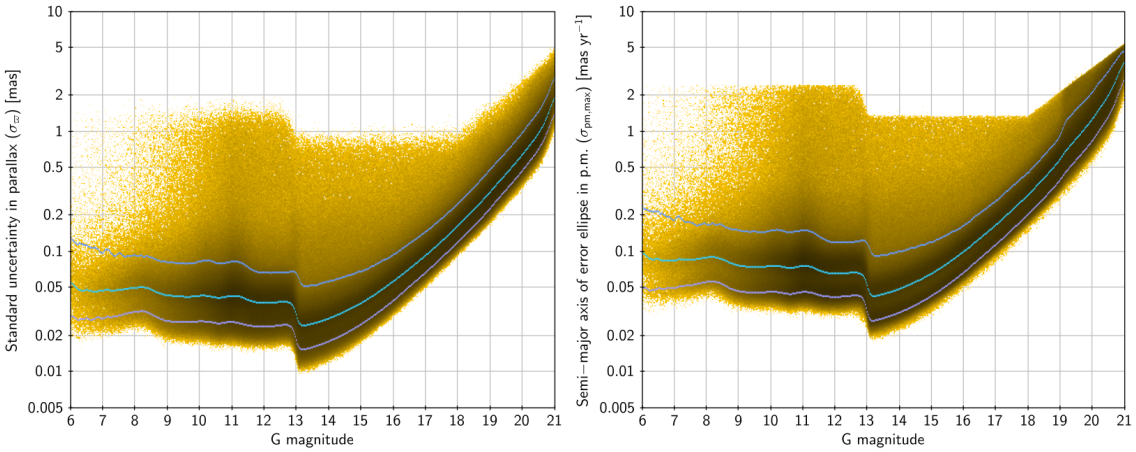

Figure 2.2: *Gaia* DR2 uncertainties for parallax (left panel) and proper motion (right panel) as a function of *G*-band magnitude for sources with five-parameter astrometry (directly from Lindegren et al. 2018). The median uncertainty is shown as cyan lines; the 10th and 90th percentiles are represented in blue.

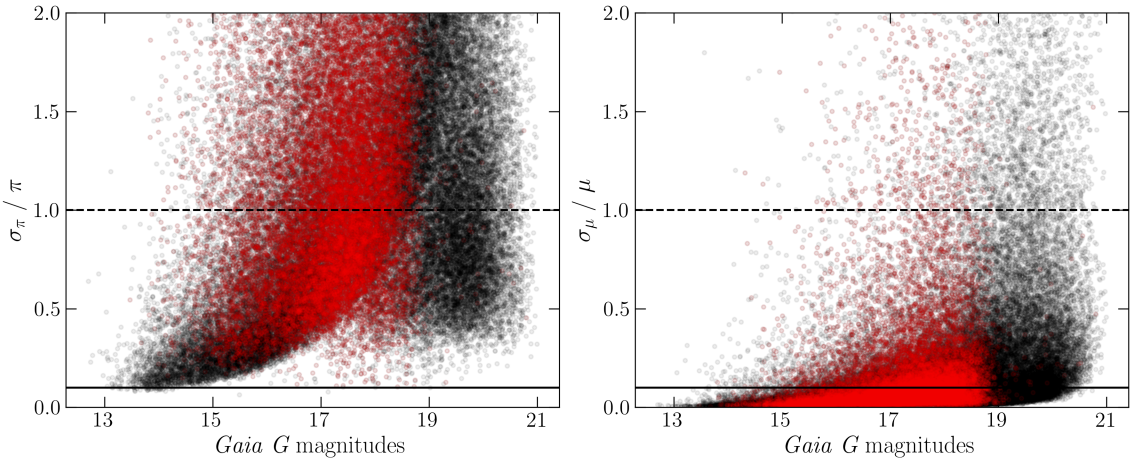

Figure 2.3: Percent errors of red giants (whose percent parallax errors are $\leq$200%) identified in CFIS. Their astrometric errors are shown as a function of *Gaia G* magnitude. Parallax errors are shown in the left panel, while the semi-major axis of the error ellipsoid for proper motions are shown on the right. Red points represent giants from R_{helio} = [10, 20] kpc. The black solid line represents 10% errors while the dashed is of the order of measurement.

Additionally, *Gaia* DR2's uncertainties are better than that of DR1 by an order of magnitude (Lindegren et al. 2018). We show in Figure 2.2 the absolute errors for all *Gaia* DR2 sources as a function of G-band for which five-parameter astrometry is available.

The enhanced accuracy of *Gaia* DR2 has motivated a wealth of recent studies relating to the substructure of our Galaxy. These include (1) searches for stellar streams (Malhan et al. 2018; Mateu et al. 2018; Ibata et al. 2019; Necib et al. 2020; Borsato et al. 2020), (2) updated globular cluster kinematics (Baumgardt et al. 2019) (3) identification of tidal tails from globular clusters (Bianchini et al. 2019; Kundu et al. 2019; Sollima 2020), (4) new estimates for the Milky Way mass profile (Cautun et al. 2020), and (5) unveiling the Galaxy's complex accretion history (Helmi et al. 2018; Mackereth et al. 2019), among many other advancements.

Gaia has certainly provided many of the pieces necessary to better understand the Galaxy's past, especially with respect to the extended Solar neighborhood. However, as previously shown in Figure 2.1, the parallax uncertainties for fainter sources are not as well constrained as the proper motions. We highlight this point in Figure 2.3, which shows the variation of astrometric errors as a function of *Gaia* G-band for a sample population of red giants. For all G magnitudes, the size and spread of uncertainties in proper motion errors are considerably smaller at any given magnitude than the parallax. This is especially true for giants between $10 - 20$ kpc (shown in red) that are most likely to reside in the outer disk and stellar halo.

Given the poor parallaxes in *Gaia* for stars in the stellar halo, we opt to use photometric parallaxes for specific tracer stellar populations that are identified using the u-band from CFIS (Ibata et al. 2017a). By combining CFIS distances and *Gaia* proper motions, we are able to explore the 5-D kinematics of the outer Galaxy, where *Gaia* data by itself is insufficient.

2.1.2 The Canada-France Imaging Survey

CFIS is an on-going Large Program using the Canada-France Hawaii Telescope (CFHT) MegaCam imager. When completed, the survey will have ground-based u- and r-band photometry for 10,000 and 5,000 deg^2 of sky, respectively. The survey is partially motivated by the *Euclid* mission, whose measurements of the distant Universe rely on accurate photometric redshifts (Ibata et al. 2017b). However, the primary motivation for the extensive CFIS-u imaging is its power for local studies of nearby stellar pop-

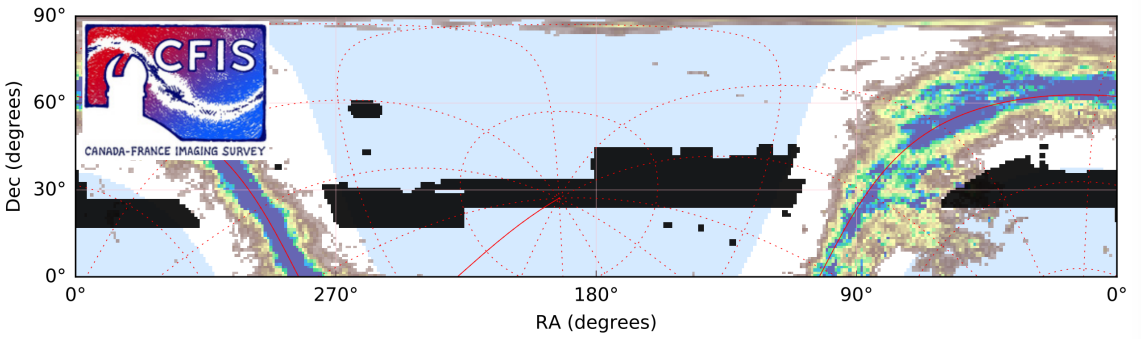

Figure 2.4: Equatorial footprint of the Canada-France Imaging Survey taken directly from Ibata et al. (2017a). Black regions show the u-band in DR1, and the blue background shows the expected final coverage when the survey is completed.

ulations. The survey footprint (as seen in Figure 2.4) is focused at Galactic latitudes of $|b| > 19°$, and is therefore well-suited for studying the halo.

Historically, deep u-band imaging is challenging to obtain (e.g., the transmission curve of SDSS falls dramatically in the blueward spectrum; see Figure 2 of Ibata et al. 2017a). The discrepancy is primarily caused by two factors: firstly, atmospheric absorption is much stronger in the blue. Secondly, telescopes and instruments achieving broad wavelength coverage across the optical spectrum generally experience less transmission in these regions unless clear design decisions were made to optimize the system for short wavelengths (in which case, throughput in the red will be affected). These factors generally result in costly exposure times to attain comparatively sensitive u-band imaging.

However, CFIS-u achieves similar photometric depth to the gri-bands of SDSS, and in fact, is deeper than u_{SDSS} by 2.7 magnitudes. This feat is a direct result of longer integration times on a relatively larger telescope, which is much more optimized in the UV by design (e.g., optical coatings) compared to other facilities. In this respect, CFIS leverages a niche characteristic of MegaCam at CFHT and the Large Program format for innovative science. We quantify this gain in the top panel of Figure 2.5, which compare the photometric uncertainties as a function of magnitude between the CFIS and SDSS. The superiority of CFIS-u is evident, and the practical effects of this difference are shown in the color-magnitude diagrams (CMD) of NGC 5466 in the bottom panels.

CFIS photometry was collected using a new, large u-band filter that illuminates all 40 MegaCam CCDs (in comparison to the previous filter set that did not illuminate the four CCDs that form the "ears" of MegaCam; see Figure 3 of Ibata et al. 2017a).

Sequences of three dithered 80s exposures were used, where each sub-exposure is offset by a third of a field in both the north-south and east-west directions. Due to the irregular shape of the MegaCam field, this method results in at least 240s exposure per field for most of the survey, while 10% obtains a total of 320s due to the overlapping "ears".

In relation to nearby stellar populations, the *u*-band is exceptionally useful as it contains an abundance of information relating to Galactic archaeology. For example, a star's absolute magnitude is sensitive to its metallicity, and many metal lines are found in the UV-blue region of the spectrum. This fact is particularly useful to photometrically identify target populations and derive basic parameters, including distances. By targeting specific stellar populations for which the absolute magnitude is well-constrained, we can obtain better distance uncertainties than those of *Gaia* in the halo. Accurate photometric distances paired with excellent proper motions gives us a more complete kinematic view of the Galaxy.

The current CFIS footprint sets the sky coverage, but the depth of the *u*-band is more than sufficient to complement the *Gaia* dataset. In the following sections, we describe the methods used to identify key tracer populations using CFIS.

2.2 Identifying Stellar Tracer Populations

2.2.1 Blue Horizontal Branch Stars

The first tracer population analyzed in Chapter 3 is the blue horizontal branch stars identified in Thomas et al. (2018). BHBs are an ideal tracer as they are present in old stellar populations and exhibit bright, stable absolute magnitudes ($M_g \sim 0.5 - 0.7$ mag; Deason et al. 2011). These blue giants can be traced out to large Galactocentric distances ($R_{gal} = 5 - 220$ kpc, i.e. visible far into the halo), achieving global distance uncertainties of order ∼10% and therefore outperforming *Gaia*'s parallax uncertainties beyond the Solar neighborhood.

BHBs are A-type giants ranging in temperatures from $T_{eff} \approx [7500, 9000]$ K. To identify these stars using photometry alone, Thomas et al. (2018) first used color-color diagrams to select the hotter A-types in the CFIS footprint. The photometric dataset consisted of the extinction-corrected CFIS *u*-band and PS1 *griz*-bands. Thomas et al. (2018) note that a single cut using (u_0 - g_0) vs (g_0 - r_0) is insufficient to identify the hotter A-types without also having considerable contamination from cooler stars, and

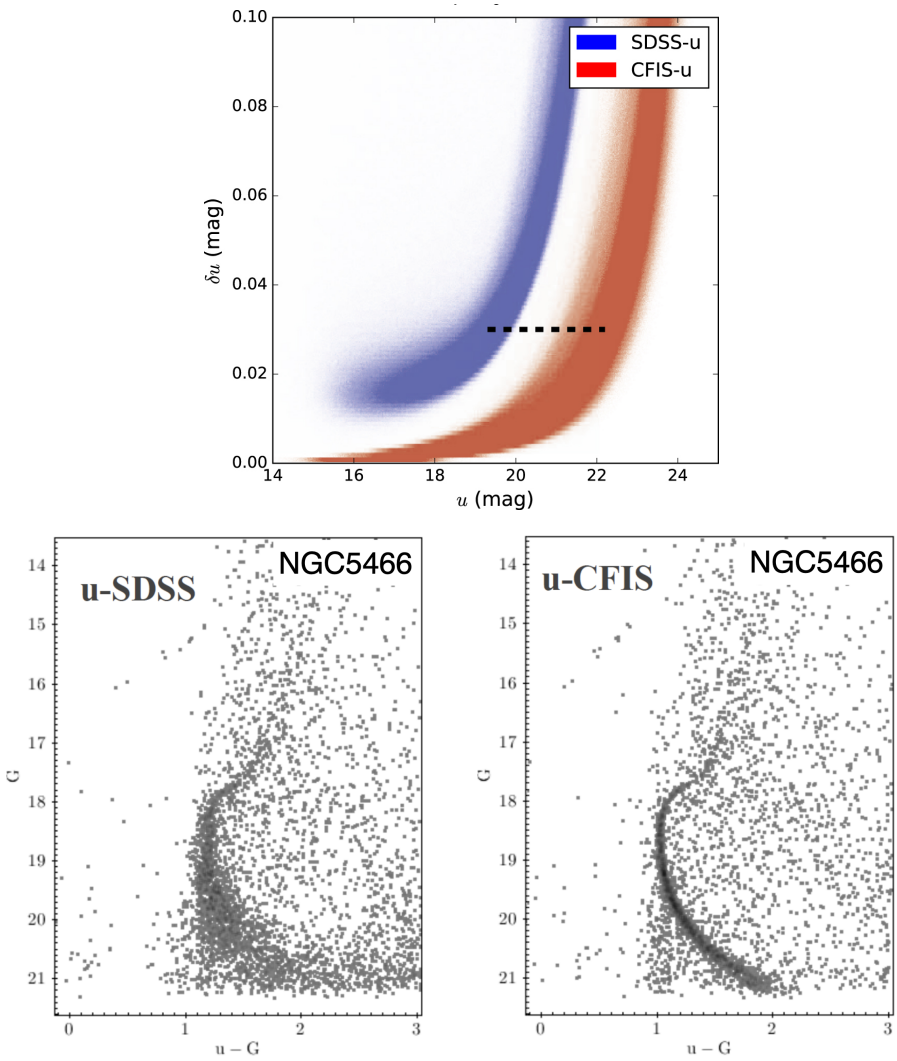

Figure 2.5: Top panel shows the photometric uncertainties in the u-band versus magnitude, taken from Ibata et al. (2017a). The CMDs of NGC 5466 in the bottom panels showcases the depth and purity of the u-band compared to SDSS.

that multiple color-color combinations are required. Figure 2.6 shows the resulting series of color-color diagrams where the orange polygon highlights the selection made in each panel.

The highlighted branches in Figure 2.6 contain BHBs (red) and contaminating blue straggler (BS) stars. In a globular cluster, BSs are higher mass main sequence (MS) stars that populate the CMD beyond the main sequence turnoff. They are similarly A-types and are often a source of contamination when selecting BHBs using photometry alone. To disentangle these two populations, Thomas et al. (2018) trained a Principal Component Analysis (PCA) algorithm on the colors of known BSs and BHBs. This sample of stars had been spectroscopically identified in Xue et al. (2011) and cross-matched to CFIS-PS1. Given the colors (u_0 - g_0), (g_0 - r_0), (r_0 - i_0), and (i_0 - z_0) for each star, the PCA is trained to identify the most relevant features (colors) for segregation between the labels (BS or BHB).

Thomas et al. (2018) found that the three most significant components (P_1, P_2, P_3) could be used to define an effective boundary between BSs and BHBs. This allows us to define a region in principal component space populated predominantly by one population or the other. The equation used to determine a star's principal components from its photometry is:

$$\begin{pmatrix} P_1 \\ P_2 \\ P_3 \\ P_4 \end{pmatrix} = \begin{pmatrix} -0.6397 & -0.7669 & 0.0493 & -0.0149 \\ -0.6479 & 0.5353 & -0.2283 & -0.4916 \\ -0.3964 & 0.3141 & 0.0040 & 0.8626 \\ -0.1181 & 0.1633 & 0.9723 & -0.1183 \end{pmatrix} \cdot \begin{pmatrix} u_0 \text{ - } g_0 \\ g_0 \text{ - } r_0 \\ r_0 \text{ - } i_0 \\ i_0 \text{ - } z_0 \end{pmatrix} \tag{2.1}$$

in which the matrix is determined by the trained PCA. The populations are segregated using a function relating (P_2 - P_3) vs P_1, given as equation 4 in Thomas et al. (2018). We show this boundary in Figure 2.7, where it is clear that the two populations are successfully separated with only very modest contamination. Figure 2.8 further demonstrates the success of this algorithm for five globular clusters in CFIS where the highlighted orange box represents the location of all true BHBs. The aforementioned separation is applied to the CFIS-PS1 A-type stars, yielding a clean sample of $\sim$10,200 BHBs with contamination of $\lesssim$25%.

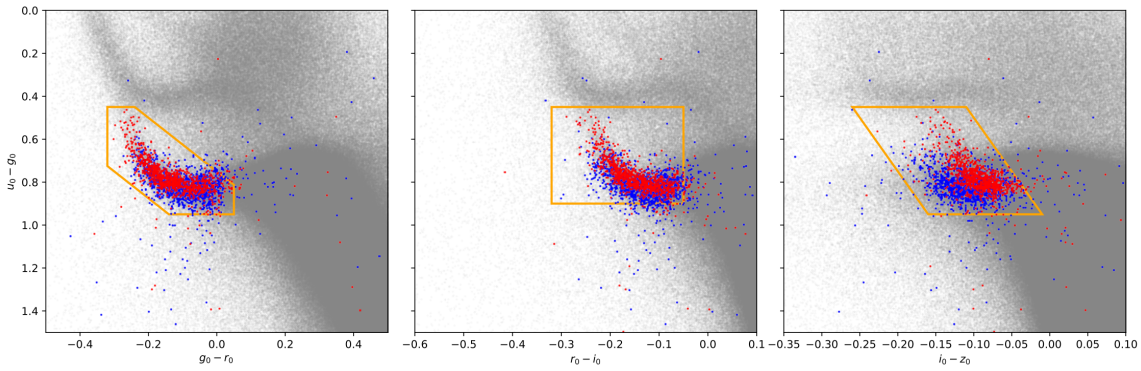

Figure 2.6: Identification of A-type stars in CFIS directly from Thomas et al. (2018). CFIS-PS1 data are shown in grey. The orange box represents the selection of A-type stars made in each color-color diagram. The spectroscopically identified BSs and BHBs from Xue et al. (2011) are shown in blue and red, respectively. Each band is extinction-corrected.

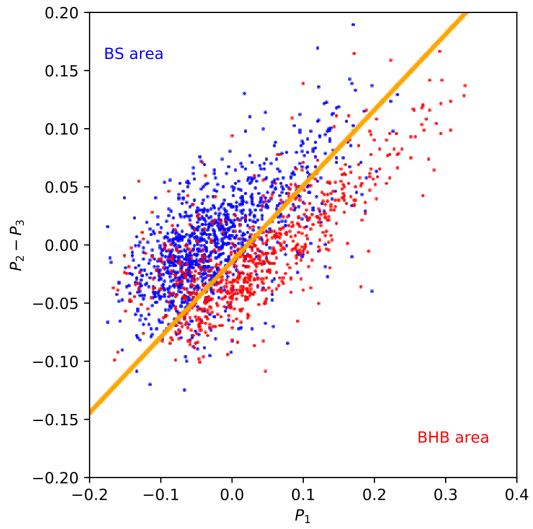

Figure 2.7: BHB and BS principal component boundary, as seen in Thomas et al. (2018). Blue and red points are as in Figure 2.6.

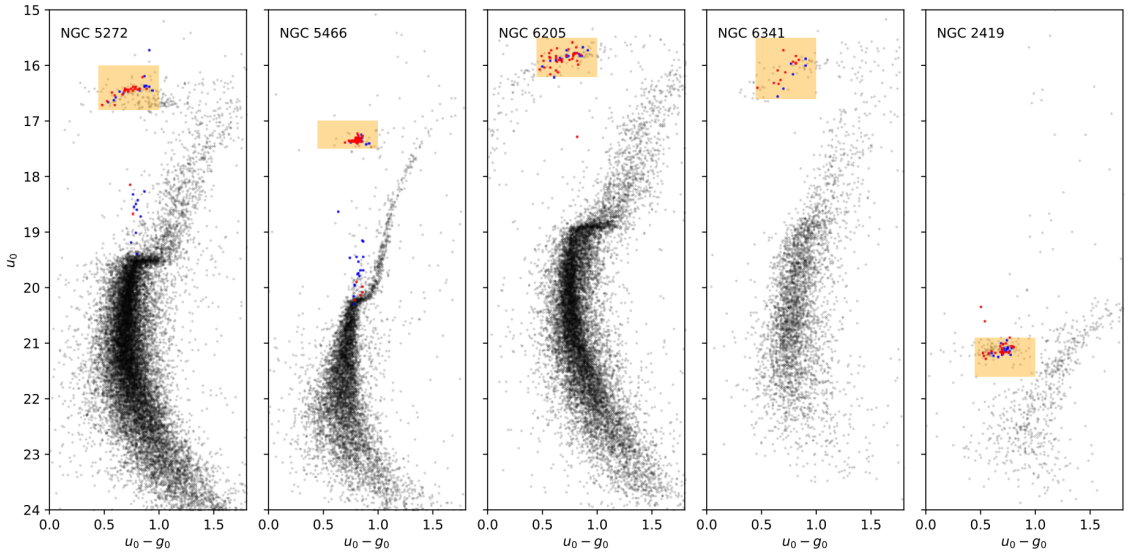

Figure 2.8: CMDs of five known globular clusters in CFIS, taken directly from Thomas et al. (2018). Blue and red points are as in Figure 2.6; the orange box highlights the location of all true BHBs.

2.2.2 Red Giant Branch Stars

The second tracer population analysed in Chapter 4 are red giant branch stars, selected from a catalog of dwarfs and giants (hereafter, "D+G"). For 12.8 million sources, Thomas et al. (2019) implemented machine learning to classify stars as either dwarfs or giants, then estimate their photometric metallicities and distances. The advantage of this method is the reliance on photometry alone in this classification, which normally requires spectroscopic data. This method is therefore significantly less expensive, allowing us to obtain a much larger sample of giants.

It is well known that distances can be estimated from photometry alone, under the assumption that the sources are MS stars, since the color can then be used to predict the absolute magnitude (e.g., Jurić et al. 2008). The photometric metallicity of these stars can also be estimated with careful analysis (Ivezić et al. 2008), which is otherwise a source of systematic uncertainty when determining distances. Ibata et al. (2017b) use this premise to estimate the overall spatial metallicity distribution of the Milky Way as seen with CFIS by firstly assuming all stars in their study are MS. From a statistical standpoint, this is an acceptable approximation since most stars in the Galaxy are on the main sequence. However, giants misidentified as MS will result in underestimated distances of 150% (or M $\simeq$ 3 mag; Thomas et al. 2019).

In order to address this source of uncertainty in photometric studies of the Galaxy's structure, Thomas et al. (2019) trained an algorithm to distinguish dwarfs (MS) from giants (primarily RGBs) based on input photometry. The authors combined the CFIS-PS1 *ugriz*- with *Gaia G*-band photometry to obtain excellent color information for millions of stars across the optical spectrum (λ = [3200, 11000] Å; see Figure 2 of Thomas et al. 2019). The algorithm first implements a Random Forest Classifier (RFC) trained on a cross-matched sample of known MS and RGBs from SDSS/SEGUE (Yanny et al. 2009). The features provided to the RFC were the extinction-corrected colors $(u - g)_0$, $(g - r)_0$, $(r - i)_0$, $(i - z)_0$, and $(z - G)_0$. The RFC then assigns probabilities for each star, where $P_{dwarf} = 1 - P_{giant}$, to classify their population. The authors note that the most significant colors in the classification are $(r - i)_0$ and $(u - g)_0$, where the implied sensitivity of the former is caused by the effective temperature, and the latter to a star's metallicity.

After the RFC classifies the two populations, Thomas et al. (2019) then predict the metallicities ([Fe/H]) and absolute magnitudes in *Gaia G* (M_G) by implementing two sets of Artificial Neural Networks (ANN) on the dwarfs and giants, separately. The

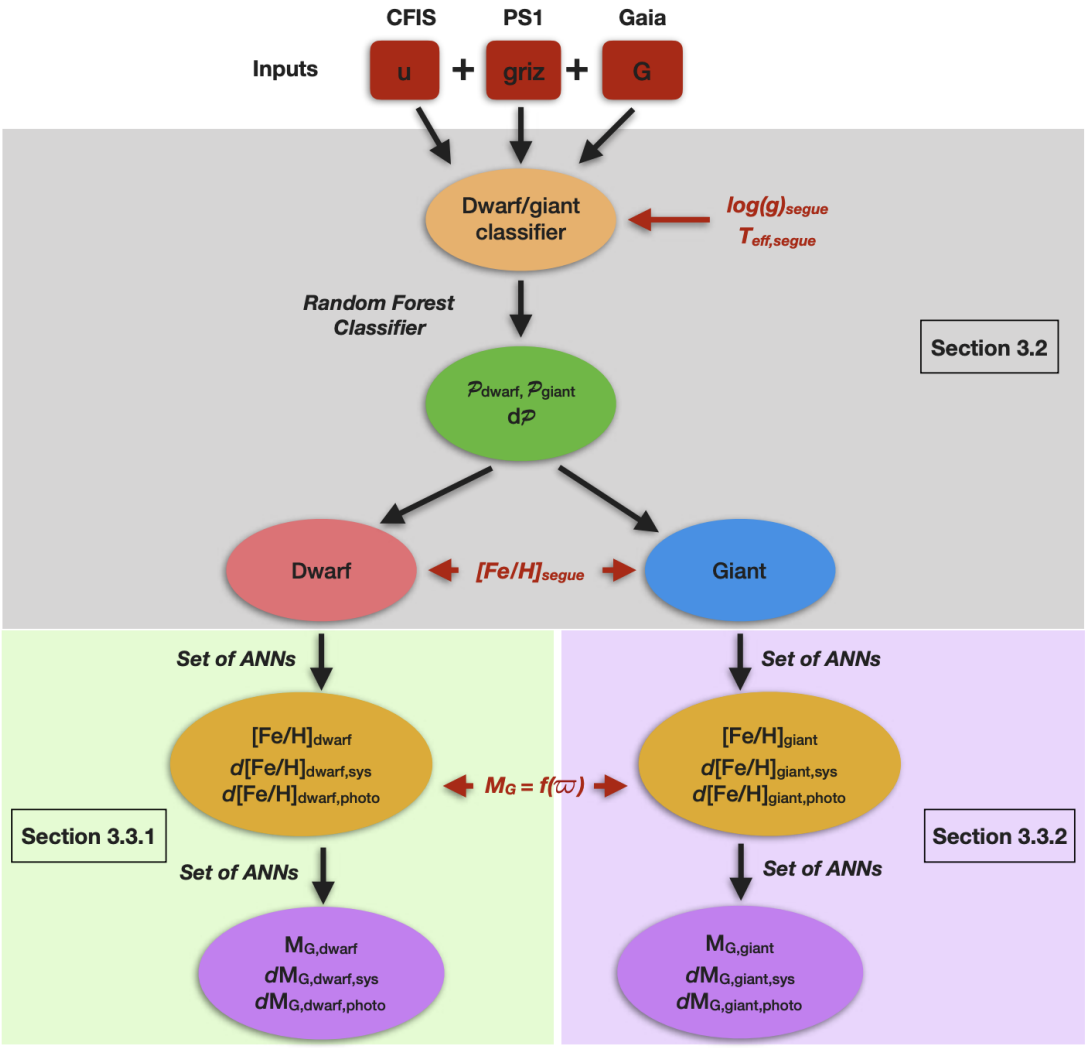

Figure 2.9: Schematic of the D+G algorithm taken directly from Thomas et al. (2019).

labels fed to the training set are SEGUE [Fe/H] and M_G. We show the schematic of the entire algorithm in Figure 2.9, which is applied to the CFIS-PS1-*Gaia* dataset after training on the SEGUE sample. The algorithm successfully identifies 70% of metal-poor giants up to [Fe/H] $<$ -1.2 dex, with distance uncertainties of typically better than $\sim$25%. The authors note that more metal-rich giants are often misidentified, resulting in a significant drop in completeness for [Fe/H] $>$ -1. This minimally affects our work as we are primarily concerned with giants in the metal-poor regime.

Figure 2.10 shows the resulting spatial-resolved metallicity distribution for dwarfs and giants from Thomas et al. (2019). The bottom panels show the highest confidence members, whose probabilities are >70%, resulting in nearly 136,000 giants (bottom left panel) and 11.2 million dwarfs (bottom right), respectively. These plots emphasize the successful segregation between the two stellar populations and the relatively accurate distances that are derived. In what follows, we rely on the RGBs as a tracer population to probe the outer regions of the Galaxy. While they are not traced to such a large radius as the BHBs, they are are an order of magnitude more numerous ($\sim$61,000 giants available) and photometric metallicities are available for the full sample.

The BHBs and RGBs of the CFIS footprint arm us with significant tracers to explore the stellar halo. In the following chapter, we probe the spatial distribution of the BHBs from Section 2.2.1.

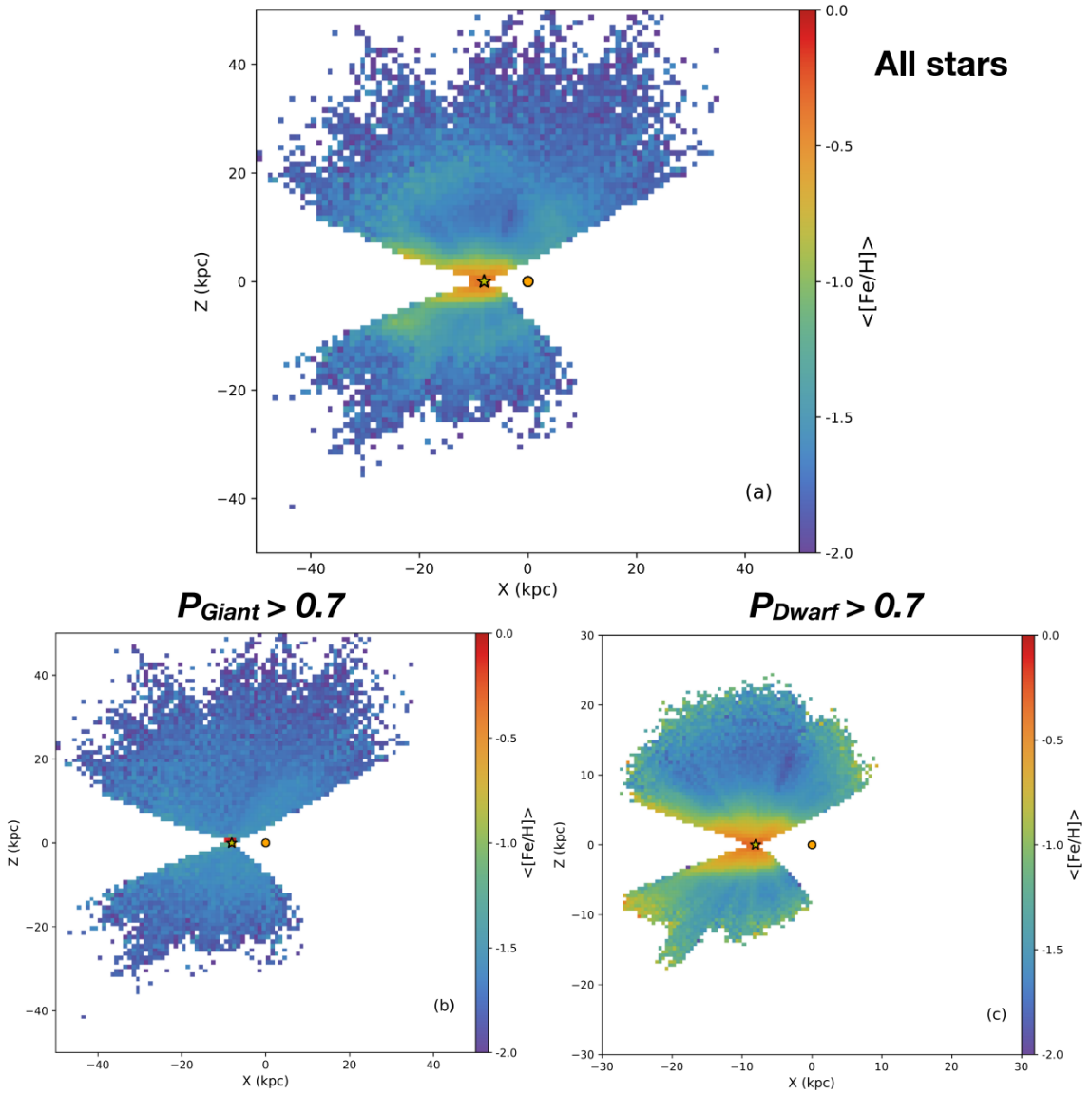

Figure 2.10: Galactic metallicity gradient for all D+G stars (top panel; 11.1 million sources) and high probability giants (bottom left; 136,000) and dwarfs (bottom right; 11.2 million) taken from Thomas et al. (2019).

Chapter 3

Exploring the Outer Halo with Blue Horizontal Branch Stars

The blue horizontal branch population identified in the CFIS footprint enables us to explore substructure far out into the stellar halo. This tracer population was identified by Thomas et al. (2018) and has been used to quantify the halo's global shape out to ∼220 kpc, nearly twice as far as other recent studies using alternative stellar tracers. The density profile that they determined implies an oblate inner halo (<41.4 kpc) and a steeper slope in the outer region with constant flattening $q_z \sim 0.9$ across all radii, in agreement with the literature.

While *Gaia* DR2 performs well in the Solar neighborhood, it lacks the ability to measure parallaxes to the same accuracy as proper motions for fainter, more distant, stars. By utilizing the BHB catalogue, which boasts excellent distance uncertainties (∼10%), we achieve accurate distance measurements in the Galaxy where *Gaia*'s performance is hindered. Cross-matched to *Gaia* proper motions, this produces an unrivaled dataset for investigating the distant halo. In this chapter, we explore the prominent structures revealed using the BHB dataset and identify one in particular that forms the focus of this thesis.

3.1 Stellar Clustering in the Halo

3.1.1 Linking a Galaxy's Accretion History with its Stellar Halo Density Profile

ΛCDM cosmology predicts that many mergers occur between galaxies at early times in the Universe, and at later times a galaxy's evolution is much more passive. In the Milky Way, the stellar halo is the graveyard of these cannibalized accreted structures. Remnants of these events can survive for billions of years as their distances from the Galaxy are large, resulting in long orbital timescales. Many of the satellites that are accreted are observed to be metal-poor, and as they approach pericenter with the Milky Way, tidal forces act to strip away mass. Stars that become unbound from their satellite will then instead orbit the Galaxy, forming stellar streams, tidal tails, and/or diffuse substructures.

The shape of the stellar halo is directly linked to the accretion history, which can be quantified via the observed density profile. Our Galaxy is known to contain many distant substructures (e.g., see the recent review by Helmi 2020 and the book edited by Newberg & Carlin 2016). Estimates of the total stellar mass within halo substructures are of order $[1.5 \pm 0.4] \times 10^9$ $M_\odot$ within 100 kpc (Deason et al. 2019) give or take a factor of two, and depending on the tracer population used (see Deason et al. 2011 and Bell et al. 2008 for comparative studies using BHBs). The smoothness of the profile changes with time, and becomes lumpier with a more active accretion history as satellites merge and are tidally stripped. Key information to understand the assembly of the stellar halo is therefore contained in global parameters such as its shape and dispersion in stellar density at large distances.

Many recent studies examined the shape of the halo using star counts of various tracers, such as RR Lyrae (Watkins et al. 2009; Hernitschek et al. 2018), K-giants (Xue et al. 2015), and BHBs (De Propris et al. 2010; Deason et al. 2014). Deason et al. (2011) found early on that the shape is best described with a broken power law profile, where the inner halo (<20 kpc) is more steep than outer radii, but defined by constant flattening ($q_z \sim 0.6$). However, the steepness of these parameters is still under debate and changes depending on the tracer and completeness of the sample. In addition, most studies do not extend further than 100 kpc.

Thomas et al. (2018) recently disentangled the BHB population within the CFIS footprint to trace the halo to remarkably large distances. They determined the profile

to be a broken power-law:

$$\rho(\mathrm{m}) = \rho_{\odot} \begin{cases} (R_{\odot}/m)^{\gamma}, & \text{for m} \leq r_b \\ (R_{\odot}/r_b)^{\gamma-\beta}(R_{\odot}/m)^{\beta}, & \text{for m} > r_b \end{cases} \tag{3.1}$$

such that the inner halo slope is $\gamma = 4.24 \pm 0.08$ changing to $\beta = 3.21 \pm 0.07$ in the outer halo, at a break radius of $r_b = 41.4$ kpc. Here, we use this same sample of stars – that extend to large Galactic radii, have minimal contamination from BSs (<25%), and exhibit high completeness – to investigate halo substructure at large distances.

3.1.2 OPTICS Spatial Clustering Algorithm

Our objective in this chapter is to identify substructure in the stellar halo using the BHBs from Thomas et al. (2018). To observe clustering in this catalogue, we require an algorithm that (a) must be effective at handling relatively large datasets, and (b) must operate with minimal assumptions about the number or properties of the substructure present. Requirement (b) automatically eliminates the possibility of implementing partitioning algorithms, such as *k*-means.

An alternative to partitioning is connectivity-based clustering. One of the most popular methods of connectivity-based clustering is the Friends-of-Friends (FoF; Huchra & Geller 1982) algorithm. FoF relies on a specified linking-length l such that any point q within a radius l surrounding the first point p is classified as a "friend". The algorithm then moves to q and searches again for any new members within l thus building a network of these points to form a group. Cluster bounds are dependent on the algorithm's exhaustion of new datapoints that fit this criterion.

Another method commonly implemented in data mining in general is DBSCAN (*Density-Based Spatial Clustering of Applications with Noise*; Ester et al. 1996), a density-based clustering method. DBSCAN resembles FoF but identifies clusters by comparing the relative density of a cluster against the background. The user defines two values: N_{min}, or the minimum number of points to consider it a cluster, and ϵ, which is the characteristic radius. If for a given point, p, there are $\geq \mathrm{N}_{min}$ points within a ϵ radius, then this region is considered a seed for a cluster (i.e. a core point).

DBSCAN relies on specifying a given physical scale to identify a base cluster, but the substructures we expect to find in the stellar halo will have a range of spatial scales. For this reason, we chose to implement an extension of DBSCAN known as *Ordering Points to Identify Clustering Structure* (OPTICS; Ankerst et al. 1999).

OPTICS is better suited for our needs in comparison to DBSCAN; although it does not segregate the data into clusters, it produces a dendrogram for analysis by the user that shows the hierarchical structure of the dataset. As such, OPTICS only requires the specification of one parameter, N_{min}.

The unique and advantageous approach OPTICS provides is the convenient dendrogram known as a "Reachability-Diagram". This plot allows the user to visualize the hierarchical density structure within the dataset, i.e. structures within structures are easily observed. Given that the halo is an amalgamation of streams, clusters, and various other overdensities, OPTICS is well-suited for exploring the Galaxy. Recently introduced to astronomy, OPTICS has already been used to observationally quantify the hierarchical nature of the Andromeda galaxy-M33 system (McConnachie et al. 2018) and tested with simulations of the Milky Way stellar halo (Sans Fuentes et al. 2017).

The resulting Reachability-Diagram depends largely on the size of N_{min}, which again represents the minimum number of points within a cluster for it to be considered significant or "real". Selecting larger values of N_{min} will produce a smoother dendrogram, potentially overlooking small-scale structures, whereas smaller values of N_{min} will result in a fairly noisy output.

All points in the dataset have a Euclidian distance from a given point p to another point q, or dist(p, q). In this space, the core distance, or d_c, is defined as the distance from p to the nearest N_{min}-th point. The algorithm calculates the "reachability-distances" (hereafter, RD) of every p to q within a cluster. The RD is defined as follows:

$$\mathrm{RD}(p,\,q) = \begin{cases} d_c, & \text{if } d_c \geq dist(p,q) \\ dist(p,q), & \text{if } d_c < dist(p,q) \end{cases} \tag{3.2}$$

Neighbors are thus defined as the closest points to p in which the RDs beyond d_c are small. OPTICS then organizes the data based on an "order" with respect to the RDs of the neighborhood. Once a neighborhood has been explored, the algorithm moves on to the next and repeats until all points have been examined.

The dendrogram produced by OPTICS from the ordered RDs provides unique insight into the structure of datasets. Substructures stand out as valleys against the background density; thus, hierarchical structuring is evident as a representation of valleys within valleys. Figure 3.1 (taken directly from Sans Fuentes et al. 2017) shows

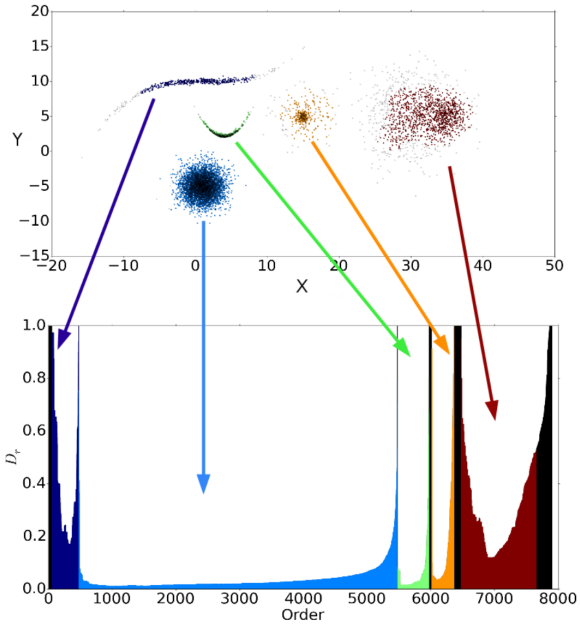

Figure 3.1: OPTICS-identified clusters from Sans Fuentes et al. (2017). The data are 8,000 2-D points representing structures similar to those found in the Galaxy's stellar halo, shown in the upper panel. The bottom panel is the resulting Reachability-Diagram, where the RDs on the y-axis are normalized with respect to the maximum and minimum RD values.

a mock 2-D halo for which various substructures identified by OPTICS are highlighted in the Reachability-Diagram. The y-axis has been normalized with respect to the maximum and minimum RDs (see equation 3 in Sans Fuentes et al. 2017). Each structure illustrates a separate valley within the dendrogram.

3.2 BHB Substructures in the Stellar Halo

3.2.1 Prominent Clumps Identified by OPTICS

We applied OPTICS to the northern Galactic region of the BHB dataset ($b > 20°$; red points of Figure 3.2) where each point is transformed to its Galactocentric coordinates (X, Y, Z), and we set $N_{min} \geq 6$. We chose this value for N_{min} as it is sufficient to identify small-scale structures in the BHB survey (for example, known globular clusters) and does not produce a significant number of spurious detections.

The resulting Reachability-Diagram is shown in the central panel of Figure 3.3. The x-axis represents the order, or index, of the BHBs within the reorganized dataset.

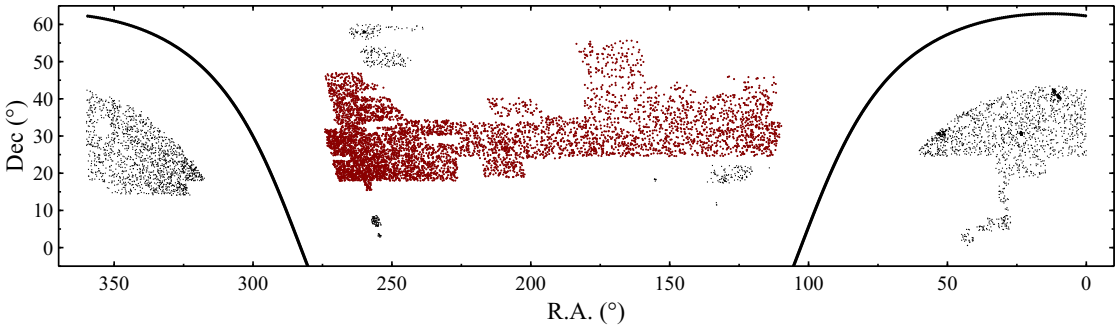

Figure 3.2: The CFIS-PS1 BHB footprint. The red points in the northern region ($b > 20°$) are the focus of our analysis. The Galactic plane is shown as the black line for reference.

As a result, data physically located near other points in a neighborhood are represented with similar indices and appear close together on the x-axis. The y-axis depicts the RDs of each star, in essence showing the general scale of structures in each neighborhood.

The valleys of Figure 3.3 show neighborhoods where RDs of stars in these structures are small compared to the background. OPTICS does not automatically define clusters, so we used an algorithm from McConnachie et al. (2018) to identify which indices define the bounds of valleys, otherwise referred to as "peaks". From a hierarchical standpoint, all valleys in the Reachability-Diagram are branches of smaller and smaller clustering compared to the Galaxy's background distribution. In this manner, each peak represents locations of segmentation within a parent cluster and every peak has at least one potential sub-cluster on the left or right index.

Before applying the algorithm, we chose to smooth the Reachability-Diagram with a Gaussian where the FWHM is equal to $N_{min}/2.5$. This acts to remove excessively small "clustering" caused primarily by poisson-like statistics.

The largest "algorithmically-identified" valleys are shown as the highlighted regions of Figure 3.3. We identified each of these structures as prominent satellites found in the literature (Harris 1996, 2010 edition; McConnachie 2012; Grillmair & Carlin 2016) by examining the on-sky positions of each valley's member stars. Of the six highlighted valleys, five are associated to known globular clusters and one to a tidally disrupting dwarf galaxy (Boötes III). In addition to these highlighted valleys, smaller features are also visible in the Reachability Diagram. The broadest of these (between M92 and M13, or approximately between BHB indices 1800 - 2000) is an artefact of

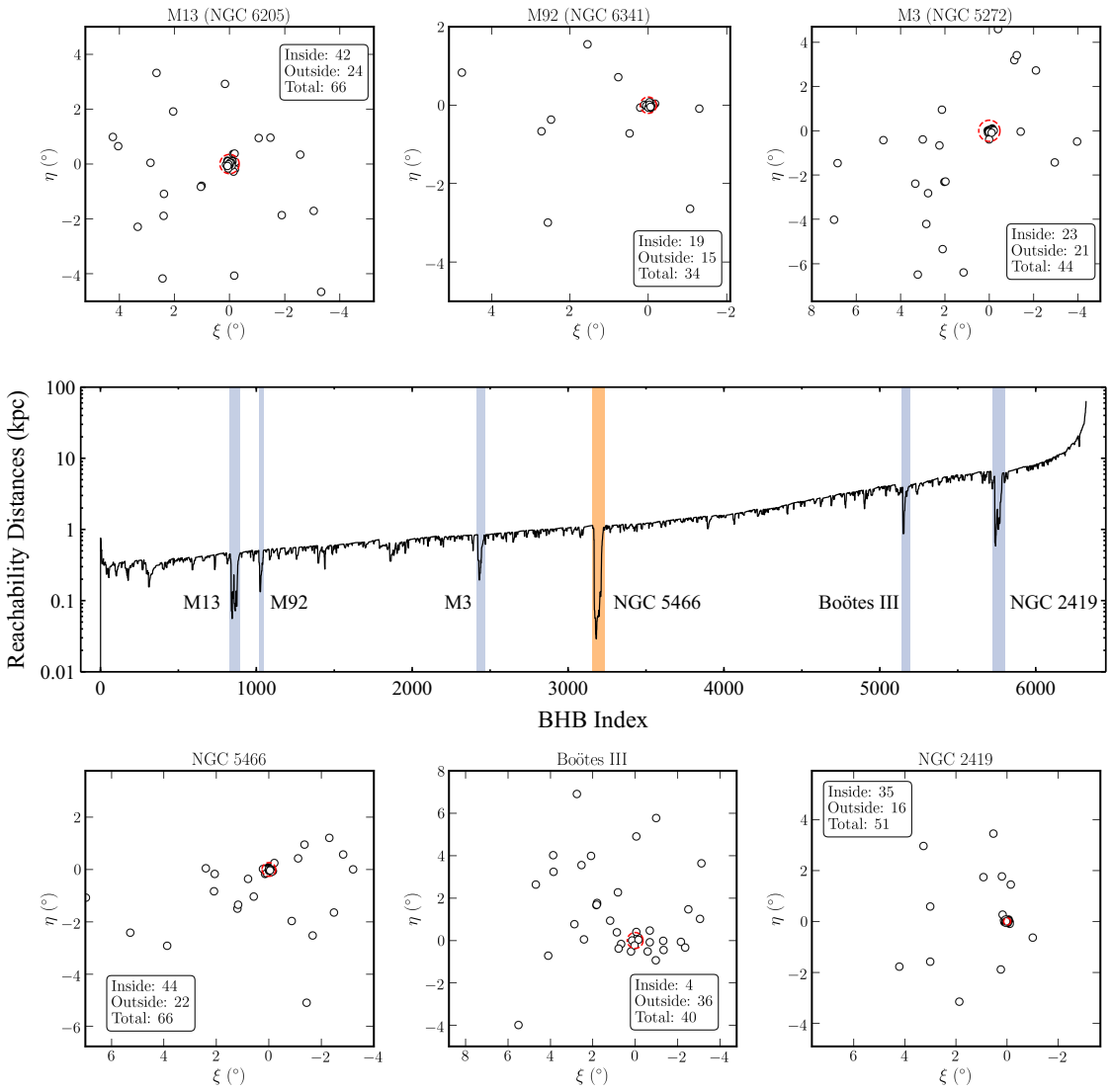

Figure 3.3: The resulting dendrogram produced by OPTICS (central panel) and the identified known satellites (surrounding smaller panels) that are highlighted in the Reachability-Diagram. The valleys in the Reachability-Diagram show the neighborhoods with low reachability distances (i.e. close physical clustering) and therefore high probability of being associated to a unique cluster. Top and bottom rows show the tangent plane of each cluster where the tidal radius (or in the case of Boötes III, the half-light measured in Carlin et al. 2009) as a red dashed circle. Statistics for each object are listed describing the number of BHBs inside and outside r_t (or r_h).

the cone of observation, caused by the CFIS limit in galactic latitude above the disk.

The surrounding panels of Figure 3.3 are the tangent-plane projections of the member stars in each valley, centered on the each of the known satellites' positions. We additionally show the King tidal radii (r_t; Moreno et al. 2014) as a red dashed circle for each globular cluster. In the case of Boötes III, we show the half-light radius measured in Carlin et al. (2009). We emphasize that a significant number of OPTICS-identified BHBs lie well beyond the tidal radii of these satellites. If any of these stars are physically associated to the main body, this suggests notable mass loss. We summarize recent findings for each of these objects below:

- M13 (NGC 6205): Lehmann & Scholz (1997) find a "halo of unbound stars", in reference to the excess surface density in the King profile. Leon et al. (2000) similarly find an extension of stars towards the galactic center. However, these stars all lie within the tidal radius.

- M92 (NGC 6341): Sollima (2020) and Thomas et al. (2020) determined the cluster exhibits tidal tails, with the latter paper identifying lengthy extensions of $\sim$17°.

- M3 (NGC 5272): Two papers (Leon et al. 2000; Grillmair & Johnson 2006) searched for stripping surrounding this cluster but do not find any evidence of disruption.

- NGC 2419: This particular globular cluster is argued to have originated from the Sagittarius dwarf galaxy (Bellazzini et al. 2020). At a distance of 82.6 kpc (Harris 1996, 2010 edition), the current tidal forces experienced by this cluster will be quite weak.

- Boötes III: This dwarf galaxy is currently being tidally disrupted, and is the likely progenitor of the Styx stellar stream (Grillmair 2009; Carlin et al. 2009; Carlin & Sand 2018).

- NGC 5466: Evidence for mass loss was first presented in Pryor et al. (1991) and Lehmann & Scholz (1997). Grillmair & Johnson (2006) identified an extensive structure from the globular cluster extending 45° using SDSS data. The cluster also appears in the SDSS "Field of Streams" from Belokurov et al. (2006a), who suggest that a stream is also apparent in their data, but extending only 4°.

3.2.2 Tidal Debris of NGC 5466

In the following stage, we explored these potential substructures by examining the kinematics of their putative BHB members using *Gaia* proper motions of each star. As anticipated, BHBs inside r_t showed tight groupings in proper motion space. However, a few objects revealed stars outside of the tidal radius whose proper motions are consistent with that of their satellite. In this respect, NGC 5466 is particularly compelling.

Figure 3.4 shows the OPTICS-identified BHBs for NGC 5466. The left panel represents a zoom-in of the tangent plane as seen in Figure 3.3 and the right is the associated absolute proper motions whose error bars are reported by *Gaia* DR2. We corrected the proper motion errors by a factor of 1.1, as Lindegren et al. (2018) showed these values are typically underestimated by $7 - 10\%$ for fainter sources ($G > 16$ mag).

The right panel of Figure 3.4 shows a clear clustering of points corresponding to the systemic proper motions of NGC 5466. The centroid of these points (outlined with a green dashed circle) is the proper motion of the cluster ($\mu_\alpha*$, μ_δ) = (-5.41, -0.79) mas yr^{-1} derived by Baumgardt et al. (2019) using the *Gaia* DR2 catalogue.

Interestingly, there are six BHBs outside r_t whose proper motions are consistent with stars in the main body of the cluster. We highlight these points in both panels of Figure 3.4 as cyan stars. To show the true motion of the cluster and BHBs, we corrected the proper motion vectors for Solar reflex motion. The values we implemented are the Schönrich et al. (2010) Local Standard of Rest (LSR) velocities $[U,V,W]_\odot$ = [11.1, 12.24, 7.25] km s^{-1}. We assume the Sun's position in the Galactocentric frame is (X, Y, Z) = (-8.122, 0, 0.025) kpc (Gravity Collaboration et al. 2019; Jurić et al. 2008) with a circular velocity of 229 km s^{-1} (Eilers et al. 2019). The arrows in the left panel show the scaled and Solar-corrected vectors of each BHB. The overall motion of the cluster is represented as the red vector for comparison.

The highlighted BHBs in the left panel of Figure 3.4 are clearly moving in a similar fashion as the globular cluster itself, thus suggesting these co-moving stars may be tidally stripped from NGC 5466. This would be consistent with results from Grillmair & Johnson (2006) and Belokurov et al. (2006a), who both find evidence for a stream, albeit with significantly different extensions. Indeed, a closer examination of the literature surrounding NGC 5466 motivates us to better understand this structure. We describe the main features of this distant cluster below.

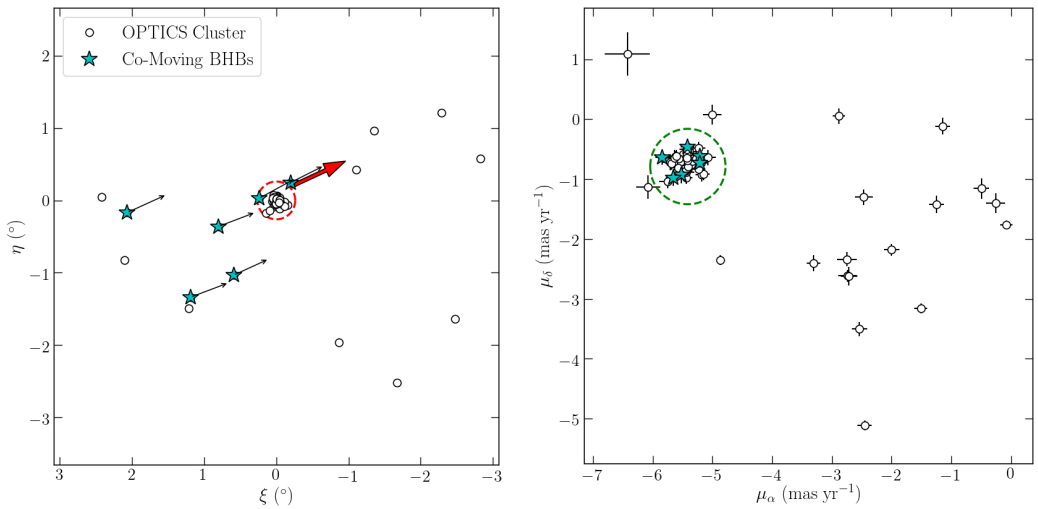

Figure 3.4: A zoom-in of the OPTICS BHBs identified as NGC 5466 (orange valley in Figure 3.3). BHBs outside the tidal radius (red dashed circle in the left panel) are shown as cyan stars. The left panel shows the tangential plane centered on the globular cluster. Black arrows show the true proper motions of candidate BHBs in this plane corrected for Solar reflex motion, while the red arrow represents the true motion of the cluster (estimates from Baumgardt et al. 2019). The right panel shows the absolute proper motion-space of the cluster BHBs where the green circle is the region we define as the proper motion clump. Stars within this circle are likely members of NGC 5466.

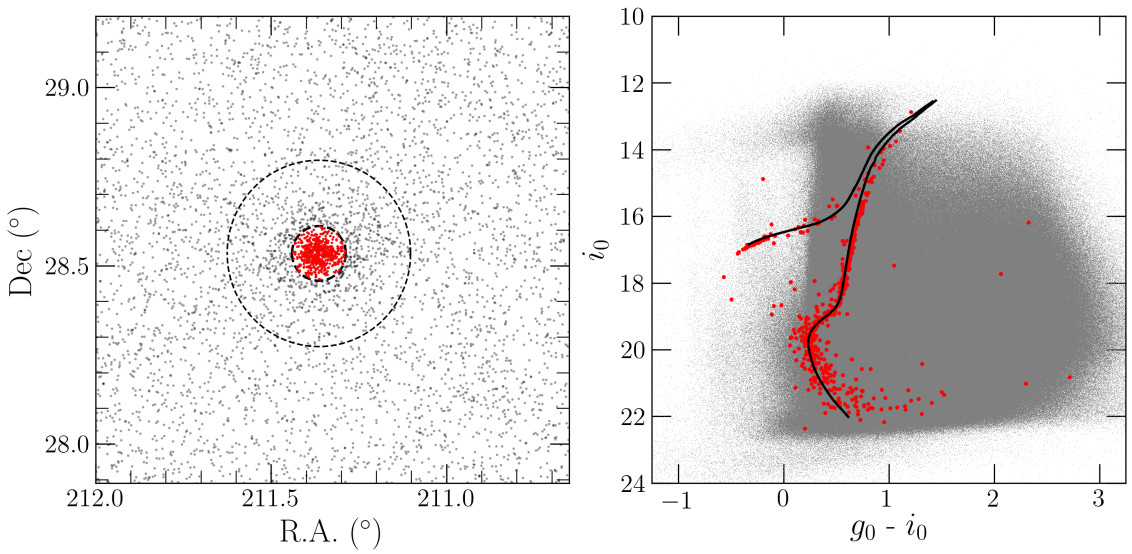

Figure 3.5: The left panel shows NGC 5466 as seen in the CFIS-PS1 dataset where stars within $2r_h$ of the center are red. The outer-most dashed circle highlights the tidal radius of NGC 5466. In the right panel, a PARSEC isochrone has been fit to the CMD of the cluster points using extinction-corrected magnitudes.

3.2.3 The Galactic Globular Cluster NGC 5466

NGC 5466 is a metal-poor ([Fe/H] = -1.98) Galactic globular cluster located at a heliocentric distance of 16 kpc (Harris 1996, 2010 edition). We provide a summary of the cluster's relevant parameters compiled from the literature in Table 3.1. Briefly, it is a low-concentration, faint, and distant cluster residing at high galactic latitude (l, b) = (42°, 73°) and exhibits negligible reddening. The cluster as viewed in the CFIS-PS1 catalogue is shown in Figure 3.5 where red points are stars within 2 half-light (r_h) radii. We estimate the age of the cluster to be ∼12.88 Gyrs as determined with a PARSEC (Bressan et al. 2012) isochrone fit to this data.

Several studies over the years have shown evidence that NGC 5466 has tidal tails, albeit of varying length. The first instance originated from Lehmann & Scholz (1997) who noted a "halo of unbounded stars" as an excess surface density in the cluster's King profile. Odenkirchen & Grebel (2004) later found similar results as an evident tidal perturbation in APM data, and suggested that the cluster likely experienced tidal shocks after a recent passage through the galactic disk. Likewise, Belokurov et al. (2006a) located extended debris in SDSS and determined the tails to be 4° in total length.

Source	Parameter	Value
Harris (1996, 2010 edition)	α	211.3637°
	δ	28.5344°
	R_{helio}	16.0 kpc
	c	1.04
	r_h	2.3 arcmin
	r_c	1.43 arcmin
	[Fe/H]	-1.98
Moreno et al. (2014)	r_{tidal}	72.98 pc
Pryor et al. (1991)	Mass	5E4 $M_\odot$
Baumgardt et al. (2019)	μ_α*	-5.41 mas yr^{-1}
	μ_δ	-0.79 mas yr^{-1}
	v_r	106.93 km s^{-1}
This work	age	12.88 Gyr
	X_{gal}	-4.95 kpc
	Y_{gal}	3.03 kpc
	Z_{gal}	15.35 kpc
	pericenter	6.4 kpc
	apocenter	43.0 kpc
	ε	0.74

Table 3.1: Observational and kinematic properties of NGC 5466 summarized from the literature and results of this work. Galactic positions are given in the right-handed coordinate system (i.e., the Sun is at X_{gal} = -8.122 kpc).

Of the most recent observations, Grillmair & Johnson (2006) used an optimized matched filter technique on SDSS data to observe the tidal tails, citing a lengthy expanse of 45° across the sky. Multiple dynamical studies have since tried to model the cluster's disruption (Fellhauer et al. 2007; Lux et al. 2012), but have failed to fully replicate these lengthy tails. In particular, the farthest reaches of the leading arm (R.A. $< 192°$) could not be reproduced.

The repeated difficulty in simulating the full extent of NGC 5466 suggests that better observations must be made on the progenitor and its tails. At present, no specific, individual stars have been confirmed as members of the putative stream, and additionally, no follow-up observational studies exist beyond the initial discovery papers. Therefore, the parameters of the tails such as length, kinematics, and distances, are not well-constrained. Our small sample of BHBs presents an interesting study, as these possible members are the first for which proper motions and distances are available. Secondly, both previous models used pre-*Gaia* estimates for the globular cluster's proper motions, and it is possible that the updated values may impact dynamical studies of this feature.

However, the putative properties of the tidal tails of NGC 5466 are compelling in a broader context. If the tails are indeed as long as the Grillmair & Johnson (2006) detection claim, NGC 5466 one of a handful of exceptionally long globular cluster stellar streams in the Galaxy (second only to GD-1, for which no progenitor is apparent at present; Grillmair & Carlin 2016; Malhan et al. 2019). Any satellite is sensitive to the total mass of the Galaxy within its orbit, and NGC 5466 is very distant. As a globular cluster stellar stream with such long tails and a well-defined progenitor, NGC 5466 is a unique probe to test the potential and dynamics of the halo at these large radii.

In the past decade, the stream from NGC 5466 has been largely ignored, likely due to the difficulties in reproducing its putative properties. Various groups probed *Gaia* DR2 kinematics for stellar streams (Malhan et al. 2018; Mateu et al. 2018), but none have rediscovered the NGC 5466 stellar stream. Given the observational history of this feature, its potential usefulness for better constraining the mass of the Galaxy, and the difficulty multiple groups have had in dynamically reproducing the observations, we decided to further explore the properties of the NGC 5466 stream as revealed in the CFIS data. The BHB catalog provides compelling evidence that there is indeed a stream, but the relatively short lifetimes of these stars mean that they are a rather sparse tracer. In the next chapter, we employ another tracer population

identified in CFIS to determine if these can better illuminate the properties of this enigmatic halo substructure, and try to determine if the tails extend even a fraction as far as observed by Grillmair & Johnson (2006).

Chapter 4

Uncovering the Distant Red Giants of NGC 5466 and its Stellar Stream

In the previous chapter, we identified a co-moving group of BHBs in the vicinity of NGC 5466 and hypothesized that these are extra-tidal stars of the globular cluster. This result agrees with past studies who observed tidal tails emanating from the cluster to various lengths. Due to our limited number of identified members, we presently are unable to classify this structure as a stream.

Furthermore, the discrepancy in length between these detections prompts questions about the actual parameters of this object (for example, what is the stream's true morphology and kinematics?), which can only be answered by tracing more member stars. Here, we expanded our tracer population to include the red giant branch stars identified in CFIS. Given that the duration of the RGB evolutionary phase is longer than that of the BHBs, they are a potentially useful and numerous tracer of halo substructure to moderately large Galactocentric radii.

The CFIS RGB stars were originally identified in Thomas et al. (2019), referred to as the "D+G" ("dwarf" + "giant") catalogue. This dataset contains a large population of RGBs (∼600,000) in CFIS whose metallicities and absolute magnitudes are predicted via machine learning methods. Cross-matched to *Gaia* DR2, this provided us with 5-D parameters (positions, distances, and proper motions) and metallicity information for each star. In this chapter, we search the catalogue for RGBs in the vicinity of NGC 5466 and detect a well-defined stream extending from the progenitor globular cluster.

4.1 Selection of Target Stars

The D+G catalogue is a dataset in which MS stars ("dwarfs") and RGBs ("giants") are identified in the CFIS footprint using each star's photometric information from cross-matched CFIS-PS1-*Gaia* G data. The algorithm's proficiency in classifying these two stellar populations is crucial to then derive other parameters, in particular metallicity and absolute magnitude. We provide a more detailed description of the machine learning aspect of this algorithm in Section 2.2.2.

The probability of being a "dwarf" or "giant" in this catalogue is determined by the RFC, where $P_{giant} > 50\%$ suggests a star is an RGB. This first selection criterion results in 600,000 stars (5% of the entire D+G catalogue).

To remove background galaxies, we implemented the PS1 criterion in Farrow et al. (2014) which relies on the point spread function (PSF) and aperture fluxes. The basic concept is that resolved and unresolved sources can be identified based on the shape of their light profile. In a given band, a galaxy's light distribution is more extended than a stellar PSF. The latter is essentially constant whereas the former will change depending on the properties of the galaxy. Stars therefore form a tight locus when one examines the differences in their magnitudes measured in different apertures. We used the PS1 r-band for star/galaxy classification where the stellar locus is identified by $\mid r_{PSF} - r_{ap} \mid < 0.05$. The authors note that this method becomes unreliable at fainter magnitudes, specifically for $r_{PSF} > 21$ mag. However, the primary restriction in photometric depth in the D+G catalogue is due to *Gaia*'s limiting magnitude ($G \approx 21$ mag; see Figure 2.2). Most sources in this catalogue (99.9%) are brighter than $r_{PSF} = 21$ mag.

After applying this measure to remove background galaxies, the sample is reduced to ∼314,000 giants. However, an artefact imparted by the RFC is the misidentification of more metal-rich stars. Following the recommendations given in Thomas et al. (2019), we removed this contamination by restricting the uncertainties of the predicted absolute magnitudes ($\delta \mathrm{M}_{G,pred}$). The limiting uncertainty is $\delta \mathrm{M}_{G,pred} \leq 0.5$ mag where $\delta \mathrm{M}_{G,pred}$ includes the photometric and systematic errors added in quadrature. This results in a sample of ∼201,000 giants.

We apply a final cut to the *Gaia* parallaxes to avoid nearby stars in the Solar neighborhood, as described in Lindegren et al. (2018). This equates to a parallax cut at >0.2 mas or comparatively, removing stars whose heliocentric distances are less than 5 kpc. Gaia Collaboration et al. (2018) also recommend a zero-point correction

of -0.03 mas to account for global parallax underestimation. Therefore, we adopt:

$$\frac{1}{\pi + 0.03 \text{ mas}} > 5 \text{ kpc} \tag{4.1}$$

providing us with a total of ∼103,000 RGBs with positions, proper motions, distances, and metallicities.

4.2 Searching the Outskirts of NGC 5466

NGC 5466 is a well-studied globular cluster (Castellani et al. 1973; Nemec & Harris 1987; Pryor et al. 1991; Harris 1996, 2010 version; Arellano Ferro et al. 2008; Beccari et al. 2015; Baumgardt et al. 2019) and consequently, its global parameters for the main body are relatively well-established (summarised in Table 3.1). In this section, we search for RGBs whose parameters are consistent with the main properties of NGC 5466 to identify any stars that may be members of a stellar stream.

We first of all perform a cut on the proper motions. Figure 4.1 shows the proper motion-space of all RGBs from our current sample (∼103,000), where red points represent stars within 1 - 2 half-light radii of NGC 5466. Similar to the BHBs in Section 3.2.2, we observed a tight clumping in proper motion space for these *bona fide* cluster members. In comparison, most stars shown in this plot exhibit a diverse range of proper motions. We remove a large fraction of these halo stars by limiting our data to RGBs whose proper motions fall within a radius of 2 mas yr^{-1} of the mean proper motion of the cluster (red circle). This value equates to a range in tangential velocities at the distance of NGC 5466 of around 415 ± 152 km s^{-1}. Further, it is nearly 10 times larger than the average proper motion uncertainties of the NGC 5466 RGBs. Thus, it is unlikely to remove any stars associated with the cluster, but it greatly reduces the sample down to ∼6,600 stars.

Secondly, assuming that a typical globular cluster will have a single burst of star formation in its lifetime, the metallicity of any tidally stripped stars should be similar to stars in the main body. Indeed, the main body of NGC 5466 is known to have virtually no spread in [Fe/H]. Therefore, we require the metallicity for candidate stream members to be limited to a range of [Fe/H] = [-2.3, -1.7]. This range is centered on the Harris (1996, 2010 edition) metallicity estimate for NGC 5466 ([Fe/H] = -1.98), and includes the global metallicity uncertainty (0.3 dex; see Thomas et al. 2019) cited for the D+G catalogue.

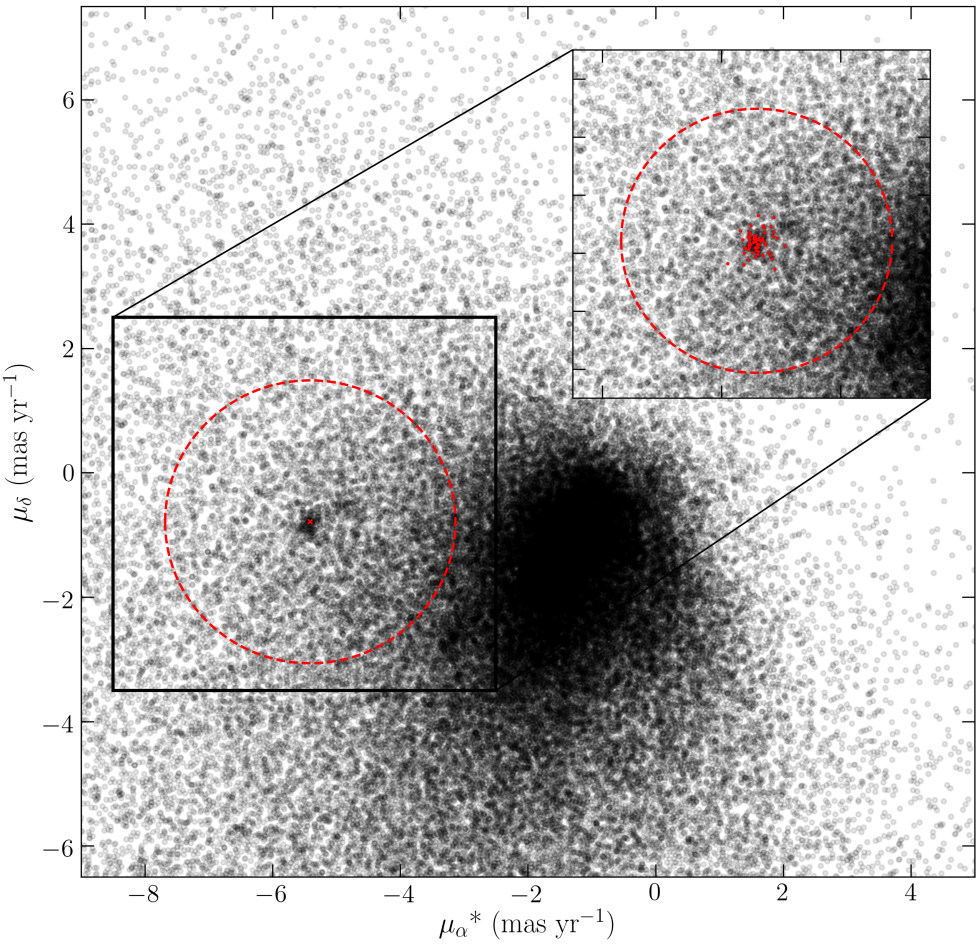

Figure 4.1: Proper motions of all available giants ($P_{giant} > 50\%$). The grouping of red RGBs highlighted in the zoom-in panel are those within 1 - $2r_h$ of the center of NGC 5466. The red dashed circle shows the 2 mas yr^{-1} boundary chosen to select stars with broadly similar proper motions to the globular cluster.

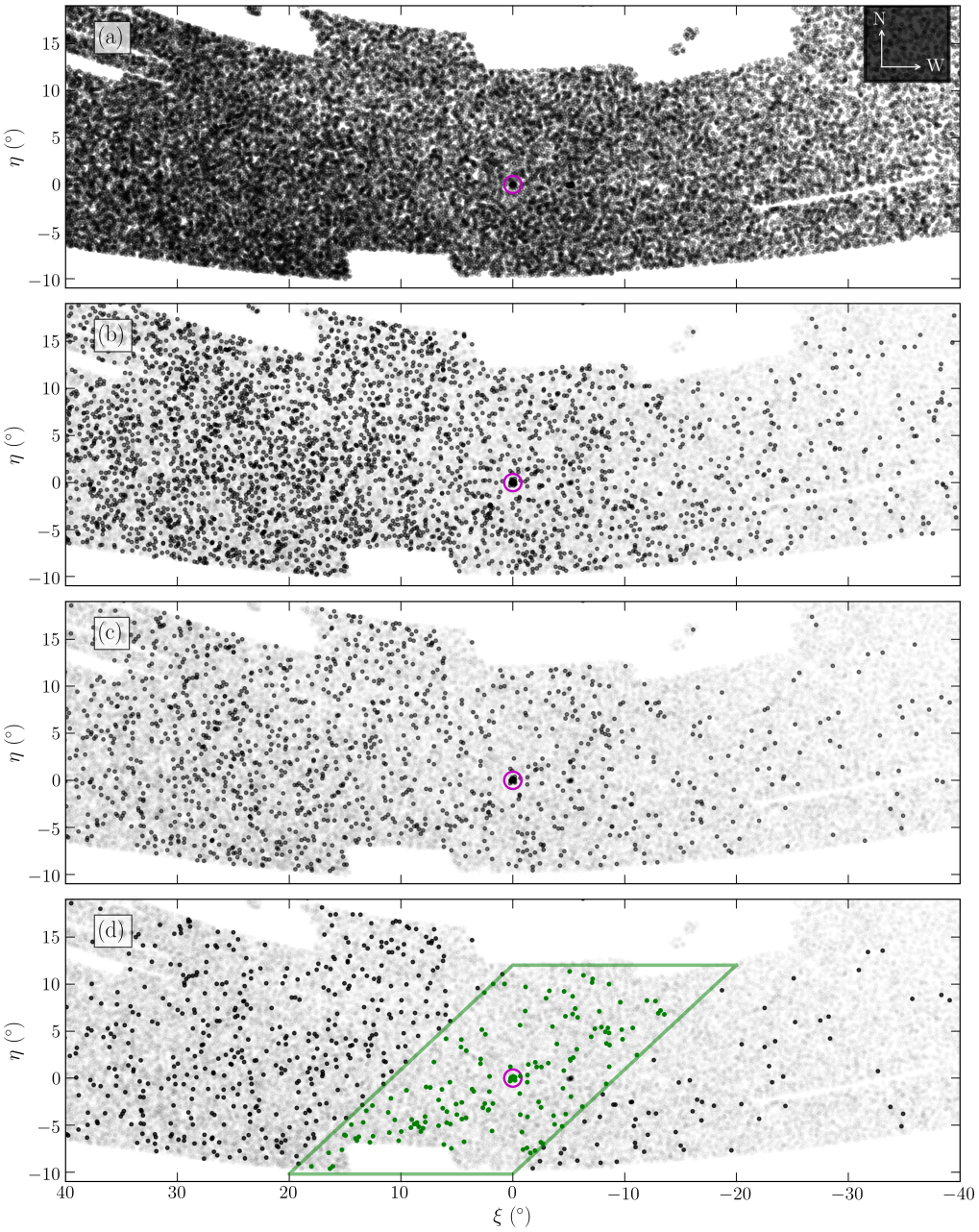

Figure 4.2: Projected distribution of stars used in this section centered on NGC 5466 (magenta circle). **(a):** Giants with $P_{giant} > 50\%$. **(b):** Black points are the sample after a proper motion cut seen in Figure 4.1, grey in remaining panels are the sample shown in (a). **(c):** Remaining points after a limitation between [Fe/H] = [-2.3, -1.7]. **(d):** The sample after a distance restriction of R_{helio} = [10, 22] kpc. Green points show the region of interest.

Finally, we restricted the allowable heliocentric distance range for the RGB stars. NGC 5466 is at a distance of 16 kpc. Distance uncertainties on individual measurements are typically 25% or better (Thomas et al. 2019), and we further broaden the range to allow for a possible distance gradient. We therefore require $R_{helio} = [10, 22]$ kpc.

Figure 4.2 shows the cumulative effect that these cuts have on our sample of RGBs. Each panel represents the tangent plane projection centered on NGC 5466, and the magenta circle highlights the position of the cluster. The top panel (a) shows our initial sample of RGB stars, and each subsequent panel shows the additive effect of (b) the proper motion cut (c) the metallicity cut (d) the distance cut. Also shown in the final panel is a simple polygon where we selected stars in the vicinity of the cluster for follow-up.

4.3 Automatic Identification of Stream Members

The descending panels of Figure 4.2 show tentative evidence of an extended structure emerging from the south-east to north-west of NGC 5466. If this apparent spatial overdensity is real, then there should be an associated kinematic signature in these stars. We selected the stars highlighted by the green box in panel (d) of Figure 4.2 for further investigation. The shape of this polygon encompasses the putative structure itself, without being overly restrictive. We developed an algorithm to examine the kinematics of these stars that is simple and reproducible, and which has been tested using both large and smaller selection boxes without any significant changes to results.

Our algorithm is based on a sigma-clipping routine which works as follows:

1. In $\mu_\alpha{}^*$ vs α, we fit a one-degree polynomial to all the data, where the weights are given by the uncertainties in the proper motion.

2. We then reject stars that are more than 3σ from the fitted line. We then generate a new polynomial fit to the remaining data.

3. We repeat the previous step, ensuring to initially include all of the data prior to deciding which stars to reject (i.e. including the stars that were rejected in the previous iteration).

4. We repeat this step until convergence, i.e. the polynomial fit and the number of stars retained no longer vary.

For the stars that survive the sigma-clipping in $\mu_\alpha{}^*$ vs α, we then reapply the algorithm to their μ_δ vs δ data. The final sample of stars are those that have survived both sets of the sigma-clipping.

Figure 4.3 shows the impact of applying this procedure to the dataset. The top and middle rows show the proper motions in each direction against α. The bottom row shows the spatial projection of the stars in the tangent plane. For clarity, both panels in the same row are the same, except the red points in the right panels represent the final sample of stars that remain after the sigma-clipping applied by the algorithm. We observe a clear sequence of stars in proper motion-space. Most notably, even though all of the analysis by the algorithm occurs in $\mu_\alpha{}^*$ vs α and $\mu_\delta{}^*$ vs α, the RGBs that remain form a very clear, coherent, and extended stream-like structure on the sky, as shown in the bottom right panel (bearing in mind a few evident outliers).

We conclude that there is clear and strong evidence for an extended stellar stream from NGC 5466, which can be traced over a large region of sky using RGBs and, to a lesser extent, BHBs. We refer to the BHBs and RGBs that define the stream − as seen in Figures 3.4 and 4.3 − as the "Gold Sample". In the following chapter, we quantify the detailed observational properties of this stream.

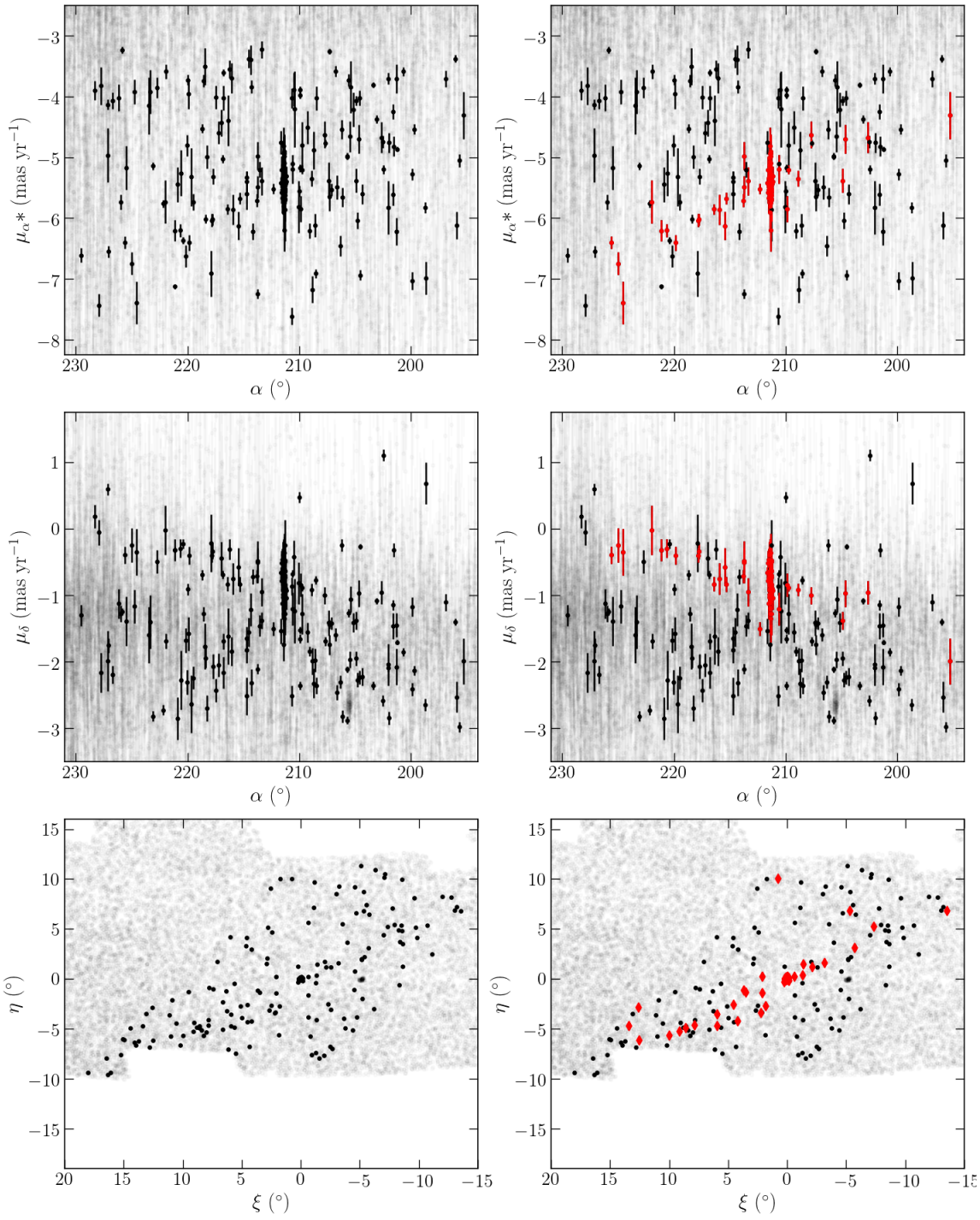

Figure 4.3: Proper motions (in each direction) of sample RGB stars as a function of R.A. (top and middle rows), and spatial distribution of the stars in the tangent plane (bottom panel). For clarity, both panels in the same row are the same, except the red points in the right panels represent the final sample of stars that remain after the sigma-clipping applied by the algorithm (i.e., the sample after both μ_α* vs α and μ_δ vs δ clippings). Grey points represent all RGBs, and black points are those within the green box in Figure 4.2.

Chapter 5

The Observational Properties of the NGC 5466 Stellar Stream

The previous chapter confirmed the existence of a very extended stellar stream around NGC 5466 for which we identified a clear kinematic structure traced by CFIS RGBs and BHBs. These stars are hereafter titled the "Gold Sample", or our highest confidence members of the NGC 5466 stellar stream. The positions and proper motions of these stars are given in Tables A.1 and A.2 in the Appendix.

Here, we evaluate the properties of this stream by analyzing trends in the Gold Sample. We first establish the stream's natural frame of reference, then quantify its variation in proper motions and distances as a function of stream longitude, or ϕ_1. We then use these relations to search for additional members, and to estimate the luminosity and width of the stream. We conclude that our final detection in this work extends approximately 31° on the sky.

5.1 Defining the Plane of the Stream

As a satellite orbits the Galaxy, its trajectory follows a path that is closely represented by the best fit great circle (Ibata et al. 2001b). For a relatively distant stream such as NGC 5466 that spans several tens of degrees, a great circle fit in the heliocentric frame is a good approximation to the Galactocentric equivalent, and is highly convenient as a frame in which to quantify the stream's properties. Positions on the celestial sphere are given in (ϕ_1, ϕ_2) which describes the longitude and latitude of the great circle respectively. For the frame that conveniently represents the NGC 5466 stellar stream, we define the origin as the R.A. of NGC 5466 (i.e., $\phi_{1,0} = 211.3637°$).

We used the Gold Sample stars[1] to fit a great circle plane to the NGC 5466 stream, such that the origin is located at the R.A. and declination of the globular cluster. The pole of the great circle is determined by least-squares minimization of ϕ_2, resulting in a pole at (α_P, δ_P) = (-16.86 ± 0.83°, 50.77 ± 0.46°).

To convert from equatorial to NGC 5466, we show the translation below in Equation 5.1. However, note that the x-axis must be inverted for the leading arm to correspond with increasing ϕ_1:

$$\begin{bmatrix} \cos(\phi_1)\cos(\phi_2) \\ \sin(\phi_1)\cos(\phi_2) \\ \sin(\phi_2) \end{bmatrix} = \begin{bmatrix} -0.7500318816 & -0.4571694316 & 0.4779626423 \\ -0.2663830593 & 0.8702492573 & 0.414374584 \\ 0.6053860275 & -0.1834729981 & 0.7744968797 \end{bmatrix} \times \begin{bmatrix} \cos(\alpha)\cos(\delta) \\ \sin(\alpha)\cos(\delta) \\ \sin(\delta) \end{bmatrix} \tag{5.1}$$

Figure 5.1 shows the distribution of Gold Sample members (BHBs and RGBs as diamonds and circles, respectively) and cluster giants in this new frame of reference. The top panel shows the heliocentric distances as a function of ϕ_1 and the middle and bottom panels show the positions of these stars in (ϕ_1, ϕ_2). The vectors in the middle panel represent the proper motions (scaled by 40%), corrected for the Solar reflex motion (as in Section 3.2.2), and the color scale in the bottom panel shows each star's heliocentric distance.

[1]The Gold Sample contains only those stars considered part of the stellar stream, not the main body (i.e., stars beyond the tidal radius of NGC 5466).

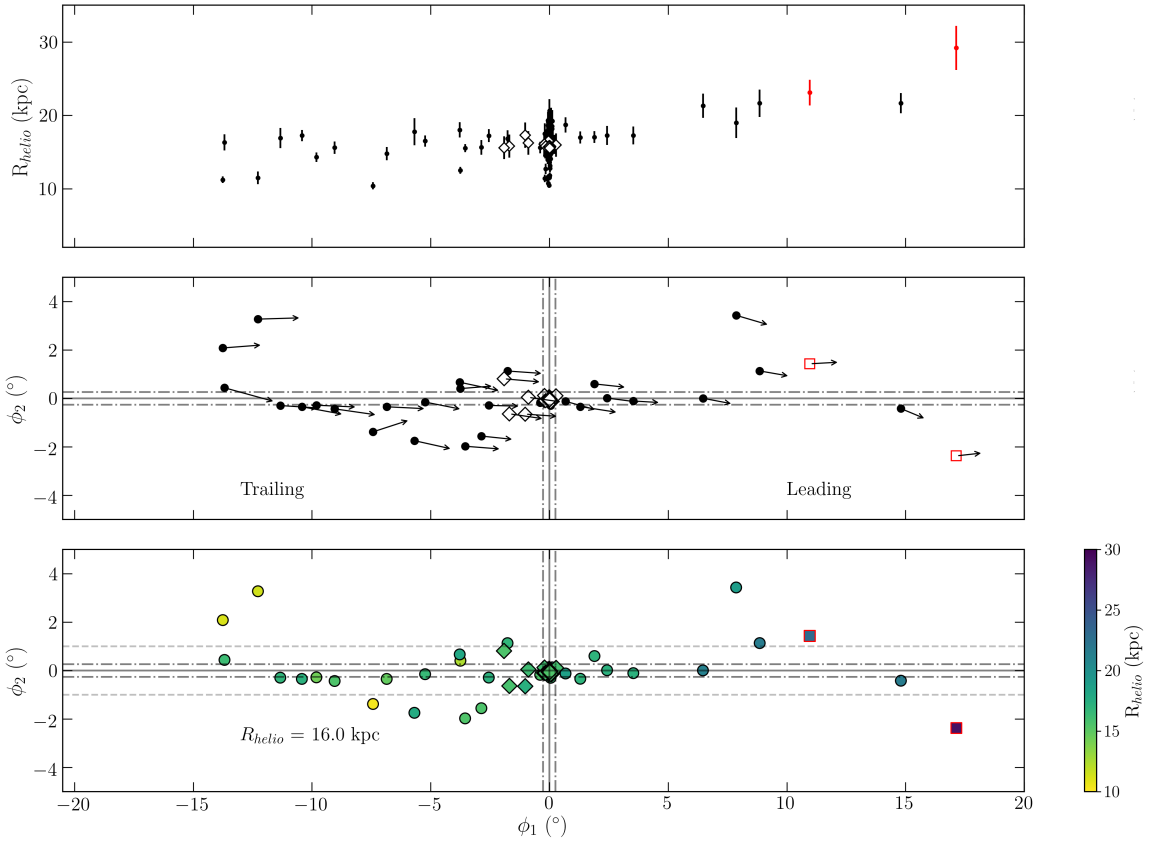

Figure 5.1: Gold Sample RGBs (circles) and BHBs (diamonds) in the rotated reference frame. The top panel shows the heliocentric distances of all stars as a function of ϕ_1. Dashed-dotted lines in the middle and bottom panels show $\pm r_t$ (tidal radius) on both axes. The vectors in the middle panel represent the Solar-corrected and rotated proper motions. The bottom panel's color gradient represents the heliocentric distances shown in the top, and dashed horizontal grey lines in this final panel are at $\phi_2 = \pm 1°$ for scale. Two additional member stars identified in Section 5.2.3 are plotted in red.

Parameter	Estimate	Comparison	Source
R_{helio} (kpc)	15.2 ± 1.6	16.0	1
μ_α* (mas yr^{-1})	-5.41 ± 0.14	-5.41 ± 0.01	2
μ_δ (mas yr^{-1})	-0.78 ± 0.13	-0.79 ± 0.01	2

Table 5.1: Cluster estimates determined by giants within r = [0.5, 2] half-light radii. The RGBs are those retained from the sigma-clipping routine and we additionally incorporate the BHBs identified by OPTICS. Comparison estimates are from (1) Harris (1996, 2010 edition) and (2) Baumgardt et al. (2019).

5.2 Stream Properties

5.2.1 Cluster Parameters

The complete sample of tracer stars associated with NGC 5466 consists of 197 giants (at present), 163 of which are RGBs and BHBs located within the tidal radius of the cluster. Prior to studying the stream in detail, we confirmed our measurements for the main body of the cluster to that of the literature.

Figure 5.2 shows the heliocentric distances and proper motions for all cluster giants. Within the tidal radius (leftwards of the blue vertical line), the mean and scatter of these quantities are very well-defined. However, we recognize that our estimates may be impacted by crowding effects. To quantify this, we firstly examined the number density profile for all NGC 5466 stars in the CFIS-PS1 dataset. Stars within the tidal radius of the cluster are binned in increments of $0.25r_h$, as shown in Figure 5.3. It is apparent that the number density falls off in the grey highlighted region, which corresponds to $0.5r_h$.

Although the proper motion panels in Figure 5.2 appear well-constrained, the heliocentric distances are derived from photometry. To avoid any possible bias crowding effects may impart on our estimates, we only used the giants between $0.5 - 2$ half-light radii (green points) to estimate the mean values of these quantities for NGC 5466. Table 5.1 shows our determined estimates for the globular cluster and comparison values to those found in the literature. We find good agreement with previous works.

5.2.2 Proper Motion and Distance as a Function of ϕ_1

With a more complete sample of member candidates, we can now explore parameters of the stream, along the longitude of the great circle. First, we used the present Gold

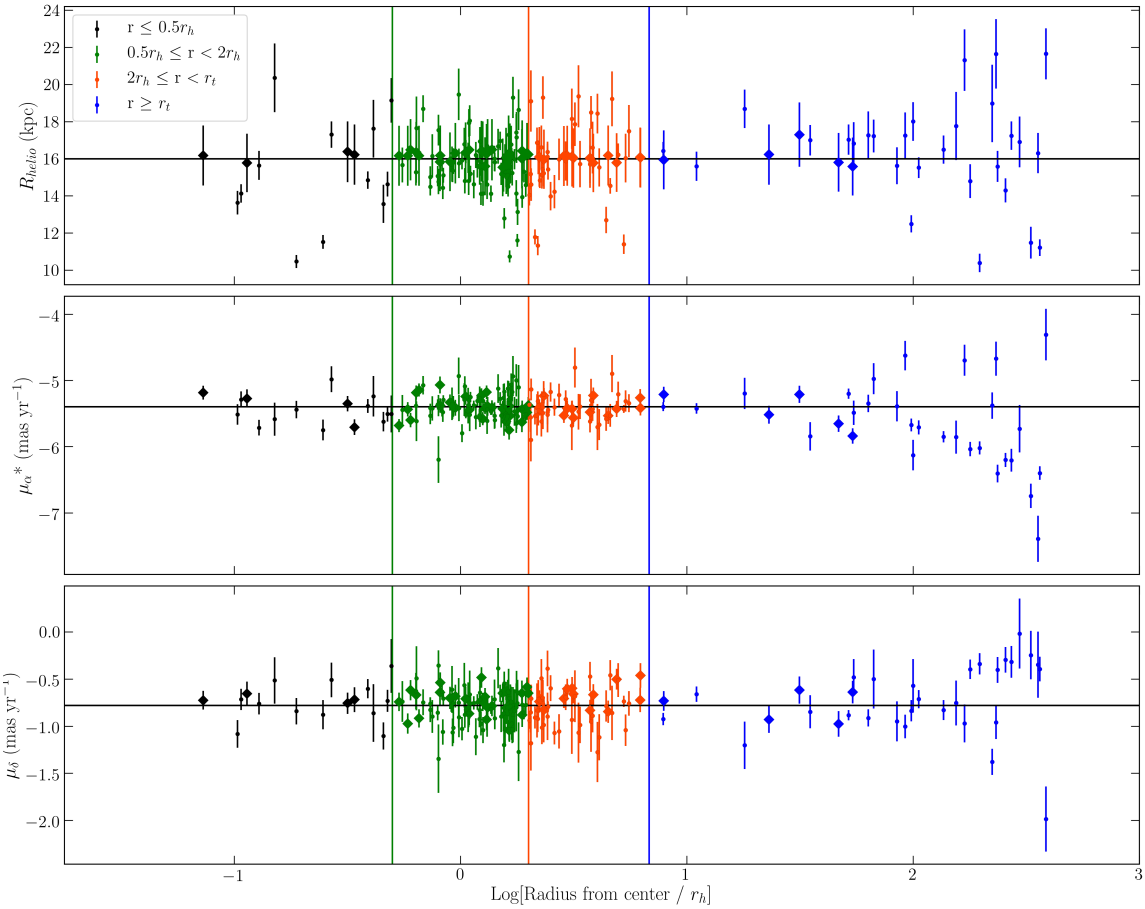

Figure 5.2: Parameters of the RGBs (circles) and BHBs (diamonds) as a function of half-light radius. Black horizontal lines show the comparison parameters seen in Table 5.1 from the literature. In units of half-light radii, black points lie within 0.5r$_h$, green from [0.5, 2]r$_h$, orange from [2r$_h$, r$_t$], and blue points fall beyond the tidal radius (i.e., the Gold Sample). This figure shows the spread for these observables are generally very well-defined within NGC 5466.

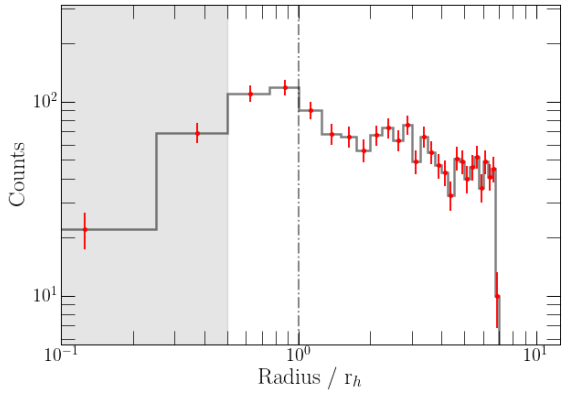

Figure 5.3: Number density profile of cluster stars from CFIS-PS1 in radial bins of $0.25r_h$. At $r = 0.5r_h$ (highlighted grey region), the number density of stars falls off, signaling detection biases caused by crowding. Red points show the errors of each radial bin assuming Poisson statistics.

Sample of 34 giants and describe their behavior with longitude via polynomial fits. To determine the best fit functions, we calculate the Akaike Information Criterion (AIC) for various degree polynomials. AIC is an estimator used to compare the relative goodness of fit for competing models where the favored model is that which minimizes the AIC score. Specifically, if k is the number of parameters in a model and $\mathcal{L}$ is the maximum likelihood of the model, then:

$$\mathrm{AIC} = 2k - 2\ln(\mathcal{L}) \tag{5.2}$$

where the relative likelihood of two models with AIC_1 and AIC_2 is defined as:

$$\text{Relative Likelihood} = \exp(\frac{AIC_1 - AIC_2}{2}) \tag{5.3}$$

AIC avoids overfitting the data, and penalizes models that are overly complex. We find that the proper motions in both directions are best described by a 1-degree polynomial, though distances along ϕ_1 are not well described by any low-order polynomial (due to the apparently different behavior of the distance as a function of $\phi_1$in the trailing and leading arms; see the top panel of Figure 5.1). Figure 5.4 shows the best fit polynomials to the proper motion data in each direction for the Gold Sample, where the dashed lines show the 3-σ uncertainty in the slope of the fits.

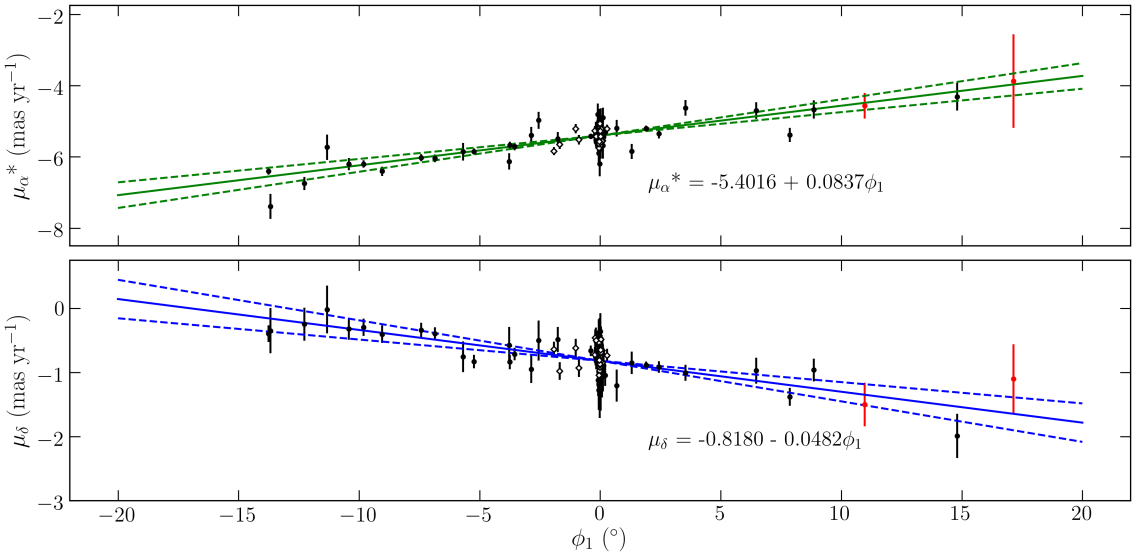

Figure 5.4: Proper motions as a function of ϕ_1 where the black points are RGBs and white-faced diamonds are BHBs. Red points show those identified by the search routine as likely members. Dashed lines show three times the standard error on the slopes.

5.2.3 Searching for Additional Stream Members

Using these established relationships between proper motions vs the stream's longitude from the previous section, we constructed a simple automated routine to search for additional stream members. This method looks for any stars in the dataset, including at very large separations on the sky, that are consistent with our estimated trends. We consider all stars with ϕ_1 = [-30°, 30°] classified as RGBs (probabilities > 50%), which have a consistent metallicity to that of the cluster ([Fe/H] = [-2.3, -1.7]).

The criteria for putative membership is determined primarily by the proper motions. For a given star, if the 1-σ range of its proper motion in consistent with the expected proper motion of the stream as given by the polynomial fits (to within three times the standard error of the fit, as shown by the dashed lines in Figure 5.4), then we retain it for consideration. We additionally require that that $|\phi_2| \leq 5°$ for each RGB. This is a generous cut, and only removes stars that are clearly far away from the plane of the stream. Finally, we look at the heliocentric distances of the remaining stars and compare them to the relationship of R_{helio} vs ϕ_1. We find two additional possible members using this method. These stars are appended to Table A.2 and we show them in Figures 5.1 and 5.4 in red.

Figure 5.5 shows all stream members, in equatorial coordinates (top panel) and the rotated frame (bottom panel). Not only does this stream appear to cover a substantial length of sky, but it is apparent that the stream is diffuse and low in density. The length we derived in this work for the NGC 5466 stellar stream as traced in CFIS is approximately 31°.

5.2.4 Width

We determined the average width of the stream by measuring the spread of ϕ_2 in for all stream members. Using the data from Tables A.3 and A.4, we fit a Gaussian to stars further than 1° from the cluster center. The distribution as a function of ϕ_2 is shown in the right panel of Figure 5.6, along with the Gaussian fit. For comparison, the equivalent histogram is shown in the left panel for stars within the tidal radius of the cluster. The dispersion perpendicular to the stream is [0.90 ± 0.11]°; this is equivalent to nearly 3.5 times the tidal radius of NGC 5466. Interestingly, this is smaller than the value determined by Grillmair & Johnson (2006), who estimated a width of 1.4° using the width of the matched filter map.

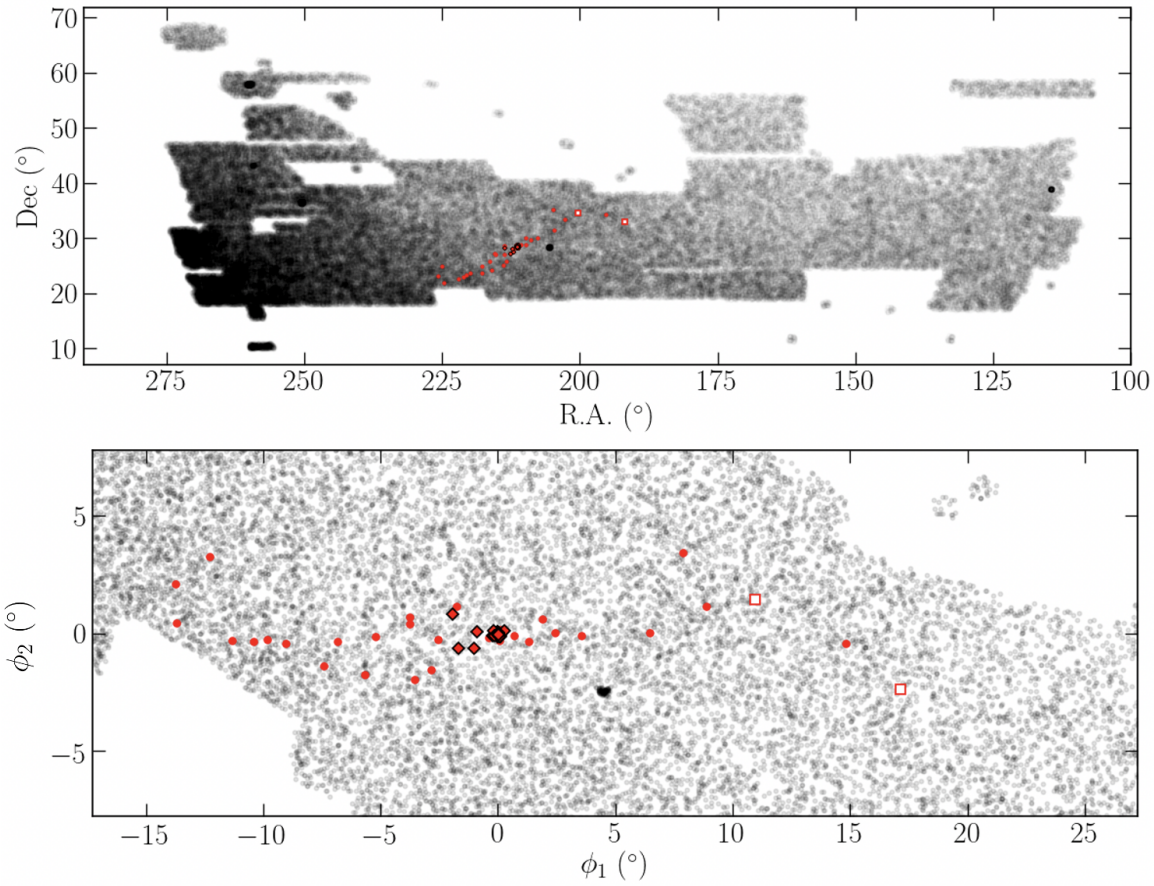

Figure 5.5: Gold Sample stream in equatorial (top) and in the rotated great circle plane (bottom) where RGBs and BHBs are as in Figure 5.1. We searched over all grey points in this representation (up to $\phi_1 = \pm 30°$) for additional members; these are therefore the RGBs limited by only metallicity. Red points are the original Gold Sample, and red/white squares show the appended members.

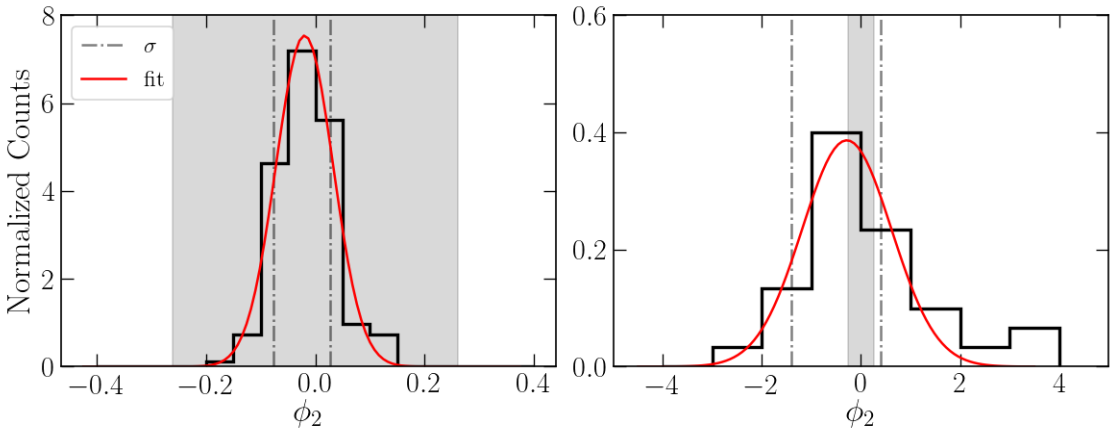

Figure 5.6: Normalized counts for the spread in ϕ_2. The left panel shows the distribution for globular cluster stars, or those within r_t (highlighted as the grey region in both plots). The distribution for Gold Sample members (at >1° radii from the center of NGC 5466) is shown in the right. Red lines in each figure are the Gaussian fit to the respective data, whose 1σ standard deviations are shown as dashed-dotted grey vertical lines. The width dispersion of the giants in the globular cluster vs in the stream are $[0.053 \pm 0.002]^\circ$ and $[0.90 \pm 0.11]^\circ$, respectively.

5.2.5 Luminosity and Mass

Our Gold Sample consists of 36 giants in total, and the total number of RGBs and BHBs in NGC 5466 is 163. We can therefore determine a lower limit for the luminosity and mass of the stream by comparing the ratio of stars within/outside the tidal radius of NGC 5466. However, the innermost regions of the cluster suffer from crowding effects. This will directly impact the number of giants we are able to detect, and must be corrected for.

To accurately estimate the number of stars in the cluster, we parameterize its density as a King profile (King 1962):

$$f = k[\frac{1}{(1+x)^{1/2}} - \frac{1}{(1+x_t)^{1/2}}]^2 \tag{5.4}$$

where $\mathrm{x} = (\mathrm{r}/\mathrm{r}_c)^2$ and $\mathrm{x}_t = (\mathrm{r}_t/\mathrm{r}_c)^2$. k is a normalisation factor, such that the integral of $f(x)$ equals the stellar luminosity of the cluster. Considering that the total luminosity is directly linked to the number of stars of a cluster, this profile also describes the number of stars contributing to each radial bin of luminosity. Integration from various radii therefore determines the percentage of stars contributing to each bin.

We integrated from [$0.5r_h$, r_t] (where the inner bound is to avoid the crowded regions of the cluster) and found that 45.5% of the luminosity is contained in this radial range. The number of giants (both RGBs and BHBs) we detect within these radii are 148; therefore the total number of giants that we should detect if crowding is negligible is approximately 325. Thus, the ratio of stars in the stream to those in the main body is 0.11.

The absolute visual magnitude of NGC 5466 is -6.98 mag (Harris 1996, 2010 edition), which equates to a total luminosity of 4.9×10^4 $\mathrm{L}_\odot$. This implies that the luminosity of the detected part of the stream is 5.3×10^3 $\mathrm{L}_\odot$. We find, given the stellar mass estimate of 5×10^4 $\mathrm{M}_\odot$ from Pryor et al. (1991), the stream is approximately 5.5×10^3 $\mathrm{M}_\odot$. This is consistent with a stellar mass-to-light ratio of $\sim$1 as seen in most old globular clusters.

This method has a few caveats, and certainly provides a lower limit estimate. For example, we assume that the number of giants in the stream is in fact the total number. While we have attempted to search for more member giants, it is clear that the data in the leading arm of NGC 5466 appears significantly more sparse than the number of detections in the closer, trailing arm. We argue in the next section that a recent pass through the Galactic disk may have caused this interesting discrepancy.

We recognize it could equally be caused by completeness effects, but believe this to be unlikely. The most distant RGB star we find in the stream has a *Gaia* *G*-band magnitude of 19.6, nearly 1.5 magnitudes brighter than the *Gaia* magnitude limit. Therefore, we conclude that completeness effects are likely not the cause of this variation. A final caveat of this estimate is the truncation of the trailing arm, which may be the caused by the southern CFIS footprint boundary ($\delta < 20°$; see top panel of Figure 5.5). This would suggest the stream may in fact be longer than we have traced it in this work, and would directly influence the ratio of stars in the stream to those of the cluster.

Chapter 6

Modelling the Dynamics of NGC 5466

In this chapter, we implement a dynamical model using the "particle-spraying" technique to explore the disruption of NGC 5466. This method allows us to qualitatively compare observed orbital properties of the stream stars directly to dynamical experiments. The resulting model shows very good agreement with the observed properties, with some interesting small differences. We suggest these could be due to variations in the actual and assumed dark matter halo shape and mass at these distances.

6.1 Particle-Spray Dynamical Modelling

There exist multiple approaches to dynamically model the disruption of satellites around the Galaxy. When comparing observed stellar streams to simulations, full N-body simulations serve as the most comprehensive option. This method treats any mass distribution as a large collection of point particles. These models are extremely useful, as they follow each particle's detailed interaction with time. For example, these simulations can be used to explore the response of the mass profile on the satellite-host interaction (when the potential cannot be suitably approximated analytically), or understanding the detailed structure of a satellite and the morphology of its tidal tails. However, these simulations can be computationally expensive and are primarily warranted once there is already a "sufficiently good" understanding of the global dynamical properties of the interaction.

Orbit-fitting methods lie on the less intricate end of the spectrum. These models largely ignore disruption processes by integrating the orbit of the satellite as a point mass. Under the assumption that a stream will largely follow the path of the progen-

itor's orbit, this method serves as a good first estimate for tracing the path of any stream, but such a process cannot by definition identify a stream's orbital properties.

Recognizing that our current work is focused on observational properties of the NGC 5466 stellar stream, and preliminary exploration of orbits, we examine point mass orbits in conjunction with an intermediate dynamical modelling technique known as "particle-spraying". This method allows us to examine qualitatively the phase-space distribution of stripped mass in our system as the progenitor is disrupted over time, and is less computationally demanding than full N-body modelling. Our general goal is to determine if the revised observational properties of NGC 5466 that we have measured are more consistent with results from dynamical modelling than previous efforts. In this respect, it is a final "sanity check" on our observational results. The methodology of particle-spraying is described in detail in Fardal et al. (2015), though we summarize the main features below.

As a satellite orbits a host galaxy, the gravitational forces between the host potential and the particles of the satellite act to strip mass from the smaller body. A particle from the satellite is considered tidally stripped when it is removed past the Jacobi (or tidal) radius of the progenitor. These particles then orbit the Galaxy instead of the satellite. In a simplistic two-body system with spherical potentials, the mass is lost from the L_1 and L_2 Lagrange points surrounding the progenitor. These points are defined as the location where the centrifugal force equals the gravitational forces between the satellite and the host. L_1 is the location where the host potential is strongest, and particles at this position are removed into lower potential energy orbits. These particles then form the leading arm of a stream. Consequently, L_2 is the position where particles are removed into higher potential energy orbits, therefore forming the trailing arm.

The particle-spray method uses the Lagrange points of the host-satellite system to remove particles over time. At specified timesteps, massless particles are ejected from L_1 and L_2 and their orbits are determined given the progenitor's current position and velocity. Mass loss is not tracked in this method, yielding quick approximations for the dynamical behavior of tidally disrupted stars. The ejection rates of particles are not based on numerical computations since the main purpose of the technique is to map the stream's evolution in phase-space.

To compare our Gold Sample members to dynamical models, we used the Fardal et al. (2015) distribution function of particles as described above (i.e., particle-spraying), in the GALA framework (Price-Whelan 2017). This PYTHON package is

used to model Galactic dynamics and calculate stellar orbits in a given potential. We generated a toy model of the stream with GALA to explore its evolution in phase-space. We additionally integrated a massless orbit for NGC 5466 for general comparison.

6.2 Modelling the Cluster's Disruption

6.2.1 Input Parameters

Firstly, we orient our coordinate system to the Galactocentric plane as implemented in ASTROPY (Astropy Collaboration et al. 2013). In this frame of reference, (X, Y, Z)$_{gal}$ are defined in a right-handed coordinate system with the origin located at the Galactic center. This system defines the position of the Sun at -X$_{gal}$. The Y$_{gal}$ and Z$_{gal}$ coordinates are positive in the direction of Galactic rotation and towards the North Galactic Pole, respectively. We used the most recent estimates of the distance to the Galactic center determined by Gravity Collaboration et al. (2019), 8.122 kpc, and 25 pc as the height of the Sun from the midplane (Jurić et al. 2008). To convert from LSR to the Galactocentric frame, we correct for the motion of the Sun using Schönrich et al. (2010) LSR velocities [U,V,W]$_{\odot}$ = [11.1, 12.24, 7.25] km s^{-1} (as in Section 3.2.2).

To model the Milky way, we implement a three-component potential consisting of a Miyamoto & Nagai (1975) disk, a Hernquist (1990) bulge, and NFW dark matter halo (Navarro et al. 1996) described by the following equations:

$$\Phi_{bulge}(R) = \frac{-GM_b}{R+a} \tag{6.1}$$

$$\Phi_{disk}(R_{cyl}, z) = \frac{-GM_d}{\sqrt{R_{cyl}^2 + (b + \sqrt{z^2 + c^2})^2}} \tag{6.2}$$

$$\Phi_{halo}(R) = \frac{-4\pi G \rho_s r_s^3}{R} \ln\left(1 + \frac{R}{r_s}\right) \tag{6.3}$$

where R is the Galactocentric radius, R$_{cyl}$ is the cylindrical radius, and z is the vertical height above the disk. Our chosen values for masses, scale radii, and other parameters are summarized in Table 6.1. For the disk, the mass (M$_d$), scale height (b), and scale length (c) are typical values also used in the MWPotential2014 from Bovy (2015).

For the halo, we adopted the most recent estimates for the Milky Way virial mass

Component	Parameter	Value
Bulge	M_b	5 x $10^9 M_\odot$
	a	1 kpc
Disk	M_d	5.56 x $10^{10} M_\odot$
	b	3.5 kpc
	c	280 pc
Halo	M_{vir}	8.2 x $10^{11} M_\odot$
	R_{vir}	207 kpc
	c_h	12
	r_s	17.25 kpc

Table 6.1: Milky Way parameters used in Equations 6.1, 6.2, and 6.3.

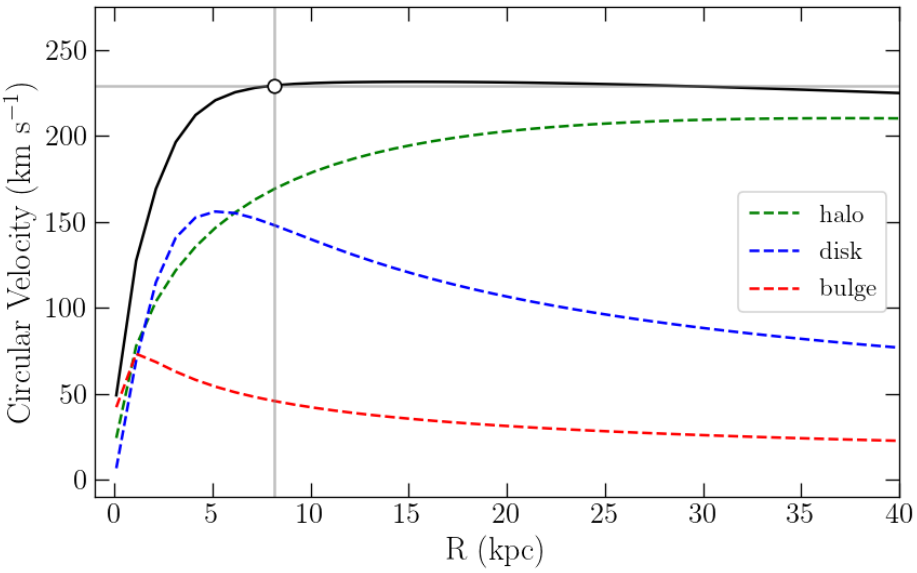

Figure 6.1: Velocity curve for GALA potentials. The cross-hairs are lain on $v_{circ}(R_\odot)$ = 229 km s^{-1}.

($\sim M_{200}$) and radius ($\sim R_{200}$) from Cautun et al. (2020). Assuming a dark matter concentration of 12 (a typical value observed in simulated Milky Way analogues; see Boylan-Kolchin et al. 2010) and using the relation $R_{vir} = c_h R_s$, we used a scale height for the dark matter halo of 17.25 kpc.

The bulge parameters are similar to those implemented in Bovy (2015); however, we require that the circular velocity at the position of the Sun equal $v_{circ}(R_\odot) = 229$ km s^{-1} (Eilers et al. 2019), as this is the most recent estimate for the circular velocity and is the value we used when correcting the proper motions for Solar reflex motion (see Sections 3.2.2 and 5.1). We used a factor of two smaller Hernquist (1990) mass (also implemented in Caldwell et al. 2020) which we found best reproduces this velocity. The Galactic rotation curve is shown in Figure 6.1.

We also accounted for the internal gravity of the satellite in our particle spraying model. This is represented as a spherical Plummer (1911) profile shown in Equation 6.4 below.

$$\Phi_p(r) = \frac{-GM_{sat}}{\sqrt{r^2 + d^2}} \tag{6.4}$$

We used the present-day mass of NGC 5466 (5×10^4 $M_\odot$ estimated by Pryor et al. 1991) and a scale height (d) of 6.7 pc derived from the core radius of the cluster (Harris 1996, 2010 version).

6.2.2 Results

To examine the orbit of NGC 5466 through the Galaxy, we integrated a point mass orbit 100 Myrs forwards and backwards. We used the potential described in the previous section and the present-day parameters of NGC 5466 (see Table 3.1). This yields an orbit with a pericenter at 6.42 kpc and an apocenter of 42.99 kpc, consistent with the values obtained by Baumgardt et al. (2019). Figure 6.2 shows the orbit integrations where forward and backward timesteps are represented as red and blue lines, respectively.

The bottom left panel in Figure 6.2 shows both the point-mass orbit and the GALA particles in Galactocentric coordinates. For the latter, we used the distribution function in Fardal et al. (2015) and ran the model for 1 Myr. We released 1 particle at each Lagrange point per timestep for a total of 1000 timesteps. As the satellite is integrated forward in its orbit, star particles are released and given orbital properties similar to those of the current progenitor and integrated forward in time.

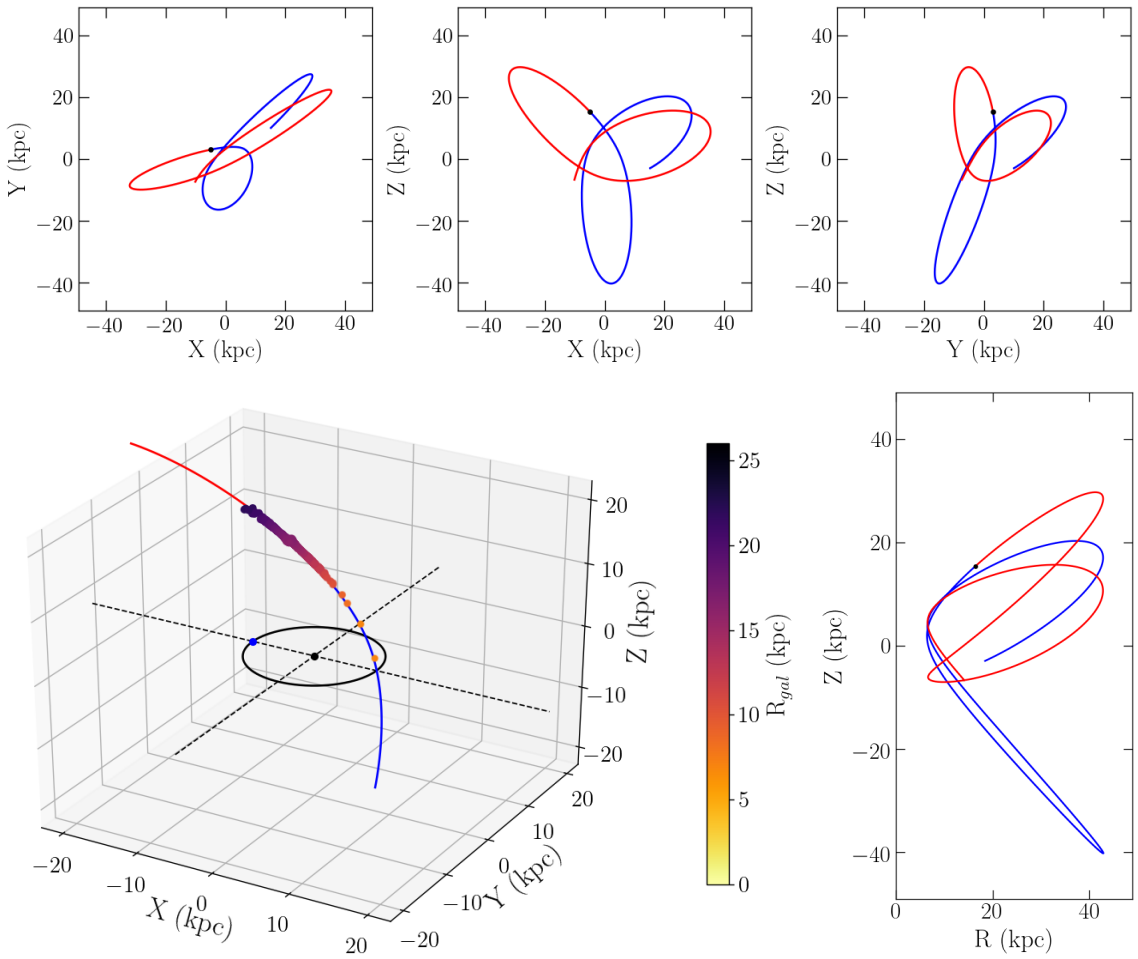

Figure 6.2: Orbit integrations of NGC 5466 in the Galactic potential described in Section 6.2.1. Blue and red lines represent the integration of a point mass over 100 Myrs backwards and forwards in time, respectively. GALA particles accompany the orbit shown in the 3-D plot. Their scaled colors are based on the galactocentric radii (R_{gal}). The position of the Sun is (X, Y, Z) = (-8.122, 0, 0.025) kpc in this frame and shown as the blue point in the 3-D plot.

The sprayed particles closely follow the point mass orbit as shown in the 3-D figure. The trajectory suggests the cluster crossed the disk within the past 100 Myrs, a result also noted in Odenkirchen & Grebel (2004). The authors claimed NGC 5466 had likely experienced significant mass loss from disk-shocking; this is consistent with the updated orbit we find with *Gaia* proper motions and the path of the detected tidal tails. However, to adequately explore the extent of mass loss caused by crossing the disk would require a more detailed suite of simulations.

We then converted the GALA particles positions to the ICRS frame and great circle plane for comparison to the observed kinematics. Figure 6.3 shows the proper motions and heliocentric distances as functions of the ϕ_1 stream longitude for the GALA star particles (black points) and the observed Gold Sample (grey error bars). Particularly in the proper motion panels, the model appears in excellent agreement with our data. We recall that the majority of stream members identified thus far were identified via the sigma-clipping routine in Section 4.3. The structure observed in the (relative) phase-space resulted in a coherent stream apparent in the on-sky positions. The fact that the proper motion behavior of these stars can then be reproduced with minimal difficulty using a simple dynamical model gives us high confidence in our observational methodology.

The bottom two panels of Figure 6.3 show the variation of heliocentric distances with ϕ_1. Here, we also note that our Gold Sample yields generally good agreement with the GALA model overall. However, the simple model appears to systematically underestimate the distances to the leading arm while giving a good match to the trailing arm (although there are not many points at large distance in the leading arm, and they all have quite large uncertainties). Such difficulties in matching both arms simultaneously are quite common in this field, most famously for the (much larger) stream from the Sagittarius dwarf galaxy (e.g., Helmi 2004; Law et al. 2005; Law & Majewski 2010). It is quite possible that this divergence may be a result of the spherical dark matter halo shape we implemented, although more investigation is necessary. In the future, it would be interesting to explore other halo shapes fit to our stream members, preferably with detailed N-body simulations to explore the stream's morphology. Presently, these experiments are beyond the scope of this work.

We also note that these panels highlight the fact that there are three Gold Sample members in the trailing arm that appear to be considerably closer than either other observed members of the model suggest. We highlight these RGBs with red circles in all panels and suggest that these stars may be contaminants based on their distance

discrepancies, though they appear consistent in all their other properties. Overall, we conclude that the observed dynamics of the stream are reasonably well represented by simple point mass and particle-spraying models, and that further modelling could prove interesting for better understanding the dynamics of the leading arm.

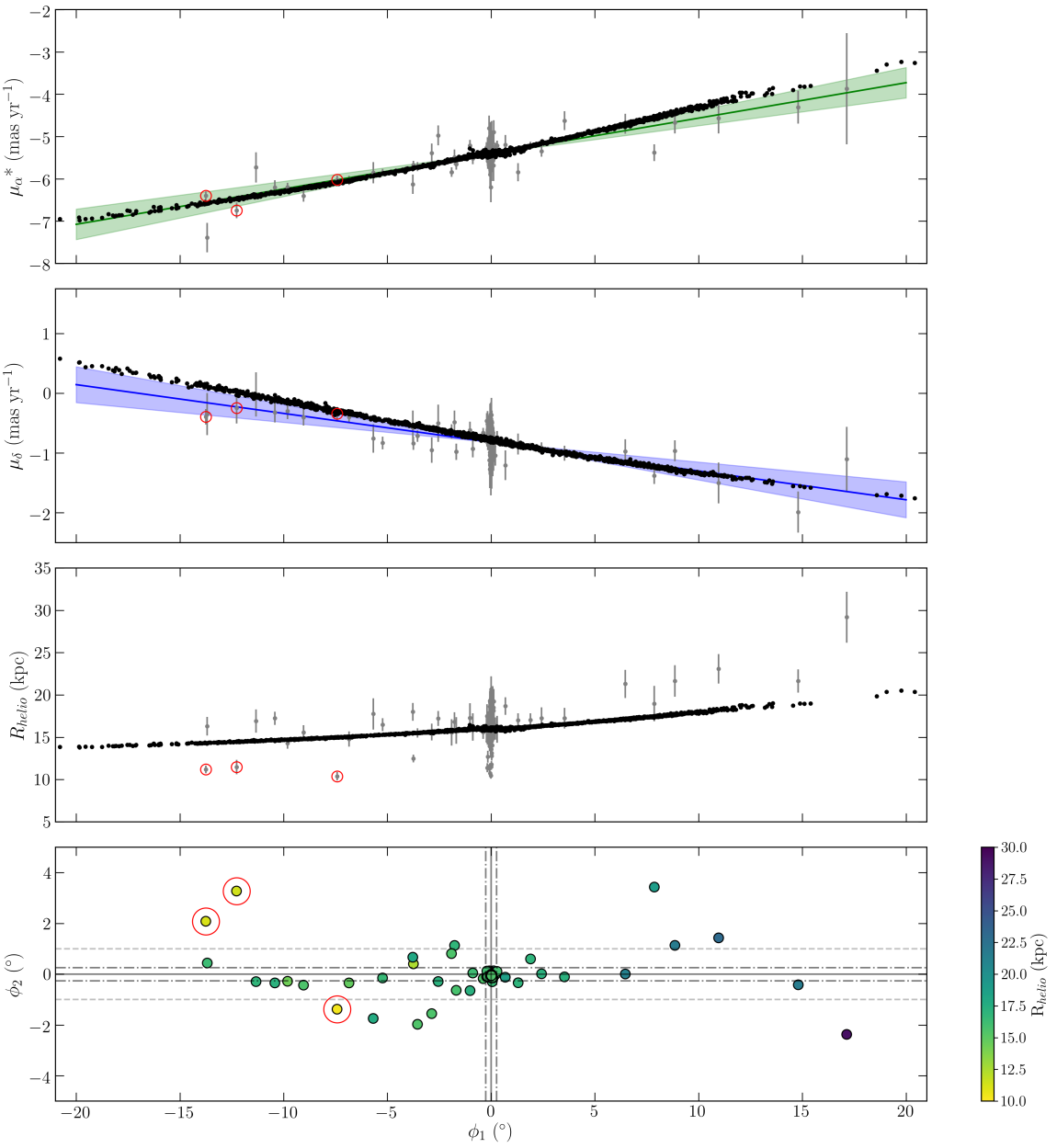

Figure 6.3: Comparison of the Gold Sample and cluster member orbital properties (grey error bars) to GALA particles (black points). The first two panels are the proper motions against ϕ_1 where the highlighted ranges show the upper and lower bounds of the polynomial fit seen in Figure 5.4. The model appears to very closely resemble the spread of observed values in our stream members. Bottom two panels show two representations of the heliocentric distances against ϕ_1. The red circles in every panel highlight three Gold Sample members that may be contaminants based on their relatively close distances.

Chapter 7

Discussion and Conclusions

7.1 Summary

The initial objective of this work was to explore substructure in the outer stellar halo of the Milky Way using multiple tracer populations identified with CFIS. The u-band data from this survey is instrumental for identifying suitable tracers given its sensitivity to metal lines in the blue region of the spectrum. CFIS therefore fills a useful niche for Galactic astronomy and is sufficiently deep to be combined effectively with other optical bands from SDSS and PS1, providing a more complete view across the spectral energy distribution of stars.

We first examined the spatial distribution of the CFIS BHBs identified in Thomas et al. (2018). By applying the OPTICS clustering algorithm to this sample, we identified prominent substructures associated with six known Milky Way satellites, and noticed possible extended structures in their vicinity. To confirm the association of these stars with the satellites, we cross-matched *Gaia* proper motions to each BHB.

Examination of the proper motion of the BHBs allowed us to identify a group of co-moving stars near the Galactic globular cluster NGC 5466. Tidal tails from this object had been hypothesized in previous studies (Pryor et al. 1991; Lehmann & Scholz 1997; Odenkirchen & Grebel 2004), and claimed to be observed in 2006. Belokurov et al. (2006a) identified tails extending 4° on the sky, and in that same year, Grillmair & Johnson claimed a much more extended stream spanning 45°. Dynamical models by Fellhauer et al. (2007) and Lux et al. (2012) attempted to reproduce the putative tails, though they each experienced difficulty in replicating the farthest extent of the leading arm. Further observations have not been made since the original detections.

Over the past decade, this stream has been largely ignored, despite its alleged length and distant progenitor for which NGC 5466 may yield intriguing dynamical science.

Given the intriguing literature surrounding this cluster and its tidal tails, and given that the co-moving BHBs we identified are consistent with a picture in which NGC 5466 is tidally stripped, we used additional tracers to determine if we could confirm (or refute) the existence of a stellar stream surrounding this globular cluster. We mined the RGBs from the D+G catalogue (Thomas et al. 2019) which yields a much higher density of tracer stars than the BHBs. This catalogue contains proper motions, positions, and metallicities for ∼314,000 giants (probabilities $> 50\%$, after star/galaxy classification) in the CFIS footprint.

Under the assumption that stars associated with NGC 5466 will have broadly similar proper motions, distances and metallicities, we identified a sample of giants in the extended vicinity of NGC 5466. A simple analysis of their proper motions allowed us to extract a structure that was both spatially and kinematically coherent, and which formed an extended stellar stream with NGC 5466 at its origin.

Having identified its members, we then determined the stream's natural frame of reference and quantified its overall structure, dynamics, and stellar mass. We compared the observed behavior in proper motions and distances to simple dynamical models involving both a point mass and a GALA particle-spray model. We found that even these simple models are able to reproduce the global behavior of the stream's proper motion, and provide a good match to the observed distance gradient. Our work is the first to identify member stars of NGC 5466 both spatially and dynamically, and we identify interesting systematic difference between observations and the models in the leading arm of the stream. We anticipate these results will motivate future modeling and observing campaigns (e.g., radial velocities), which could provide some interesting insights into the global shape of the Milky Way halo at these large distances.

7.2 Comparison to Previous Work

Many studies in the past few years have identified or re-identified Milky way substructures by mining the 1.3 billion sources in *Gaia* DR2. For example, Malhan et al. (2018) and Ibata et al. (2019) identified 13 new streams in total using the STREAMFINDER algorithm (Malhan & Ibata 2018) applied to *Gaia* 5-D kinematics. The distances of these new discoveries range from $R_{helio} = [5, 25]$ kpc. Though this

method was demonstrated to successfully locate known streams such as GD-1, Jhleum, Orphan, and Sagittarius, the NGC 5466 stream was not kinematically detected by these authors.

Two other studies searched for tidal streams using the RR Lyrae stellar population. Mateu et al. (2018) implemented the GC3 stream-finding method, which searches along great circle paths for overdensities and extended tails. This method resulted in fourteen new candidate streams and a handful of known structures; however, the authors state they do not identify any pole counts for NGC 5466. Additionally, Kundu et al. (2019) searched for extra tidal structures surrounding known globular clusters using RR Lyrae; however they similarly do not identify any tracing the NGC 5466 stellar stream.

Further studies probing the *Gaia* survey for stream-like structures (Helmi et al. 2017; Necib et al. 2019; Borsato et al. 2020) have also not traced NGC 5466 thus far. Considering the surplus of recently discovered stellar streams, it is somewhat interesting that NGC 5466 has not been uncovered. However, we attribute this largely to the fact that the stream is very distant (and hence, *Gaia* parallaxes are of limited use). Additionally, this stream is extremely diffuse: we detect approximately 36 giants over 31° of sky. We attribute our successful detections to our ability to robustly identify tracer populations with CFIS, which have distance estimates that are currently unparalleled at large Galactocentric radius, in addition to the exquisite proper motions provided by *Gaia* DR2.

Figure 7.1 directly compares our results to the original Grillmair & Johnson (2006) matched filter detection map. The authors argued that the dark diagonal strip from the bottom left to the top right corners are due to a physical overdensity of stars as a result of the NGC 5466 stream. We compare our great circle plane as the red line, which was fit to our observations; the magenta points also show the sprayed particles from our dynamical model. Close to the cluster, the path of the stream as given by Grillmair & Johnson (2006) is broadly in agreement with our results. However, at R.A. $\lesssim 200°$, the path of the great circle and model deviates from the claimed matched filter path. Indeed, as comparison to Figure 5.5 makes clear, we are unable to detect many stream members at R.A. $\lesssim 200°$. Given our analysis is based on deeper photometry (CFIS and PS1, compared to SDSS), we consider it unlikely that they feature in the matched filter at these coordinates is a real signal.

We also compare our findings to the results of the previous simulations which relied on the path of the stream as given by the matched filter. Fellhauer et al. (2007)

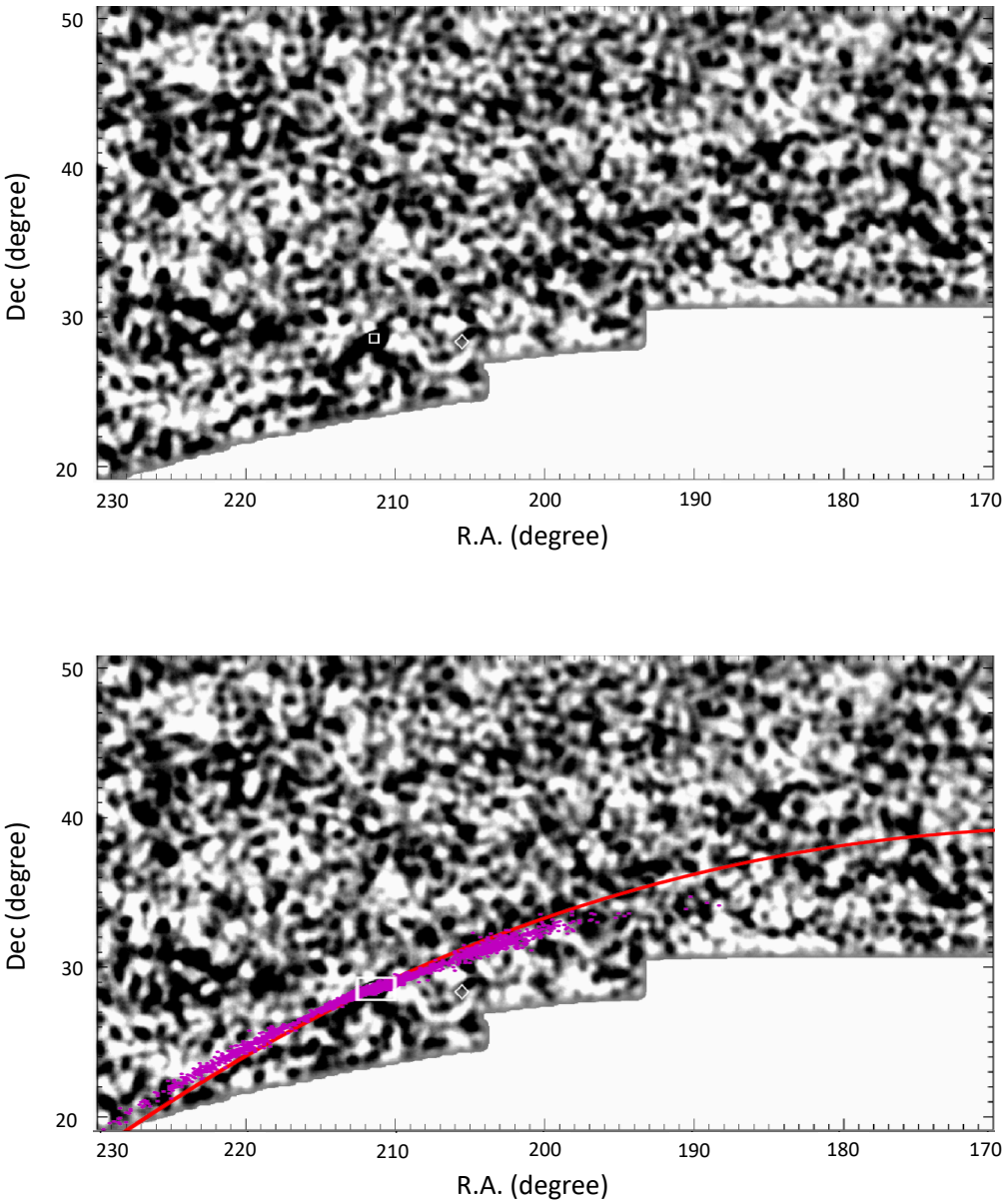

Figure 7.1: A direct comparison between the 45° detection from Grillmair & Johnson (2006). The top panel is the matched filter map showing the extended tails from (α, δ) = (230°, 20°) to (180°, 42°). The white square represents the globular cluster. In the bottom panel, we show the great circle fit to the Gold Sample members (red line) and the particle-spray model (magenta points). Both diverge at approximately R.A. = 200° compared to the original detection.

used SUPERBOX particle-mesh simulations to try to reproduce the morphology of the stream and the kinematics of the present-day globular cluster. By fitting the width and surface density of the simulation to that of the matched filter, they predicted tails up to 100°. The authors proposed that the recent passage through the disk by the globular cluster caused tidal shocks in the system and acted as the main trigger of mass loss. Their model suggested that the most recent passage through the disk occurred ∼100 Myrs ago − consistent with discussion in Odenkirchen & Grebel (2004) and this work.

Critically, Fellhauer et al. (2007) found that it was not possible to reproduce the stream with the current proper motion estimate for the globular cluster. At the time, the proper motions used were derived from HIPPARCOS, which yielded ($\mu_\alpha*$, μ_δ) = (-4.65 ± 0.82, 0.8 ± 0.82) mas yr^{-1}. The authors opted for a lower value of μ_δ = 0.4 mas yr^{-1}, within 1-σ of the measurement. Compared to the more recent *Gaia*-based estimate derived by Baumgardt et al. (2019), μ_δ = -0.79 ± 0.01, their correction is more accurate. Regardless, these authors predicted a trend in heliocentric distance that is generally consistent with our new findings (top panel of Figure 7.2).

Lux et al. (2012) used the Grillmair & Johnson (2006) stream-path and an orbit-fitting method to attempt to constrain the Galactic potential. Interestingly, they reproduced the path of the stream up to R.A. = 192° using oblate and triaxial halo shapes and claimed that spherical and prolate dark matter halos could be rejected at high confidence. We note that it is at this approximate position where we no longer detect any stream members, and reiterate that the path of our great circle plane begins to deviate from the path proposed by Grillmair & Johnson (2006).

Despite our agreement with Lux et al. (2012) with respect to the path of the stream on the sky, the gradient in heliocentric distances predicted by Lux et al. (2012) demonstrates the opposite trend compared to Fellhauer et al. (2007) and to our new observations. The bottom panel of Figure 7.2 shows the distance gradients in the stream for the suite of simulations run by Lux et al. (2012), whereas the red error bars show our new observed distance gradient. It is worth emphasising that, at the time these models were conducted, there was no direct information on the distance gradient of the stream. These results can now be efficiently compared to our Gold Sample observational data.

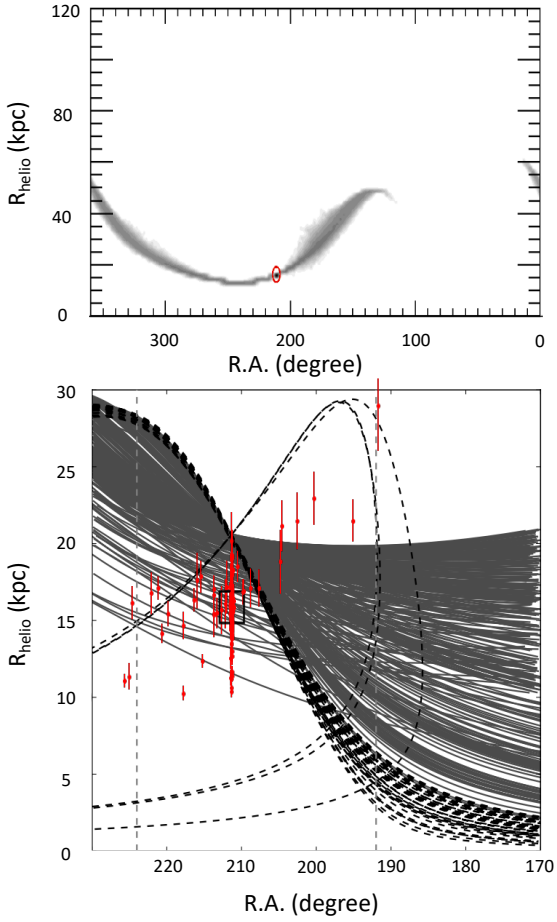

Figure 7.2: Direct comparison of our heliocentric distance trends with R.A. to the results from Fellhauer et al. (2007) (top) and Lux et al. (2012) (bottom). Red error bars represent our highest confidence stream members. Dashed vertical lines show the R.A. ranges where the path of the matched filter was reproduced successfully in Lux et al. (2012). The black box highlights the position in this plane of the globular cluster.

7.3 Looking Ahead

Our GALA model implements a spherical NFW halo and successfully reproduces, to first order at least, the major trends we observe in proper motions and distances. Unlike the earlier claim by Lux et al. (2012) based on much less information, it appears that the NGC 5466 stream cannot yet rule out a spherical halo shape. Indeed, while NGC 5466 is only one stream out of a multitude of such structures, we expect it to be a very useful laboratory for those seeking to better measure the mass and shape of the Milky Way's gravitational potential. Long, thin, and dynamically cold stellar streams such as Pal 5 and NGC 5466 can provide strong constraints on the potential of the Galaxy. The fact that NGC 5466 is so distant, exhibits a strong distance gradient, and is believed to have recently had an interaction with the disk of the Milky Way, makes it a unique test-case for dynamical modelling of the Milky Way.

In the context of observational constraints on NGC 5466, we anticipate that the dynamical properties of the stream quantified in Chapter 5 will help in identifying additional member stars. This is a particular priority for the trailing arm, which could well extend beyond the SDSS and CFIS footprints. This portion of the stream is also much closer ($R_{helio} < 10$ kpc) than the rest, potentially facilitating the search for more members and providing an even more comprehensive mapping of the stream.

The other obvious observational constraint lacking from our analysis are the radial velocities for member stars. In this era of *Gaia*, it is increasingly the case that tangential velocities are more readily available than radial velocities, the exact opposite of what it has been for many decades. However, obtaining the stream's full 6-D kinematics will allow us to explore the phase-space distribution in detail – including deriving energies and angular momenta for our member stars. With spectra of sufficiently high resolution, we can also better explore the chemical abundances of stream stars. Already, this type of analysis on the main body has shown trends in α-elements similarly observed in dwarf galaxies (Lamb et al. 2015; Venn et al. 2004).

The formation of this stream and the cluster's origin provides many insightful questions we hope to answer in the future. But it is also just one cluster. With the all-sky power of *Gaia*, and the wide field u-band perspective of CFIS for 10,000 deg^2 in the north, soon to be followed by the Large Synoptic Survey Telescope (LSST at the Vera C. Rubin Observatory) with more than 20,000 deg^2 in the south, our exploration of the outer Galaxy is only just beginning.

Appendix A

Additional Information

A.1 Observed Parameters of the Gold Sample

The following tables are the observational data for BHBs (Table A.1) and RGBs (Table A.2) of the Gold Sample stream members. Heliocentric distances are photometrically obtained from CFIS, while proper motions are cross-matched from *Gaia* DR2.

We also include positional and proper motion data rotated in the great circle frame (Tables A.3 and A.4; from the translation in Section 5.1). ϕ_1 and ϕ_2 represent the longitude and latitude of this system, respectively. Proper motions in these tables are corrected for Solar reflex motion, then rotated into this frame. Conditional members identified in Section 5.2.3 are appended to the end of Tables A.2 and A.4.

ID	R.A. (°)	Dec (°)	R_{helio} (kpc)	μ_α* (mas yr^{-1})	μ_δ (mas yr^{-1})
1	212.0302	27.5003	17.2967 ± 1.7297	-5.2112 ± 0.1305	-0.6172 ± 0.1437
2	211.1383	28.7820	15.9393 ± 1.5939	-5.2123 ± 0.1166	-0.7325 ± 0.1044
3	212.2727	28.1715	16.2251 ± 1.6225	-5.5180 ± 0.1349	-0.9305 ± 0.1404
4	212.6950	27.1924	15.8071 ± 1.5807	-5.6548 ± 0.1249	-0.9769 ± 0.1363
5	213.7126	28.3461	15.5797 ± 1.5580	-5.8405 ± 0.1152	-0.6391 ± 0.1208
6	211.6359	28.5638	16.0564 ± 1.6056	-5.4169 ± 0.1140	-0.4610 ± 0.1307

Table A.1: List of "Gold Sample" BHBs.

ID	R.A. (°)	Dec (°)	$R_{helio,pred}$ (kpc)	μ_α* (mas yr^{-1})	μ_δ (mas yr^{-1})
7	195.3068	34.2154	21.6520 ± 1.3741	-4.3092 ± 0.3881	-1.9872 ± 0.3450
8	202.6499	33.4567	21.6475 ± 1.8703	-4.6716 ± 0.2569	-0.9615 ± 0.1753
9	204.6825	31.4458	21.3098 ± 1.6581	-4.6976 ± 0.2340	-0.9712 ± 0.2021
10	204.8897	35.1409	18.9778 ± 2.0912	-5.3810 ± 0.1986	-1.3792 ± 0.1389
11	207.7039	30.0776	17.2575 ± 1.2324	-4.6257 ± 0.2220	-1.0034 ± 0.1258
12	208.9051	29.6896	17.2590 ± 1.2863	-5.3480 ± 0.1310	-0.9136 ± 0.0914
13	209.8709	28.8610	16.9963 ± 0.8251	-5.8456 ± 0.2130	-0.8476 ± 0.1748
14	209.7578	29.9678	17.0305 ± 0.8117	-5.2011 ± 0.0765	-0.8851 ± 0.0542
15	211.1529	28.3138	16.4268 ± 0.4823	-5.3972 ± 0.0669	-0.9246 ± 0.0661
16	210.6149	28.7657	18.6889 ± 1.0345	-5.1982 ± 0.2352	-1.2038 ± 0.2508
17	211.6564	28.2156	15.5932 ± 0.7845	-5.4239 ± 0.0779	-0.6604 ± 0.0823
18	213.3529	25.8162	15.6223 ± 0.9959	-5.3910 ± 0.2285	-0.9500 ± 0.2119
19	213.7877	25.1158	15.5186 ± 0.5563	-5.7101 ± 0.1064	-0.7134 ± 0.0967
20	213.7368	27.0737	17.2229 ± 0.8812	-4.9750 ± 0.2347	-0.5004 ± 0.3135
21	213.7444	28.6991	16.8205 ± 1.1477	-5.4889 ± 0.1831	-0.4822 ± 0.1947
22	215.2901	27.0877	12.4913 ± 0.4596	-5.6743 ± 0.0975	-0.8364 ± 0.1119
23	215.4653	27.2993	18.0070 ± 1.0454	-6.1283 ± 0.2307	-0.5721 ± 0.2842
24	215.9519	24.2550	17.7626 ± 1.8410	-5.8570 ± 0.2503	-0.7543 ± 0.2383
25	216.4128	25.8587	16.4943 ± 0.7597	-5.8503 ± 0.0857	-0.8306 ± 0.1060
26*	217.7949	23.6799	10.3904 ± 0.4976	-6.0207 ± 0.0979	-0.3381 ± 0.1120
27	217.8405	24.8631	14.7913 ± 0.9061	-6.0378 ± 0.1080	-0.3962 ± 0.1034
28	219.8409	23.6443	15.5834 ± 0.8387	-6.4060 ± 0.1342	-0.4024 ± 0.1373
29	221.1630	22.9827	17.2438 ± 0.7690	-6.2060 ± 0.1721	-0.3184 ± 0.1686
30	220.6388	23.3639	14.3005 ± 0.6498	-6.2007 ± 0.1058	-0.2952 ± 0.1365
31	222.0228	22.5356	16.9056 ± 1.3742	-5.7303 ± 0.3589	-0.0170 ± 0.3709
32	224.5786	21.8593	16.3049 ± 1.0889	-7.3919 ± 0.3478	-0.3471 ± 0.3517
33*	225.0265	24.9984	11.4767 ± 0.8607	-6.7452 ± 0.1837	-0.2462 ± 0.2571
34*	225.6367	23.1840	11.2105 ± 0.4497	-6.4005 ± 0.1028	-0.3936 ± 0.1299
35**	191.8986	33.1122	29.1899 ± 3.0057	-3.8701 ± 1.3128	-1.1017 ± 0.5421
36**	200.4530	34.5566	23.0920 ± 1.7470	-4.5673 ± 0.3618	-1.4991 ± 0.3415

Table A.2: List of "Gold Sample" RGBs. IDs with an asterisk (*) are the possible contaminates identified in Figure 6.3. The tentative final members added in Section 5.2.3 are marked with double (**).

ID	ϕ_1 (°)	ϕ_2 (°)	μ_{ϕ_1} (mas yr^{-1})	μ_{ϕ_2} (mas yr^{-1})
1	-1.0169	-0.6473	3.5773	-0.2422
2	0.2826	0.1094	3.4694	-0.0848
3	-0.8848	0.0448	3.6424	-0.4972
4	-1.6828	-0.6347	3.7182	-0.5320
5	-1.9106	0.8110	4.0074	-0.3401
6	-0.2053	0.1230	3.7772	0.0175

Table A.3: List of "Gold Sample" BHBs in the rotated great circle frame.

ID	ϕ_1 (°)	ϕ_2 (°)	μ_{ϕ_1} (mas yr^{-1})	μ_{ϕ_2} (mas yr^{-1})
7	14.8034	-0.4181	2.6937	-1.1015
8	8.8576	1.1352	3.2370	-0.5511
9	6.4674	0.0071	3.2133	-0.5985
10	7.8654	3.4324	3.5611	-1.0257
11	3.5350	-0.1058	2.9362	-0.1681
12	2.4302	0.0147	3.6020	-0.4556
13	1.3021	-0.3374	4.0484	-0.6151
14	1.8989	0.5999	3.4566	-0.3642
15	0.0512	-0.2978	3.5681	-0.4263
16	0.6804	-0.1198	3.3623	-0.9172
17	-0.3861	-0.1750	3.6677	-0.0695
18	-2.8641	-1.5543	3.4879	-0.3571
19	-3.5489	-1.9741	3.8738	-0.2963
20	-2.5511	-0.2887	3.4015	-0.0761
21	-1.7624	1.1325	3.8318	-0.2637
22	-3.7466	0.4070	3.5615	0.2789
23	-3.7757	0.6681	4.3691	-0.9047
24	-5.6841	-1.7440	4.0432	-0.8798
25	-5.2335	-0.1493	3.9321	-0.7682
26*	-7.4265	-1.3794	3.9355	1.2545
27	-6.8513	-0.3446	4.2221	-0.2042
28	-9.0432	-0.4306	4.5507	-0.6402
29	-10.4232	-0.3438	4.4759	-0.8088
30	-9.8121	-0.2797	4.3653	-0.1946
31	-11.3320	-0.2929	4.2191	-0.2725
32	-13.6814	0.4400	5.3777	-1.4567
33*	-12.2730	3.2758	4.6083	0.1346
34*	-13.7523	2.0848	4.2402	0.3159
35**	17.1370	-2.3727	2.8652	0.3140
36**	10.9650	1.4306	3.1950	0.1719

Table A.4: List of "Gold Sample" RGBs in the rotated great circle frame. IDs with an asterisk (*) are the possible contaminates identified in Figure 6.3. The tentative final members added in Section 5.2.3 are marked with double (**).

Bibliography

Ankerst M., Breunig M. M., peter Kriegel H., Sander J., 1999. ACM Press, pp 49–60

Antoja T., Ramos P., Mateu C., Helmi A., Anders F., Jordi C., Carballo-Bello J. A., 2020, A&A, 635, L3

Arellano Ferro A., Rojas López V., Giridhar S., Bramich D. M., 2008, MNRAS, 384, 1444

Astropy Collaboration et al., 2013, A&A, 558, A33

Baumgardt H., Hilker M., Sollima A., Bellini A., 2019, MNRAS, 482, 5138

Beccari G., Dalessandro E., Lanzoni B., Ferraro F. R., Bellazzini M., Sollima A., 2015, ApJ, 814, 144

Bell E. F., et al., 2008, ApJ, 680, 295

Bellazzini M., Ibata R., Malhan K., Martin N., Famaey B., Thomas G., 2020, A&A, 636, A107

Belokurov V., 2013, NewAR, 57, 100

Belokurov V., Evans N. W., Irwin M. J., Hewett P. C., Wilkinson M. I., 2006a, ApJL, 637, L29

Belokurov V., et al., 2006b, ApJL, 642, L137

Belokurov V., Erkal D., Evans N. W., Koposov S. E., Deason A. J., 2018, MNRAS, 478, 611

Bianchini P., Ibata R., Famaey B., 2019, ApJL, 887, L12

Bland-Hawthorn J., Gerhard O., 2016, , 54, 529

Bonaca A., Hogg D. W., 2018, ApJ, 867, 101

Bonaca A., et al., 2020, ApJ, 889, 70

Borsato N. W., Martell S. L., Simpson J. D., 2020, MNRAS, 492, 1370

Bovy J., 2015, ApJS, 216, 29

Boylan-Kolchin M., Springel V., White S. D. M., Jenkins A., 2010, MNRAS, 406, 896

Bressan A., Marigo P., Girardi L., Salasnich B., Dal Cero C., Rubele S., Nanni A., 2012, MNRAS, 427, 127

Caldwell N., Bonaca A., Price-Whelan A. M., Sesar B., Walker M. G., 2020, AJ, 159, 287

Carlin J. L., Sand D. J., 2018, ApJ, 865, 7

Carlin J. L., Grillmair C. J., Muñoz R. R., Nidever D. L., Majewski S. R., 2009, ApJL, 702, L9

Castellani V., D'Antona F. A., de Amicis R., Smriglio F., 1973, , 22, 71

Cautun M., et al., 2020, MNRAS, 494, 4291

Chambers K. C., et al., 2016, arXiv e-prints, p. arXiv:1612.05560

Conselice C. J., Wilkinson A., Duncan K., Mortlock A., 2016, ApJ, 830, 83

De Propris R., Harrison C. D., Mares P. J., 2010, ApJ, 719, 1582

Deason A. J., Belokurov V., Evans N. W., 2011, MNRAS, 416, 2903

Deason A. J., Belokurov V., Koposov S. E., Rockosi C. M., 2014, ApJ, 787, 30

Deason A. J., Belokurov V., Sanders J. L., 2019, MNRAS, 490, 3426

Eilers A.-C., Hogg D. W., Rix H.-W., Ness M. K., 2019, ApJ, 871, 120

Ester M., Kriegel H.-P., Sander J., Xu X., 1996. AAAI Press, pp 226–231

Fardal M. A., Huang S., Weinberg M. D., 2015, MNRAS, 452, 301

Farrow D. J., et al., 2014, MNRAS, 437, 748

Fellhauer M., et al., 2006, ApJ, 651, 167

Fellhauer M., Evans N. W., Belokurov V., Wilkinson M. I., Gilmore G., 2007, MNRAS, 380, 749

Gaia Collaboration et al., 2016a, A&A, 595, A1

Gaia Collaboration et al., 2016b, A&A, 595, A2

Gaia Collaboration et al., 2018, A&A, 616, A1

Gallart C., Bernard E. J., Brook C. B., Ruiz-Lara T., Cassisi S., Hill V., Monelli M., 2019, Nature Astronomy, 3, 932

Gravity Collaboration et al., 2019, A&A, 625, L10

Grillmair C. J., 2009, ApJ, 693, 1118

Grillmair C. J., Carlin J. L., 2016, Stellar Streams and Clouds in the Galactic Halo. p. 87, doi:10.1007/978-3-319-19336-6_4

Grillmair C. J., Johnson R., 2006, ApJL, 639, L17

Harris W. E., 1996, AJ, 112, 1487

Helmi A., 2004, ApJL, 610, L97

Helmi A., 2020, arXiv e-prints, p. arXiv:2002.04340

Helmi A., Veljanoski J., Breddels M. A., Tian H., Sales L. V., 2017, A&A, 598, A58

Helmi A., Babusiaux C., Koppelman H. H., Massari D., Veljanoski J., Brown A. G. A., 2018, Nature, 563, 85

Hernitschek N., et al., 2018, ApJ, 859, 31

Hernquist L., 1990, ApJ, 356, 359

Huchra J. P., Geller M. J., 1982, ApJ, 257, 423

Ibata R. A., Gilmore G., Irwin M. J., 1994, Nature, 370, 194

Ibata R. A., Gilmore G., Irwin M. J., 1995, MNRAS, 277, 781

Ibata R., Irwin M., Lewis G. F., Stolte A., 2001a, ApJL, 547, L133

Ibata R., Lewis G. F., Irwin M., Totten E., Quinn T., 2001b, ApJ, 551, 294

Ibata R. A., Lewis G. F., Irwin M. J., Cambrésy L., 2002, MNRAS, 332, 921

Ibata R. A., et al., 2017a, ApJ, 848, 128

Ibata R. A., et al., 2017b, ApJ, 848, 129

Ibata R. A., Malhan K., Martin N. F., 2019, ApJ, 872, 152

Ivezić Ž., et al., 2008, ApJ, 684, 287

Johnston K. V., Law D. R., Majewski S. R., 2005, ApJ, 619, 800

Johnston K. V., Bullock J. S., Sharma S., Font A., Robertson B. E., Leitner S. N., 2008, ApJ, 689, 936

Jurić M., et al., 2008, ApJ, 673, 864

Kilic M., Munn J. A., Harris H. C., von Hippel T., Liebert J. W., Williams K. A., Jeffery E., DeGennaro S., 2017, ApJ, 837, 162

King I., 1962, AJ, 67, 471

Kundu R., Minniti D., Singh H. P., 2019, MNRAS, 483, 1737

Küpper A. H. W., Balbinot E., Bonaca A., Johnston K. V., Hogg D. W., Kroupa P., Santiago B. X., 2015, ApJ, 803, 80

Lamb M. P., Venn K. A., Shetrone M. D., Sakari C. M., Pritzl B. J., 2015, MNRAS, 448, 42

Laporte C. F. P., Johnston K. V., Gómez F. A., Garavito-Camargo N., Besla G., 2018, MNRAS, 481, 286

Law D. R., Majewski S. R., 2010, ApJ, 714, 229

Law D. R., Majewski S. R., 2016, The Sagittarius Dwarf Tidal Stream(s). p. 31, doi:10.1007/978-3-319-19336-6_2

Law D. R., Johnston K. V., Majewski S. R., 2005, ApJ, 619, 807

Lehmann I., Scholz R. D., 1997, A&A, 320, 776

Leon S., Meylan G., Combes F., 2000, A&A, 359, 907

Lindegren L., et al., 2018, A&A, 616, A2

Łokas E. L., Kazantzidis S., Majewski S. R., Law D. R., Mayer L., Frinchaboy P. M., 2010, ApJ, 725, 1516

Lux H., Read J. I., Lake G., Johnston K. V., 2012, MNRAS, 424, L16

Mackereth J. T., et al., 2019, MNRAS, 482, 3426

Majewski S. R., Skrutskie M. F., Weinberg M. D., Ostheimer J. C., 2003, ApJ, 599, 1082

Majewski S. R., et al., 2017, AJ, 154, 94

Malhan K., Ibata R. A., 2018, MNRAS, 477, 4063

Malhan K., Ibata R. A., Martin N. F., 2018, MNRAS, 481, 3442

Malhan K., Ibata R. A., Carlberg R. G., Valluri M., Freese K., 2019, ApJ, 881, 106

Mateu C., Read J. I., Kawata D., 2018, MNRAS, 474, 4112

McConnachie A. W., 2012, AJ, 144, 4

McConnachie A. W., et al., 2018, ApJ, 868, 55

Miyamoto M., Nagai R., 1975, Publications of the Astronomical Society of Japan, 27, 533

Mo H., van den Bosch F. C., White S., 2010, Galaxy Formation and Evolution

Monachesi A., et al., 2019, MNRAS, 485, 2589

Moreno E., Pichardo B., Velázquez H., 2014, ApJ, 793, 110

Mucciarelli A., Bellazzini M., Ibata R., Romano D., Chapman S. C., Monaco L., 2017, A&A, 605, A46

Navarro J. F., Frenk C. S., White S. D. M., 1996, ApJ, 462, 563

Necib L., Ostdiek B., Lisanti M., Cohen T., Freytsis M., Garrison-Kimmel S., 2019, arXiv e-prints, p. arXiv:1907.07681

Necib L., et al., 2020, Nature Astronomy,

Nemec J. M., Harris H. C., 1987, ApJ, 316, 172

Newberg H. J., 2016, Introduction to Tidal Streams. p. 1, doi:10.1007/978-3-319-19336-6_1

Newberg H. J., Carlin J. L., 2016, Tidal Streams in the Local Group and Beyond. Vol. 420, doi:10.1007/978-3-319-19336-6,

Odenkirchen M., Grebel E. K., 2004, in Prada F., Martinez Delgado D., Mahoney T. J., eds, Astronomical Society of the Pacific Conference Series Vol. 327, Satellites and Tidal Streams. p. 284 (arXiv:astro-ph/0307481)

Odenkirchen M., et al., 2001, ApJL, 548, L165

Pearson S., Küpper A. H. W., Johnston K. V., Price-Whelan A. M., 2015, ApJ, 799, 28

Pearson S., Price-Whelan A. M., Johnston K. V., 2017, Nature Astronomy, 1, 633

Planck Collaboration et al., 2016, A&A, 594, A11

Plummer H. C., 1911, MNRAS, 71, 460

Powell D., 2013, Nature, 502, 22

Price-Whelan A. M., 2017, The Journal of Open Source Software, 2, 388

Pryor C., McClure R. D., Fletcher J. M., Hesser J. E., 1991, AJ, 102, 1026

Renaud F., Agertz O., Read J. I., Ryde N., Andersson E. P., Bensby T., Rey M. P., Feuillet D. K., 2020, arXiv e-prints, p. arXiv:2006.06011

Ruhland C., Bell E. F., Rix H.-W., Xue X.-X., 2011, ApJ, 731, 119

Sans Fuentes S. A., De Ridder J., Debosscher J., 2017, A&A, 599, A143

Schönrich R., Binney J., Dehnen W., 2010, MNRAS, 403, 1829

Searle L., Zinn R., 1978, ApJ, 225, 357

Sollima A., 2020, MNRAS, 495, 2222

Somerville R. S., Davé R., 2015, , 53, 51

The Dark Energy Survey Collaboration 2005, arXiv e-prints, pp astro–ph/0510346

Thomas G. F., et al., 2018, MNRAS, 481, 5223

Thomas G. F., et al., 2019, ApJ, 886, 10

Thomas G. F., et al., 2020, arXiv e-prints, p. arXiv:2009.04487

Tononi J., Torres S., García-Berro E., Camisassa M. E., Althaus L. G., Rebassa-Mansergas A., 2019, A&A, 628, A52

Vasiliev E., Belokurov V., 2020, MNRAS, 497, 4162

Venn K. A., Tolstoy E., Kaufer A., Kudritzki R. P., 2004, in McWilliam A., Rauch M., eds, Origin and Evolution of the Elements. p. 58 (arXiv:astro-ph/0305188)

Watkins L. L., et al., 2009, MNRAS, 398, 1757

Xue X.-X., et al., 2011, ApJ, 738, 79

Xue X.-X., Rix H.-W., Ma Z., Morrison H., Bovy J., Sesar B., Janesh W., 2015, ApJ, 809, 144

Yanny B., et al., 2009, AJ, 137, 4377

York D. G., et al., 2000, AJ, 120, 1579